CERN/LHCC/93-50
LHCC/I 6
15 October, 1993

COBEX

Letter of Intent
for a
Collider Beauty Experiment
at the
Large Hadron Collider at CERN

Abstract

The Collider Beauty Experiment [COBEX] Collaboration proposes to build a forward detector dedicated to the study of CP violation and other rare phenomena in the decays of Beauty particles. COBEX would be fully operational at the startup of LHC and, in the course of the first year of operation, should produce precision measurements of CP-violation, B_s mixing over the entire theoretically allowed range of x_s (up to 45 or more), and some FCNC modes.

Members of the COBEX Collaboration

University of California, Los Angeles, U.S.A.
S. Erhan, M. Medinnis, P. Schlein, J.G. Zweizig

Cukurova University, Adana, Turkey
A. Kuzucu, G. Onengut, N. Ozdes

University of Lausanne, Lausanne, Switzerland
C. Joseph, J.P. Perroud, M.T. Tran

University of Liverpool, Liverpool, U.K.
J.R. Fry

University of Massachusetts, Amherst, MA, U.S.A.
E. Hartouni, M. Kreisler

Max Planck Institut für Kernphysik, Heidelberg, Germany
W. Hofmann

Nanjing University, Nanjing, P.R.C.
T.Y. Chen, D. Xi, N.G. Yao

Northwestern University, Evanston, IL, U.S.A.
J. Rosen, K. Seth

Queen Mary & Westfield College, London, U.K.
P.F. Harrison

Rudjer Boskovic Institute, Zagreb, Croatia
P. Bogunovic, G. Paic, D. Rendic, D. Vranic

Centre d'Etudes Nucleaires-Saclay, Gif-sur-Yvette, France
J. Zsembery

Institute for Nuclear Physics, Gatchina, St. Petersburg, Russia
A. Kaschuk, V. Sarantsev, E. Spiridenkov, A. Vorobyov

IHEP-Serpukhov, Protvino, Russia
R. Dzhelyadin, Y. Guz, V. Obraztsov, A. Ostankov, A. Solodkov

Spokesperson:
P. Schlein (SCHLEIN@UCLAHEP)

Contents

1 Introduction & Overview

The COBEX collaboration proposes a dedicated forward Collider Beauty Experiment for the Large Hadron Collider. The design is optimized to achieve unrivaled sensitivity and resolution in the study of CP violation in the decays of Beauty (B) particles. The search for new physics beyond the standard model will also be pursued with sensitive measurements of B_s-$\overline{B_s}$ oscillation and searches for rare decays of B particles. These are goals of the highest order in present day particle physics.

The large $b\bar{b}$ collider cross section expected at the LHC (about 500 μbarn) means that COBEX will be able to carry out a rather precise study of CP violation in B-decay *during the first year of LHC operation*. For example, an average luminosity during the first year as small as $5 \cdot 10^{31}$ cm^{-2}s^{-1} would result in the production of more than $2 \cdot 10^{11}$ B_d and $\overline{B_d}$ mesons and a COBEX statistical measurement uncertainty of 0.027 in the CP violation parameter, $\sin(2\beta)$ for the "gold-plated" final state, $B_d \rightarrow J/\psi K_s^o$. Analogous results would be obtained for other final states as well.

At the end of the same year, there will be more than 10^5 reconstructed and flavor-tagged B_s-mesons. With a measurement resolution in proper time, $\sigma(\tau)$ = 3%, $x_s = \Delta M/\Gamma$ can be well determined over the entire theoretically allowed range (as large as 45 or more). Moreover, the determination of the angle γ in CP violating B_s decays will be highly constrained.

It will also be possible to make stringent tests of the loop-induced standard model predictions for several flavor-changing-neutral-current processes. For example, using the calculations of Ali et al.[1], COBEX expects that a sample of about 5000 events of $B_d^o \rightarrow \mu^+\mu^- K^{*o}$ should be available at the end of the first year. This would allow the study of shapes of the B decay distributions, in addition to its rate, and could lead to evidence for new physics beyond the standard model at an early stage in the life of the LHC.

1.1 Overview of a Collider B Experiment

Fig. 1.1 shows the laboratory angular distribution of the B-meson momentum vector expected at the LHC, calculated using the PYTHIA 5.6 Monte Carlo event generator[2]. A fundamental production asymmetry is seen.

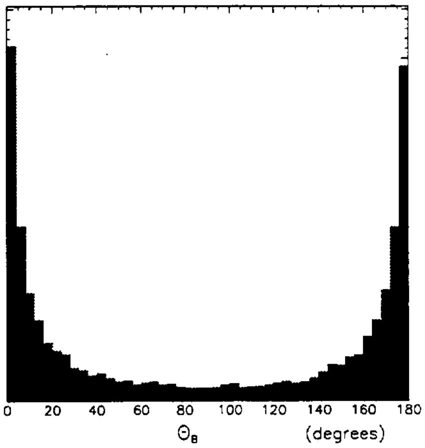

Figure 1.1: Angular distribution of B-meson momentum vector in the laboratory, calculated using PYTHIA.

The inherently asymmetric parton-parton interactions for production of $b\bar{b}$-quarks at collider energies lead to the rather sharp forward and backward peaking in the angular distribution of B-mesons in the laboratory. Thus, there is no fundamental reason to introduce an additional asymmetry by decreasing one of the beam momenta and, in the limit, running in a fixed target mode.

The following are the underlying features of the Collider Beauty Experiment, COBEX:

- **Large $b\bar{b}$ cross section (500 μbarn):** Very significant results can be obtained during the first year of LHC operation when beam currents are planned to be about 10% of final values. Considerable flexibility is allowed in selecting events.
- **Large ratio of $b\bar{b}$ to inelastic cross section (1/150):** This value at LHC collider energy means that the requirements on the Level-1 trigger are modest and non-critical
- **Relatively small average B-meson momentum (80 GeV):** Allows for a short, inexpensive and precise detector, for which it is easier to provide particle identification. There is excellent measurement resolution in B-meson proper time (3%) and in invariant mass (σ_M = 8 MeV for the $B_d \rightarrow J/\psi K_s^o$ channel).

The detector layout is shown in Fig. 1.2 and a typical event in Fig. 1.3.

The COBEX design has evolved from first and second generation forward experiments at the ISR by members of our collaboration and from extensive detector R&D work on a new detector element in the experiment, planar silicon detectors inside the vacuum pipe perpendicular and close to the circulating

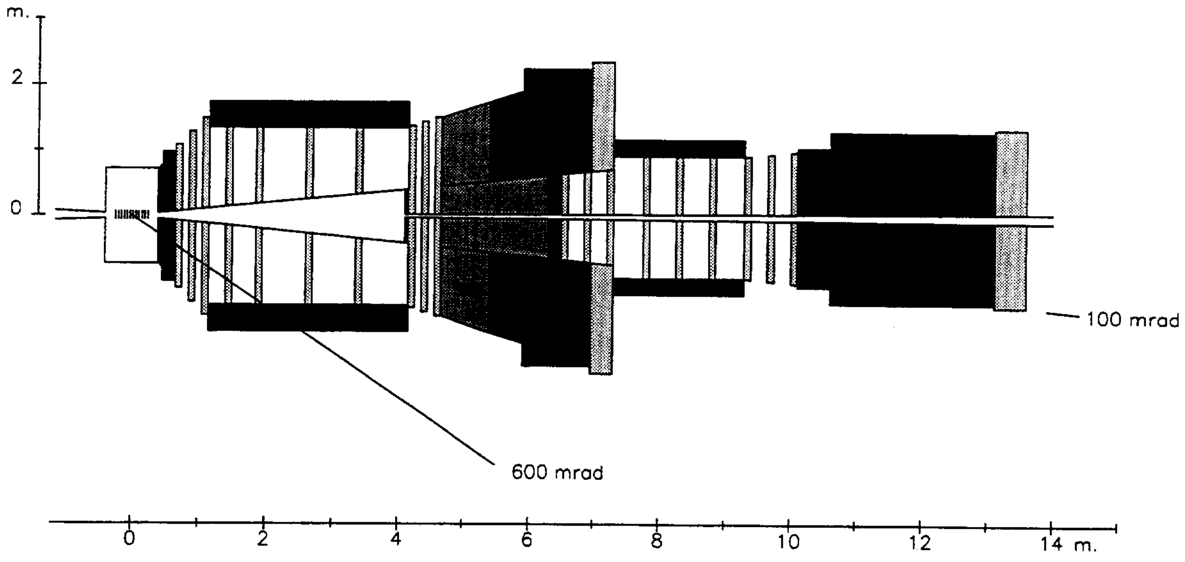

Figure 1.2: COBEX layout: The silicon microvertex detector is installed inside the collider vacuum pipe at the center of the interaction region. The large quadrupole magnet has pole tip field 1.5 T; the dipole field is 2.5T. Two vacuum windows, at 40 cm and 410 cm, respectively, are connected by a thin conical vacuum pipe section. Tracking chambers are light grey, gas RICH counters are medium grey and electromagnetic calorimeters are dark grey. Iron is black. The electromagnetic calorimeter and muon filter sections after Spectrometer I are retractable, if necessary to reduce "spray".

beams (P238), used with data-driven processors as the Level-1 trigger (RD21).

The forward collider detector with 600 mrad aperture shown in Fig. 1.2 takes optimal advantage of the forward peaking seen in Fig. 1.1. Fig. 1.4 shows the expected distribution of all B-momenta at LHC; the shaded events are those which have all decay products contained in a 600 mrad aperture. The momentum distributions of reconstructed event samples (see Chapt. 9) are very close to the shaded distribution in Fig. 1.4.

Most of the reconstructed events have momenta between 30 and 200 GeV, which results in the mean value of 80 GeV and a corresponding mean flight path of 5 mm. As shown in Chapter 9, the measurement uncertainty in this distance using the COBEX silicon microvertex detector (see Chapt. 4) is about 108 μm. This leads to the measurement uncertainty in B-meson proper time of 3%, which will make it possible to measure rather precisely the decay time oscillations of B_s-mesons with x_s over the entire theoretically allowed range, (as large as 45 or more). This capability will be an important component in the CP violation analysis discussed in Chapt. 10.

The large aperture (10 to 600 mrad) spectrometer system comprises a quadrupole magnet spectrometer relatively close to the interaction point (for tracking the slower, wide-angle tracks), and a dipole magnet spectrometer further from the interaction point (for tracking the faster, low angle tracks). The smaller field near the axis of the quadrupole allows small angle tracks to emerge without major deflection, from a window at the end of a conical vacuum pipe, and pass into the downstream dipole spectrometer. The layout allows for efficient reconstruction of slow or fast K^0's and Λ^0's.

The spectrometers (see Chapt. 3) will be instrumented by wire chambers which yield a spatial resolution of the order of 30 μm per projected coordinate. Gas and liquid Ring-Imaging Cherenkov counters (see Chapt. 5) provide particle identification over the complete momentum range of interest. Electromagnetic calorimeters (see Chapt. 6) follow each spectrometer and are used for reconstruction of final states with a single gamma or π^0 (possible when the constraints from sub-mass cuts exist) and for electron identification. Finally, there are muon filters (see Chapt. 7) following the spectrometers, which are used for triggering and for offline identification of muons.

Much of the COBEX experiment has now been

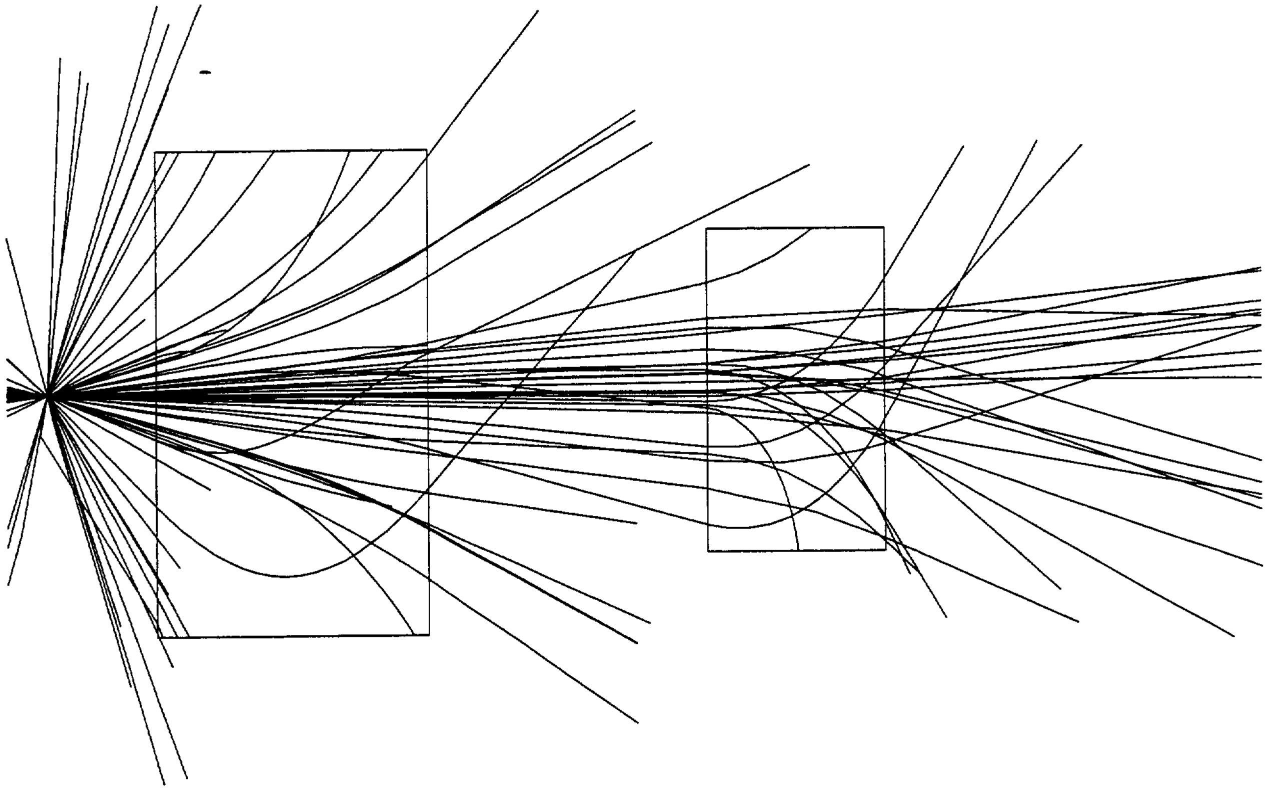

Figure 1.3: A typical COBEX B event showing the trajectories of charged tracks in the magnetic spectrometers. Particles with angles less than 100 mrad do not emerge from the vacuum pipe until the end of the quadrupole magnet.

simulated, including track reconstruction in the quadrupole spectrometer. Quadrupole track-finding efficiencies are more than 99% (starting from 3-dimensional points), with a ghost contamination of about 1%.

The COBEX detector can be installed in an existing even LEP area, on one side of an interaction region (see Chapt. 11), with minimal modification and negligible cost, and can use an existing LEP counting room. Our cost estimate for the entire detector including magnets is about 47 MSF.

1.2 Performance Parameters

COBEX will have three different modes of operation, the first two of which are summarized in Table 1.1:

- **"Low" Luminosity = $5 \cdot 10^{31}$ cm^{-2}s^{-1} :** Up to this luminosity, an impact parameter trigger algorithm, based on silicon microvertex data, suppresses events which are consistent with a single vertex. This Level-1 trigger has been shown[3, 4] to be capable of reducing the minimum bias rate by more than a factor of 1/100,

	COBEX	
$\mathcal{L}_{COBEX}$ (cm^{-2}s^{-1}) $\mathcal{L}_{LHC}^{max}$	$5 \cdot 10^{31}$ $1.5 \cdot 10^{33}$	$5 \cdot 10^{32}$ $1.5 \cdot 10^{34}$
Interaction Rate	3.5 MHz	35 MHz
Interactions per bunch crossing	0.09	0.9
min. bias suppression in Level-1	10^{-2}	10^{-3}
Output Rate Level-1	35 KHz	35 KHz
Required Suppression	1/350	1/350
$\sigma(b\bar{b})$	500 μb	
N($b\bar{b}$) in 1 year	$2.5 \cdot 10^{11}$	$2.5 \cdot 10^{12}$
$B_d \rightarrow J/\psi K_s^o$ $\rightarrow \ell^+ \ell^- \pi^+ \pi^-$	$4.6 \cdot 10^{6}$	$4.6 \cdot 10^{7}$
ϵ_{total}	$2.9 \cdot 10^{-3}$	$2.7 \cdot 10^{-3}$
Tagged Event Sample	$1.3 \cdot 10^{4}$	$1.2 \cdot 10^{5}$
$\sigma[\sin(2\beta)]$	0.027	0.009

Table 1.1: Top: COBEX minimum bias rate parameters assuming 25 nsec bunch spacing and 70 mbarn inelastic cross section. Bottom: $b\bar{b}$ rates and "CP-Reach" for $B_d \rightarrow J/\psi K_s^o$.

while retaining good efficiency (20-50%) for B-mesons (this increases the $b\bar{b}$/inelastic ratio to about 1/5). Table 1.1 summarizes the overall data-flow situation for the minimum bias component. The Level-1 event output rate is 35 KHz. In 10^7 seconds, $3.5 \cdot 10^{11}$ events are produced. As discussed in Chapt. 8, reducing this rate to such a level that not more than 10^9 interesting events are written to tape during a year will require a suppression of at least 1/350 in a "farm" of hundreds of high-performance RISC processors or in a powerful data-driven-processor system, as is being studied in RD21.

- **"Medium" Luminosity = $5 \cdot 10^{32}$ cm^{-2}s^{-1}:** At higher luminosities, up to about $5 \cdot 10^{32}$ cm^{-2}s^{-1}, the topology trigger is replaced by a single muon trigger (see Chapters 7 and 8). This trigger is based on the signals from a muon filter consisting of iron walls interspersed with muon chambers. The muon tracks are reconstructed online. Triggering on a single muon with transverse momentum at least 1.5 GeV yields more than 10^{-3} minimum bias suppression. As seen in the table, the same Level-1 output rate of 35 KHz results and the overall data flow situation is approximately the same as at the lower luminosity.

  For both the low and medium luminosity situations, Table 1.1 also shows the "bottom line" event yield for the CP violation analysis of the "gold plated" channel $B_d \rightarrow J/\psi K_s^o$ Chapters 9 and 10 discuss the source of these numbers in more detail.

- **"High" Luminosity = $5 \cdot 10^{33}$ cm^{-2}s^{-1}:** This operating mode would be intended specifically for the rare decay mode: $B_s \rightarrow \mu^+\mu^-$, which is expected[1] to have a branching ratio of $1.8 \cdot 10^{-9}$ in the absence of new physics (see Chapt. 2 for a discussion of the physics importance of this channel). With this luminosity, about 36K such events are produced in a year's run, of which about 9K events will decay into our apparatus. Several hundred events should survive the most severe cuts which are necessary to suppress the background (consisting mainly of uncorrelated muon pairs from semileptonic decays of B and $\bar{B}$). The apparatus would run with the silicon detectors retracted to 1 cm from the beams, at which point the radiation damage would be the same as it is running at 1/10 the luminosity with the silicon 3 mm from the beams. Such running should be possible. More detailed calculations are in progress and will be reported to the LHCC.

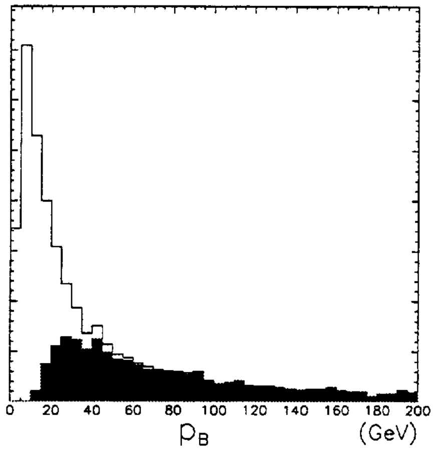

Figure 1.4: Total momentum of B-mesons produced at the LHC, calculated using PYTHIA. The shaded events are those $B_d \rightarrow J/\psi K_s^o$, whose decay products are all contained within a 600 mrad aperture. 29% of the shaded event sample have momenta larger than 200 GeV and are off-scale at the right hand side of the plot.

References

[1] A. Ali et al., DESY 93-016

[2] H.U. Bengtsson and T. Sjöstrand, Computer Physics Comm., **46** (1986) 43.

[3] J. Ellett et al. [P238 Collaboration], Nucl. Instrum. & Methods **A317** (1992) 28

[4] S. Erhan et al. [COBEX Collaboration], Nucl. Instrum. & Methods **A333** (1993) 101.

2 Physics Objectives

Within the Standard Model, quark mixing is parameterized by the Cabibbo-Kobayashi-Maskawa (CKM) matrix. This matrix has 9 complex elements, but because of the constraints of unitarity, and the freedom to redefine the phases of quark fields, it may be parameterized in terms of only 4 independent variables. In the parameterization of Wolfenstein[1], it is written:

$$V = \begin{pmatrix} V_{ud} & V_{us} & V_{ub} \\ V_{cd} & V_{cs} & V_{cb} \\ V_{td} & V_{ts} & V_{tb} \end{pmatrix} \tag{1}$$
$$= \begin{pmatrix} 1-\lambda^2/2 & \lambda & A\lambda^3(\rho - i\eta) \\ -\lambda & 1-\lambda^2/2 & A\lambda^2 \\ A\lambda^3(1-\rho-i\eta) & -A\lambda^2 & 1 \end{pmatrix}$$

It is important to note that the CKM matrix is not simply an arbitrary parameterisation of physical observables, but appears in the Standard Model Lagrangian. *Hence its parameters are of equal importance in the theory as, say, G_F or the masses of the Z^0 and the top quark.* There has been much experimental effort expended recently [2] on measuring the latter two quantities, the first of which is now known with startling precision.

In contrast however, the two CKM parameters ρ and η are very poorly determined. A major goal of this experiment is a precise determination, and in fact an over-determination of these two quantities as a sensitive test of the Standard Model description of quark mixing. In conjunction with measurements already made, this can be accomplished by the measurement of $B_s^0 - \overline{B_s^0}$ mixing, CP violation in various decays of B-mesons, and rare decays of B-mesons.

In order to appreciate the full significance of these measurements, it is necessary to consider the information currently available on the elements of the CKM matrix, and its limitations.

So far, $|V_{ud}|$ has been determined precisely in nuclear beta decay and $|V_{us}|$ from $K \to \pi \ell \nu$ decays. These give a precise measurement of λ ($\simeq 0.22$) to about 1 %. $|V_{cb}|$, and thus A, is determined from semileptonic B decays, A being found to be 0.8 ± 0.1. With the increased statistics which will become available at CLEO II over the next few years, and using a recently suggested technique [3] for the extraction of $|V_{cb}|$, it is probable that this quantity will eventually be determined with a precision of around 1 % also.

Three present measurements provide limited information on the remaining two variables, ρ and η. One is the determination of $|V_{ub}/V_{cb}|$ from the measurement of the ratio of charmless to charmed semileptonic B-decays at CLEO. From Eq. 1 it can be seen that this combination fixes the value of $\sqrt{\rho^2+\eta^2}$ (as λ is known). This results in an annulus in the $\rho - \eta$ plane, centered on the origin (Fig. 2.1). It is again likely that this measurement will improve over the next few years, as statistics increase. At present however, the errors which determine the width of the annulus are dominated by model dependence. A program is underway [4] to try to gather enough data to distinguish between the models. It is expected that the width of the annulus will eventually be reduced by a factor of 2 which will help considerably to constrain the allowed region of the $\rho - \eta$ plane.

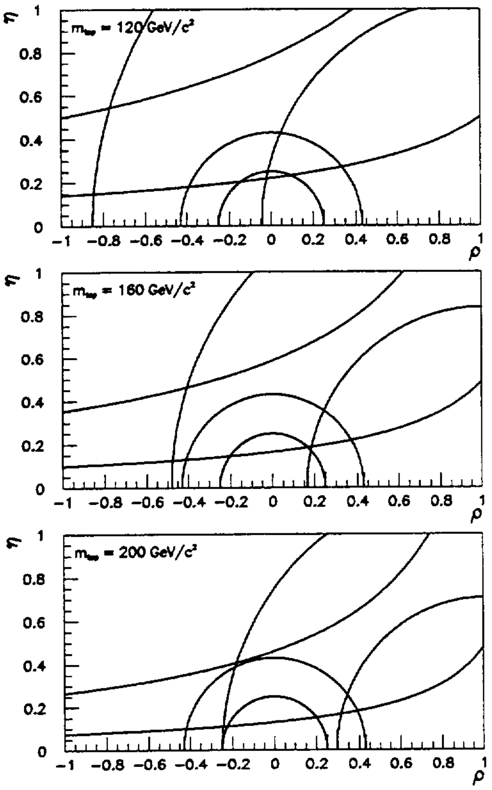

Figure 2.1: Limits on the CKM parameters ρ and η for three values of the top-quark mass. The annular region centered at the origin is the region allowed by the measurements of $|V_{ub}/V_{cb}|$. The annular region centered on the point (1,0) is that allowed by measurements of $B_d^0 - \overline{B}_d^0$ mixing. The approximately hyperbolic band is the region allowed by the measurements of the CP-violation parameter ϵ in kaon decays.

The other two relevant measurements are those of $B_d^0 - \overline{B_d^0}$ mixing and the CP-violation parameter, ϵ, in K decays. Although both are well-measured, their interpretations in terms of CKM parameters are dogged by theoretical uncertainties and a dependence on the unknown top-quark mass. $B_d^0 - \overline{B_d^0}$ mixing depends on the combination $|V_{td}V_{tb}^*|^2$ which can be seen to fix the quantity $(1-\rho)^2 + \eta^2$ (A and λ being known) thereby defining an annulus in the $\rho - \eta$ plane centered on the point (1,0). ϵ depends approximately on the quantity $(1-\rho)\eta$, measurements thereby providing constraints which form hyperbolae in the $\rho - \eta$ plane.

The constraints provided by all the above measurements are shown in Fig. 2.1 for three possible values of the top-quark mass. In each case the theoretical errors dominate the width of the constraint-bands shown. There is little chance of a significant reduction in most of these uncertainties, unless Lattice QCD may shed light on some of them [5].

The above measurements are often discussed with reference to the so-called "Unitarity Triangle", (Fig. 2.2) whose vertices are formed by the origin, the point (1,0) and the point (ρ,η). The inside angles of the triangle can be determined rather well by measurements of CP-violation in B-decays. The following notation will be used for them:

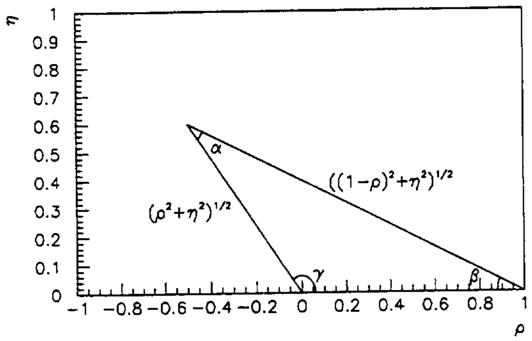

Figure 2.2: The Unitarity Triangle

- α is the inside angle at the point (ρ,η),
- β is the inside angle at the point (1,0),
- γ is the inside angle at the origin.

In this experiment, we hope to measure all three angles precisely, as a thorough test of the internal consistency of the Standard Model.

2.1 $B_s^0 - \overline{B_s^0}$ Mixing.

The general formalism of $B^0 - \overline{B}^0$-mixing has been described many times and is reviewed in ref. [6]. Allowing for $B^0 \leftrightarrow \bar{B}^0$ transitions, the time-evolved state for an initial $B^0(\overline{B}^0)$ may be written:

$$\overset{(-)}{\psi}(t) \propto e^{-\imath m_1 t - \Gamma_1 t/2}.|B_1> +(-)\, e^{-\imath m_2 t - \Gamma_2 t/2}|B_2> \qquad (2)$$

where $|B_1>$ and $|B_2>$ are the two eigenstates of the B-meson mass matrix. Then the probability of the state to decay as a $B^0(\overline{B}^0)$ meson is given by

$$|<B^0|\overset{(-)}{\psi}(t)>|^2 \propto e^{-\Gamma t}[1 \pm \cos(\Delta m t)] \qquad (3)$$

$$|<\overline{B}^0|\overset{(-)}{\psi}(t)>|^2 \propto e^{-\Gamma t}[1 \mp \cos(\Delta m t)] \qquad (4)$$

where $\Delta m = m_1 - m_2$ and $\Gamma \equiv \Gamma_1 \approx \Gamma_2$. Dilution effects, discussed in Chapter 10, mean that what are actually observed in the four data samples are linear combinations of the two functions in Eqs. 3 and 4. Observation of the time dependences in any of the four samples enables the mixing parameter x_α, and a "dilution factor" to be determined.

Let us see how a measurement of $B_s^0 - \overline{B_s^0}$ mixing can improve the determination of the quantity $(1-\rho)^2 + \eta^2$ (ie. the distance from the apex to the point (1,0)). We define the mixing parameter $x_\alpha = \Delta m_\alpha / \Gamma_\alpha$, where α stands for the flavour of the light quark in the B-meson. In the Standard Model, this is given by [6]:

$$x_\alpha = \tau_{B_\alpha} \frac{G_F^2}{6\pi^2} m_{B_\alpha} \eta_{QCD} (B_{B_\alpha} f_{B_\alpha}^2) F m_t^2 |V_{t\alpha}V_{tb}^*|^2. \qquad (5)$$

τ_{B_α} and m_{B_α} are measured, while η_{QCD}, B_{B_α} and f_{B_α} are all calculated, their uncertainties accounting for the widths of the relevant annular bands in the figures. $F(m_t^2/M_W^2)$ is an analytic and slowly varying function of m_t, the unknown top-quark mass. If we now consider the ratio x_d/x_s, we see that the troublesome top-quark mass dependence is canceled completely while all the calculated quantities appear as ratios which are expected to be close to unity and to have small uncertainties. In fact we get

$$(\rho-1)^2+\eta^2 = \left(\frac{x_d}{x_s}\right)\left(\frac{1}{\lambda^2}\right)\left(\frac{B_{B_s}}{B_{B_d}}\right)\left(\frac{\tau_{B_s}}{\tau_{B_d}}\right)\left(\frac{f_{B_s}}{f_{B_d}}\right)^2 \qquad (6)$$

where the last four factors are all known with small uncertainties, giving a much improved constraint for $(\rho-1)^2+\eta^2$.

It should be noted that, as the parameter $|V_{ts}V_{tb}^*|^2$ which governs $B_s^0 - \overline{B_s^0}$ mixing depends only on A and λ, the measurement of this quantity provides no direct information on ρ and η. Rather it provides the combination $\eta_{QCD}(B_{B_s} f_{B_s}^2) F(m_t^2/M_W^2) m_t^2$ in Eq. 5. Assuming this to be similar to the equivalent combination for the B_d^0, as expected, one is then able to extract the combination $(\rho-1)^2+\eta^2$ from $B_d^0-\overline{B_d^0}$ mixing.

It is of interest to know what the current experimental and theoretical limits are on the parameter x_s. There is rather little direct experimental evidence for $B_s^0-\overline{B_s^0}$ mixing. The time-integrated B^0 mixing observed at the $\Upsilon(4S)$ machines [7] is pure $B_d^0-\overline{B_d^0}$ mixing, while that observed at UA1, CDF and LEP is due to a mixture of B_d^0 and B_s^0 mesons. These allow one to derive a lower limit for the amount of $B_s^0-\overline{B_s^0}$ mixing at $x_s > 1.6$. Time-integrated measurements will be of little use in improving this bound in the future. Exclusive time-dependent mixing measurements are needed in order to proceed further in the study of B_s^0 mixing.

Theoretical predictions of the rate of B_s^0 mixing may be obtained from the Standard Model, Eq. 5 above. Allowing the ranges 120 GeV $< m_t <$ 200 GeV and 0.15 GeV $< \sqrt{B_{B_s}}f_{B_s} <$ 0.25 GeV, this predicts $6 < x_s < 44$. In principle, another constraint is available for x_s: the determination of $|V_{ub}/V_{cb}|$ by CLEO may be combined with the measured value of ϵ to constrain the position of the point (ρ,η). The argument may then be reversed to determine x_s from Eq. 6 using the measured value of x_d. We find $0.5 < (\rho-1)^2+\eta^2 < 2.0$, giving $6 < x_s < 40$, where we have used $x_d = 0.69 \pm 0.1$ [10] and $f_{B_s}/f_{B_d} = 1.08 \pm 0.06$ [8]. It is coincidental that this method gives similar information to the previous direct method of calculation.

As shown in Chapter 10, the above range of x_s is well within the reach of COBEX. It is quite possible that, in the meantime, improved measurements of the ratio $|V_{ub}/V_{cb}|$ will become available, and/or the discovery of the top-quark. Any such developments will serve to constrain further the theoretically allowed range of values of x_s. Failure to find $B_s^0-\overline{B_s^0}$ mixing in the allowed range will immediately signal a failure of the Standard Model description of quark mixing in weak interactions.

With the ratio x_d/x_s measured as discussed above, and with the anticipated improved bounds on the ratio $|V_{ub}/V_{cb}|$, the intersection of the two resulting (relatively narrow) bands defining the sides of the unitarity triangle should be quite well determined. The constraint from ϵ will provide a non-trivial cross-check which will be made much tighter if the top-quark mass is measured by then. Then the latter, in conjunction with the x_s measurement, will provide a "measurement" of the quantity $\sqrt{B_{B_s}}f_{B_s}$ for comparison with lattice QCD calculations [5].

2.2 CP Violation in B-decays

CP violation is an interesting topic in its own right. It is not yet fully understood in the Standard Model, and is put-in for empirical reasons, by allowing the Yukawa couplings of the Higgs to the quarks to be complex. In the case of 3-or-more generations, this results in a complex component in the CKM matrix which, in turn, gives rise to CP violating observables in weak interactions. This origin of CP violation is intimately related to both the mass problem (the quark masses also arise from the Higgs-quark Yukawa couplings) and the generation problem (as the effect would be absent with less than three generations). On a larger scale, CP violation is thought to be a necessary precondition for the origin of the baryon asymmery of the universe. All these facts make the study of CP violation a compelling one.

As we have argued in the above sections, despite the fact that CP violation is well-measured in the neutral Kaon system, this has only a limited impact on our knowledge of the fundamental complex quantity ($|\eta|$) in the CKM matrix, both because of the unknown top-quark mass, and because of incalculable (to date) hadronic factors. On the other hand, many CP-violating observables in the decays of B-mesons are expected to provide highly constraining information, owing to a complete absence of hadronic uncertainties. Hence, having fixed the unitarity triangle as described in the above sections, we would like to perform very precise tests on its internal consistency using measurements of such observables, as a test of the Standard Model description of quark mixing in weak interactions. There are three types of such measurements:

- Decays of neutral B-mesons to final states which are CP-eigenstates.
- Decays of neutral B-mesons to final states which are not CP-eigenstates.
- Decays of charged B-mesons.

The general features of the above types of measurements are discussed below in turn:

Decays of Neutral B-mesons to CP-eigenstates.

In the case of neutral B-mesons, CP-violation is entwined with the phenomenon of $B^0-\overline{B^0}$ mixing. The general formalism has been described many times and may be found for example in the review of Ref. [9]. In this formalism, the two eigenstates of the neutral B-meson mass matrix, $|B_1>$ and $|B_2>$, may be written in terms of the beauty eigenstates:

$$|B_{1(2)}> = p|B^0> +(-)q|\overline{B^0}> \qquad (7)$$

where, within the Standard Model, the ratio q/p is given by the CKM phases

$$(q/p)_{B_d} \simeq 2\arg(V_{td}V_{tb}^*), (q/p)_{B_s} \simeq 2\arg(V_{ts}V_{tb}^*) \quad (8)$$

for the two types of neutral B-meson respectively. Considering a final state f, which is a CP eigenstate, we can define the decay amplitudes for pure beauty eigenstates:

$$M = |<f|B^0>| \ and \ \overline{M} = |<f|\overline{B^0}>| \qquad (9)$$

and the quantity:

$$\lambda = \frac{q}{p}\frac{<f|\overline{B^0}>}{<f|B^0>}. \qquad (10)$$

(This should not be confused with the CKM parameter of the same name). Then the time-dependent rates for the decays of states which are initially in a pure B^0 or $\overline{B^0}$ state (they may oscillate into the charge-conjugate state before decaying) into the final state f are given by

$$\begin{aligned}\Gamma(t)(\overset{(-)}{B}{}^0 \to f) &= Ae^{-\Gamma t}[1 \pm B\cos\Delta mt \\ &\mp C\sin\theta\sin\Delta mt] \qquad (11)\end{aligned}$$

where $A = (M^2+\overline{M}^2)/2$, $B = (M^2-\overline{M}^2)/(M^2+\overline{M}^2)$, and $C = (2M\overline{M})/(M^2+\overline{M}^2)$. Note that $C^2 = 1-B^2$. θ is the phase of λ. If the two decays each involve a unique CKM phase, $M = \overline{M}$, and the equations simplify considerably. Then, the time-dependent asymmetry

$$\begin{aligned}A_f(t) &= \frac{\Gamma(t)(B^0\to f)-\Gamma(t)(\bar{B}^0\to f)}{\Gamma(t)(B^0\to f)+\Gamma(t)(\bar{B}^0\to f)} \\ &= \sin 2\phi_f\sin(\Delta mt), \qquad (12)\end{aligned}$$

where ϕ_f is one of the angles of the unitarity triangle. Clearly the amplitude of the asymmetry has no hadronic uncertainties and is a direct measure of a CKM quantity. A channel for which this is the case is $B_d^0 \to J/\psi K_S^0$, which is governed by the angle β. This is also very attractive experimentally, because of its dilepton decay signature.

When more than one CKM phase is involved, the asymmetry has a more complicated form, and depends on the magnitudes of the amplitudes. Then, isospin analysis is needed to extract the CKM information, requiring several channels to be observed. An example of this case is $B_d^0 \to \pi^+\pi^-$ whose asymmetry is governed by the angles α. Penguin diagrams may contribute to the amplitudes however, necessitating reconstruction of the experimentally daunting $\pi^0\pi^0$ final state.

Another channel suffering from additional hadronic contributions is that of $B_s^0 \to \rho K_S^0$ whose aysmmetry is governed by γ. It is also thought to have a very low branching ratio, making measurements difficult. However there are alternative channels and methods for all these angles.

COBEX will be sensitive to $\sin 2\beta$ in several decay channels, including $B_d^0 \to J/\psi K_S^0$, $B_d^0 \to \psi(2S)K_S^0$ and $B_d^0 \to J/\psi K^{0*}$. The CP-reach in these channels will be summarised in Chapter 10.

Decays of Neutral B-mesons to non-CP-eigenstates.

The analysis of this type of decay is analogous to that described above to CP-eigenstates, except for the added complication of unknown hadronic final state phases. Considering a final state f, with CP conjugate denoted $\overline{f}$, it can be shown (Ref. [11]) that if the amplitudes $<f|B^0>$ and $<f|\overline{B^0}>$ each involve a unique weak phase, then

$$|<f|B^0>| = |<\overline{f}|\overline{B^0}>| = M \qquad (13)$$

and

$$|<\overline{f}|B^0>| = |<f|\overline{B^0}>| = \overline{M}. \qquad (14)$$

Then the time dependent rates for the decays of states which are initially in a pure B^0 or $\overline{B^0}$ state are given by

$$\begin{aligned}\Gamma(t)(\overset{(-)}{B}{}^0 \to f) &= Ae^{-\Gamma t}[1 \pm B\cos\Delta mt \\ &\mp C\sin(\phi_f+\delta_s)\sin\Delta mt] \, (15)\end{aligned}$$

$$\begin{aligned}\Gamma(t)(\overset{(-)}{B}{}^0 \to \overline{f}) &= Ae^{-\Gamma t}[1 \mp B\cos\Delta mt \\ &\mp C\sin(\phi_f-\delta_s)\sin\Delta mt] \, (16)\end{aligned}$$

where A, B and C have the same definitions as in Eq. 11. δ_s is the strong interaction final state phase difference between $<f|B^0>$ and $<f|\overline{B^0}>$. An illustration of the forms of the above functions for typical values of the parameters is shown in Fig. 2.3. Fitting Eqs. 15 and 16 to the observed time-dependences yields the quantities $\overline{M}/M$, $\sin(\gamma+\delta)$ and $\sin(\gamma-\delta)$, from which $\sin(\gamma)$ may be obtained.

This method can be applied to measure γ at COBEX, by using the following B_s decays to non-CP-eigenstates:

- $B_s^0 \to D_s^{\pm}K^{\mp}$,
- $B_s^0 \to D_s^{*\pm}K^{\mp}$
- $B_s^0 \to D_s^{\pm}K^{*\mp}$

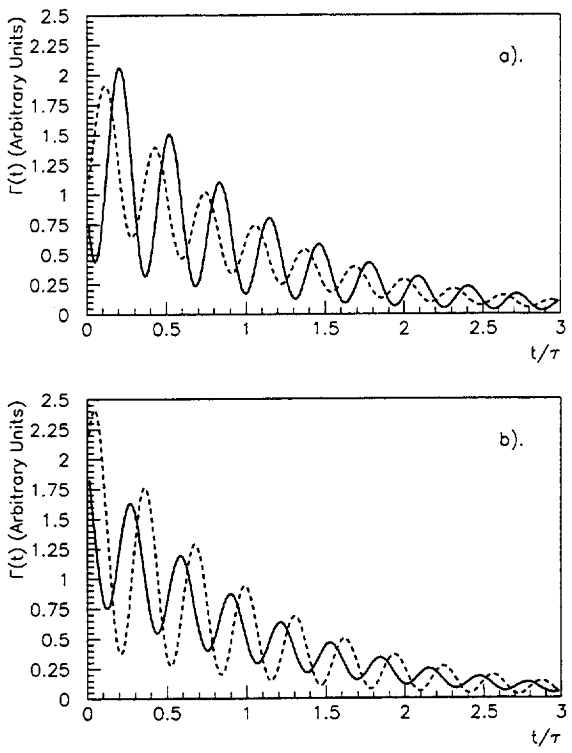

Figure 2.3: Examples of proper time distributions for decays of neutral B-mesons to final non-CP-eigenstates. The examples shown are for B_s-mesons with $x_s = 20$, $\phi_f = 0.5$, $\delta_s = 0.2$ and $\overline{M}/M = 1/\sqrt{2}$. The solid and dashed curves are for B_s-mesons and $\overline{B_s}$-mesons respectively for Eq. 15 in a). and Eq. 16 in b).

which are expected to have the time dependences given in equations 15 and 16.

Decays of Charged B-mesons.

A second method of measuring γ consists of measuring the exclusive decay rates in the following 3 channels:

- $B^+ \to D_1^0 K^+$
- $B^+ \to \overline{D}^0 K^+$
- $B^+ \to D^0 K^+$

and their CP-conjugates. As $D_1^0 = (D^0 + \overline{D}^0)/\sqrt{2}$,

$$A(B^+ \to D_1^0 K^+) = [A(B^+ \to D^0 K^+) + A(B^+ \to \overline{D}^0 K^+]/\sqrt{2} \quad (17)$$

and

$$A(B^- \to D_1^0 K^-) = [A(B^- \to D^0 \overline{D}^0 K^-) + A(B^- \to \overline{D}^0 K^-]/\sqrt{2} \quad (18)$$

It has been pointed out (Ref. [12]) that the amplitudes are related by

$$A(B^+ \to \overline{D}^0 K^+) = A(B^- \to D^0 K^-) \quad (19)$$

$$A(B^+ \to D^0 K^+) = \exp(2i\gamma) A(B^- \to \overline{D}^0 K^-) \quad (20)$$

where γ is the CKM phase to be measured. Then, Eqs. 17 and 18 may be described by two triangles in the complex plane, as shown in Fig. 2.4.

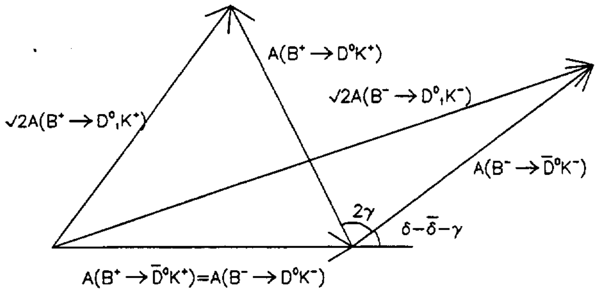

Figure 2.4: Complex triangles of Eqs. Eqs. 17 and 18

In these channels, the charged B-meson is self-tagging (by the charge of the kaon in the final state). Measurement of the amplitudes of all six amplitudes (in fact, only four are independent) enables the angle γ to be extracted up to a two-fold ambiguity. As described in Ref. [12], the ambiguity may be removed by comparison of several different channels, eg. the ones above with D_1^0 replaced by D_2^0, and both of these channels with the $K^\pm$ replaced by other states with similar quantum numbers, eg. $K^0\pi^\pm$, $K^\pm\pi^0$, $K^0\pi^\pm\pi^\mp$, etc. These have the same CKM dependence, but different final state phases in each case, allowing the common CKM phase to be extracted from the analyses. In fact, this procedure alone provides a test of the Standard Model, namely the requirement of a common CKM solution between all channels.

Analogous channels exist for $B^0 \to D^0(\overline{D}^0, D_1^0, D_2^0)X_s$ but these have a smaller branching ratio for the B and are not self-tagging.

This method has the advantage of simplicity, in the sense that only the rates are required to be measured. On the other hand, not observing a time dependence, it may be difficult to prove that what one sees is really

CP violation. The many channels approach should however increase confidence in the results.

COBEX will be able to reconstruct all the above channels, and in view of its large cross-section×Luminosity×acceptance, will have unrivalled statistical precision.

2.3 Rare B-decays

(The text in this section is a shortened version of a memo by Ahmad Ali[13]. We are very grateful to him for his help.)

Theoretical interest in rare (Flavor Changing Neutral Current) B-decays lies, in the first place, in their potential role as precision tests of the Standard Model in the flavour sector. Within the Standard Model, their eventual measurements will provide quantitative information about the top quark mass and more importantly about the CKM matrix-elements, V_{td}, V_{ts} and V_{tb}. In particular, the CKM-suppressed rare B-decays directly measure V_{td}. Together with improved measurements of the CKM matrix elements $|V_{cb}|$ and $|V_{ub}|$, the measurements of $|V_{td}|$ will determine the CKM unitarity triangle, pinning down the CP violating phases in the Standard Model.

At the same time, rare B-decays have the potential to provide early evidence for non-SM physics. It is therefore imperative to get as reliable estimates of these decays in the SM as possible, and to carry out an experimental physics programme sensitive to FCNC decays.

The experimental search for the FCNC B-decays has already provided first dividends. The recent CLEO observation [14] of the rare decay mode $B \to K^* + \gamma$, having a combined branching ratio $BR(B \to K^* + \gamma) = (4.5 \pm 1.5 \pm 0.9) \cdot 10^{-5}$, and an improved upper limit on the inclusive branching ratio $BR(B \to X_s + \gamma) < 5.4 \cdot 10^{-4}$ (95% $C.L.$) [15] have been analyzed in the SM-context, as well as in several SM-extensions. Within the SM, the resulting experimental measurements have been interpreted as a corresponding limit on the CKM-matrix element ratio $|V_{ts}|/|V_{cb}|$. Combining the exclusive and inclusive decay rates, the CLEO measurements yield: $0.50 \leq |V_{ts}|/|V_{cb}| \leq 1.67$ (at 95% $C.L.$) [16].

While the radiative rare B-decays were expected to have larger SM-branching ratios, and hence to be measured first, the FCNC B-decays involving dileptons are very promising, as they involve different effective interactions than the ones involving photons. In particular, the radiative B-decays are neither sensitive to effective operators involving the non-diagonal bsV or bdV couplings, where V represents a virtual Z boson or a virtual photon, nor to the effective four fermi operators such as $(\bar{s}\Gamma_i b)(\ell^+ \Gamma_i \ell^-)$, where Γ_i is some linear combination of the Dirac γ-matrices. Since these couplings are the ones which determine the SM-rates and distributions and they are also present in a number of SM-extensions, *there exists a strong case for dedicated experimental studies involving semileptonic and leptonic FCNC B-decays.*

In the semileptonic FCNC decays, the complete Dalitz distributions involving the dilepton pair and the recoiling hadron(s) are measurable, and hence both the shapes and rates can be used to search for non-SM effects. Since normalized distributions in SM depend essentially on the top quark mass, but are otherwise reliably calculable with the help of QCD, effects of non-SM physics are easy to search for and interpret.

FCNC semileptonic and purely leptonic B decays can be classified as the CKM- allowed and CKM-suppressed transitions involving the matrix element V_{ts} and V_{td}, respectively. COBEX has a built-in sensitivity for measuring FCNC semileptonic and leptonic decays, such as $B \to X_s \ell^+ \ell^-$ and $B \to X_d \ell^+ \ell^-$, with the dilepton mass being different from the J/ψ and ψ' resonance regions to reduce the CC component. The exclusive decays $B \to (K, K^*) + \ell^+ \ell^-$ and $B \to (\pi, \rho, \omega) + \ell^+ \ell^-$ are of particular interest. Also for them, the short distance pieces are measurable only away from the J/ψ and ψ' resonant regions.

Theoretical predictions of exclusive rare B-decays are less sharp at present, than are those for their corresponding inclusive decays. This is so, since rare B-decays involve the so-called heavy to light hadron transitions, as opposed to the heavy to heavy CC decays $B \to (D, D^*)\ell\nu_\ell$, which have been quantitatively studied in the HQET framework and are under theoretical control. Significantly firm statements on the exclusive rare B-decays can be made if the CKM-suppressed CC exclusive decays such as $B \to (\pi, \rho, \omega)\ell\nu_\ell$ become available experimentally. Their measurements will reduce the extrapolation over a large kinematic region, reducing the parametrization dependence of the relevant form factors. Since the present experimental sensitivity involving the CC decays $b \to u$ is on the threshold of these measurements, it should be possible to make firm predictions for the corresponding FCNC processes in future.

Inclusive Semileptonic FCNC B-Decays: $B \to (X_s, X_d)\ell^+\ell^-$

The details for the calculation of both the long and short-distance contributions to inclusive FCNC $B \to (X_s, X_d) + \ell^+ \ell^-$ decays can be seen in Ref. [17], where the theoretical Dalitz distribution and a number of decay distributions are calculated. The short distance contributions to the branching ratios are estimated as:

$$\begin{aligned} BR(B \to X_s + e^+e^-) &= (0.6 - 2.5) \cdot 10^{-5} \\ BR(B \to X_s + \mu^+\mu^-) &= (3.5 - 14.0) \cdot 10^{-6} \end{aligned}$$

for the top quark mass range 100 GeV $< m_t <$ 200 GeV, whereas for $m_t = 150$ GeV, one obtains $BR(B \to X_s + e^+e^-) = 1.5 \cdot 10^{-5}$ and $BR(B \to X_s + \mu^+\mu^-) = 8.5 \cdot 10^{-6}$. Thus, FCNC semileptonic decay rates are much more sensitive to m_t than the corresponding FCNC radiative B decays. These estimates are to be contrasted with the present upper limit for the (averaged) B-meson branching ratio from the UA1 collaboration: $BR(B \to X + \mu^+\mu^-) = 5 \cdot 10^{-5}$ [18], indicating an experimental sensitivity only an order of magnitude away in this channel.

The Dalitz distributions in the FCNC semileptonic decays can be used to project out definite pieces of the effective Hamiltonian, which provide increased sensitivity to non-SM physics. For example, one can define a forward-backward asymmetry for the dileptons in their center of mass system with respect to the X_s-momentum (or the K^*-momentum for the exclusive decay $B \to K^*\ell^+\ell^-$) in the B rest-frame. It has been shown that for the presently allowed top quark mass, this asymmetry in the Standard Model is proportional only to the Z and W^+W^- exchange diagrams, with the virtual Z contribution numerically dominating. Thus, the forward- backward asymmetry in FCNC semileptonic decays is sensitive to any enhancement in the effective bsZ and bdZ couplings. Likewise, all non-SM scenarios, which inherently have a chiral structure different from that of the Standard Model, will yield unmistakable distortion effects on the B decay distributions.

Exclusive Semileptonic FCNC B-Decays: $B \to (K, K^*)\ell^+\ell^-$

We now discuss the exclusive semileptonic rare decays $B \to (K, K^*)\ell^+\ell^-$. The corresponding CKM-suppressed exclusive decays $B \to (\pi, \rho, \omega)\ell^+\ell^-$ can be obtained by the appropriate CKM-matrix element ratio. One may exploit heavy quark symmetries of heavy to light transitions to obtain relations between the CC semileptonic heavy to light decays and the FCNC rare B decays. Estimates based on the assumed parametrizations of the Isgur-Wise function, fitted to the semileptonic D-decays, are given in [19, 20].

Heavy quark symmetries work best in the region close to the maximal momentum transfer to the leptons and we restrict ourselves to the comparison of the lepton spectra of the processes mentioned above close to the point of maximal momentum transfer. The estimated branching ratios of the exclusive semileptonic rare decays $B \to (K, K^*)\ell^+\ell^-$ are given in Table 2.1.

Parameterization	A	B
$BR(B \to K\ell^+\ell^-)$	$6.0 \cdot 10^{-7}$	$2.7 \cdot 10^{-7}$
$R(B \to Ke^+e^-)$	4%	2%
$R(B \to K\mu^+\mu^-)$	7%	3%
$BR(B \to K^*e^+e^-)$	$5.6 \cdot 10^{-6}$	$4.1 \cdot 10^{-6}$
$R(B \to K^*e^+e^-)$	37%	28%
$BR(B \to K^*\mu^+\mu^-)$	$2.9 \cdot 10^{-6}$	$2.5 \cdot 10^{-6}$
$R(B \to K^*\mu^+\mu^-)$	34%	29%

Table 2.1: Rates and branching fractions for the decays $B \to K\ell^+\ell^-$, $B \to K^*e^+e^-$ and $B \to K^*\mu^+\mu^-$ with $\ell = e, \mu$, and $m_t = 150$ *GeV*. A and B are two different parameterizations of the Isgur-Wise function used in the calculation. The quantity R is the ratio of the rate of each channel to that of its corresponding inclusive strangeness channel.

The numbers in Table 2.1 are in agreement with other estimates in the literature within a factor 2, which is the theoretical accuracy one should expect.

Leptonic FCNC B-Decays: $(B_s^0, B_d^0) \to \ell^+\ell^-$.

The decay rates for $(B_s^0, B_d^0) \to \ell^+\ell^-$were discussed some time ago in Ref. [21] to lowest (1 loop) order. With the help of the effective Hamiltonian formalism one can incorporate the QCD effects, and we refer to a recent calculation of this decay mode in Ref. [22].

The rates for the decays $B_s^0 \to \mu^+\mu^-$ and $B_s^0 \to e^+e^-$ are suppressed, compared to the corresponding rate for $\tau^+\tau^-$ by $(m_\mu/m_\tau)^2$ and $(m_e/m_\tau)^2$, respectively. For the dilepton modes, they are estimated as:

$$\begin{aligned} BR(B_s \to \mu^+\mu^-) &= 2.0 \cdot 10^{-9} \qquad (21) \\ BR(B_d \to \mu^+\mu^-) &= 8.0 \cdot 10^{-11} \end{aligned}$$

Again, one can express the decay rates $\Gamma(B_d^0 \to \ell^+\ell^-)$ in terms of the rates for $\Gamma(B_s^0 \to \ell^+\ell^-)$ using the relation in the CKM model:

$$\frac{\Gamma(B_d^0 \to \ell^+\ell^-)}{\Gamma(B_s^0 \to \ell^+\ell^-)} = \frac{|V_{td}|^2}{|V_{ts}|^2}(1 + \delta_\ell), \qquad (22)$$

where δ_ℓ is an $SU(3)$-breaking parameter. Again, for the default value $|V_{td}/V_{cb}|^2 = 0.05$, one expects the branching ratios for $B_d^0 \to \ell^+\ell^-$ to be suppressed by ~ 20, as compared to the corresponding decays $B_s^0 \to \ell^+\ell^-$.

The purely leptonic decays of B_d^0 and B_s^0 mesons are of considerable interest in theories with leptoquarks [23]. In the leptoquark scenario, the effective four-fermi operators involving the $(\bar{s}\Gamma_i b)(\ell^+\Gamma_i\ell^-)$ couplings can be enormously enhanced. This allows for searches for induced effects of leptoquarks which would go much beyond their direct searches.

2.4 Other Physics

COBEX at the LHC will accumulate vast numbers of B-mesons and baryons. Besides the two main goals, of determining parameters of the standard model and testing the model itself, there will be significant opportunities to study many other areas of B-physics, such as:

- b-quark production dynamics,
- spectroscopy of mesons and baryons with b-quarks,

Below we present brief descriptions of the potential of COBEX in some of these areas.

2.4.1 Production dynamics

b-quark production in hadronic reactions is fundamental to the study of perturbative QCD[24]. Complete next-to-leading-order calculations are available for the total, one particle inclusive cross-sections and correlations. Inclusive cross-sections measured by CDF[25] at $p_t > 10$ GeV are a factor three above these predictions. The reason for this discrepancy is unknown. Perhaps the discrepancy between theory and experiment should not be taken too seriously at present, because the experimental data are not very precise and the theoretical calculations suffer from poor knowledge of the structure functions at small x. Better information on these should soon be available from HERA. Precise measurements of the total cross-sections and the p_t and x distributions in the broad region $0.05 < x < 0.5$, $p_t < 5$ GeV can lead to very unambiguous confrontation of theory with experiment.

Another interesting topic is the investigation of rather specific b-quark fragmentation dynamics[26], which exhibits itself in production of $b - \bar{s}$ and $\bar{b} - s$. The standard event generator PYTHIA gives for p-p collisions $\sigma(\bar{B}_s) > \sigma(B_s)$ as a consequence of a difference in the masses of strings generating these mesons. A B_s-meson is produced as a result of $\bar{b} - u$ $(\bar{b} - d)$ string breaking, while a $\bar{B}_s$-meson is produced after $b - ud$ $(b - uu)$ string breaking. These strings have different masses because of a big difference between quark (u,d) and diquark (uu,ud) momenta and the probability of their breaking into strange quarks increases with string mass. Therefore in p-p collisions this model as well as other models with white strings or clusters yields $\sigma(\bar{B}_s) > \sigma(B_s)$. Observation of this effect would be very valuable.

2.4.2 Heavy flavor spectroscopy

As a useful by-product of the search for CP-violation in the beauty sector, the very large samples of data containing heavy flavour particles which will be accrued may be used for the study of heavy flavor spectroscopy [27].

There are two interesting areas of heavy flavour spectroscopy:

- Open flavor states, i.e. B_d, B_s, B_c, D_s and D-meson systems and Charm- and Beauty-flavored baryons.
- Hidden flavor states, i.e. cc- and bb- onium states.

There are many missing (undiscovered) states in both categories — states which are not readily produced exclusively due to quantum number preferences or states which are not readily observed inclusively due to experimentally difficult decay channels. With COBEX, it may be possible to fill in some of the holes in the present listings of heavy flavor states. Of particular interest would be the identification of heavy flavor mesons which are not easily explained in terms of a $q\bar{q}$ paradigm but rather may be evidence for hadro-molecular states.

There is some interest in whether useful self-tagging schemes might be possible, using the hadronic or electromagnetic cascade decays of excited B-mesons. Whether or not such B-meson flavor-tagging will prove to be competitive with traditional methods based on the partner $\bar{B}$ decay remains to be seen. The initial study of such states and their decays is however a necessary pre-requisite of any such tagging schemes and could be performed at COBEX.

B_c Physics

Bound states of a b and $\bar{c}$ quark pair (the B_c mesons) have never been observed. The study of bound states of heavy quarks with different flavours, such as $B_c(\bar{b}c)$ and $\bar{B}_c(b\bar{c})$, is of great interest for several reasons. Firstly, this interest is related to heavy meson spectroscopy and its description in the framework of potential models. Secondly, the study of weak decays of such mesons implies the possibility of determining some parameters of the Standard Model.

The current theoretical status of B_c physics, both production and decay, is summarized by Likhoded et al.[28] (see also Refs. [29, 30, 31]). One can expect B_c production rates at LHC which are nearly 1% of those for B_d mesons. Because of the existence of one c quark already in the meson, branching ratios to final states which contain J/ψ are expected to be very large.

Excited Heavy Flavor States

Within the quark model the ground state neutral B mesons consist of a $\bar{b}d$ (B^0) or a $\bar{b}s$ (B_s^0). To date only one excited state, the B^*, has been observed. The mass of this 1^- (quark model assignment) state is 5324.6±2.1 MeV. As this state is relatively narrow and much less than a pion mass above the B meson ground states, decays to the ground state take place radiatively. Unfortunately the signature photon energy is too low for presently configured collider spectrometers.

At the 1993 Snowmass conference the results[32] of detailed calculations for masses of the 1^3P_1 and 1^3P_2 excited D_s, B, and B_s mesons were presented. Whether or not there is a significant cross section for any of these excited states, relative to the ground states, is an open question. Results from e^+e^- machines and photoproduction experiments may not necessarily be indicative of hadro-production trends. It is expected that COBEX will be able to shed considerable light on this field.

Excited beauty mesons will tumble down to the lowest lying ground states (either B or B_s) through a combination of radiative transitions and strong decays. As such, their secondaries will come from the primary interaction vertex. Due to parity conservation the 1^3P_1 state cannot decay directly by pion emission to the B ground state but can go through the B^*. Single pion emission of the 1^3P_1 (and presumably broader 1^3P_0) is allowed. One variant of self-tagging would involve identifying a charged pion whose direction vector is close to the neutral B vector and whose $\pi^\pm B^0$ invariant mass is close to the 1^3P_2. We note however a couple reasons why this type of resonance self-tagging may be difficult:

- Although the production of P-wave states may be large, only a restricted number of decays - those with a charged pion and neutral B meson in the final state - are relevant. For example, given equal initial populations of the 1^3P_2 (B^{**+}, B^{**0}, $\overline{B}^{**0}$, B^{**-}), only one-third of the strong decays will lead to the desired final state.

- Contributions from dipion decays such as $B^{**0} \rightarrow \pi^+\pi^-B^0$ where one of the pions is soft and missed and the other appears to resonate with the B^0 with consequent flavor dilution. A hadro-molecular state (BV, V=ρ,ω) would fall in this category.

It would appear that flavor self-tagging will not work for B_s^0 since the $\bar{b}-s$ system has zero isospin and consequently no transitions involving single charged pions. If any or all of the P-wave states lie below the $m_B + m_K$ threshold, those states will decay by E1 γ emission. Above this threshold B_s^0 excited states will fall apart into $B + K$ (or $B + K\pi$) and consequently short circuit the B_s^0. This is directly analogous to the more familiar situation in charmonium where transitions to low lying states are effectively quenched above the open charm thresholds, $2m_D$ and $m_D + m_{D^*}$.

There is a rich field of spectroscopy to be mined. Not only is it interesting in its own right, but it can clarify outstanding issues in light quark spectroscopy as well as serve as a technical basis for symmetry studies such as CP violation.

Heavy Flavor Onium States

The observed $b\bar{b}$ onium states, consist of six $^3S_1$ and six $^3P_{J=0,1,2}$ states. Conspicuous in their absence are D-wave states, singlet P-wave states, and the $^1S_0's$. Potential model predictions for some of these states exist. The reasons for this pattern are well known: much of the world's sample of beauty particles (hidden and open) comes from e^+e^- machines where the $b\bar{b}$ pair has the quantum numbers of the virtual annihilation photon, 1^{--}. Triplet P-wave states are subsequently populated through radiative decays of higher- lying $^3S_1$ states. By contrast however, inclusive production at hadron colliders might lead to a more democratic population of quantum levels. The excited states produced will decay radiatively to the ground state which will, at least in some cases, decay to dimuon pairs which will satisfy the COBEX muon trigger. The problem of identifying the excited states then becomes one of identifying the transitions to the ground state through small and experimentally difficult decay modes. But, this might well be possible in some cases at COBEX.

Generally the spacings between bottomonium states are reasonably well described by potential models. Thus on the whole potential model predictions should serve as useful guides to undiscovered states.

References

[1] L. Wolfenstein, Phys. Rev. **D31** (1985) 2381.

[2] J. Lefrancois, Talk presented at International Europhysics Conference on High Energy Physics, Marseille, 1993.

[3] M. Neubert, Phys. Lett. **B264** (1991) 455.

[4] S. Stone, private communication.

[5] C.T.Sachrajda in "B Decays", edited by S. Stone, World Scientific, 1992.

[6] H. Schroder, in "B Decays", edited by S. Stone, World Scientific, 1992.

[7] For an extensive review, see eg. A. Ali and D. London, J. Phys G.: Nucl. Part. Phys. **19** (1993).

[8] C.T.Sachrajda, Talk presented at conference QCD - 20 years later, Aachen, 1992.

[9] Y. Nir and H.R. Quinn, in "B Decays", edited by S. Stone, World Scientific, 1992.

[10] M.V. Danilov, Talk presented at International Europhysics Conference on High Energy Physics, Marseille, 1993.

[11] R. Aleksan, I. Dunietz & B. Kayser, Zeit. Fur Phys. **C54**, 653 (1992).

[12] M. Gronau, & D. Wyler, Phys. Lett. **B265** (1991) 172.

[13] A. Ali, private communication (1993).

[14] Evidence for Penguins: First observation of $B \to K^*(892)\gamma$, R. Ammar et al. (CLEO), CLNS-93-1212; see also, S. Stone, Nucl. Instrum. & Methods **A333** (1993) 15.

[15] E. Thorndike (CLEO), Talk at the American Physical Society Meeting, Washington (D.C.), April 12 (1993) and private communication.

[16] A. Ali and C. Greub , DESY Report 93-065 (1993).

[17] A. Ali, T. Mannel and T. Morozumi, Phys. Lett. **B273** (1991) 505.

[18] C. Albajar et al. (UA1), Phys. Lett. **B262** (1991) 163.

[19] A. Ali, C. Greub and T. Mannel, DESY Report 93-016(1993).

[20] A. Ali and T. Mannel, Phys. Lett. **B264** (1991) 447. Erratum: *ibid* **B274** (1992) 526.

[21] B.A. Campbell and P.J.O'Donnell, Phys. Rev. **D25** (1982) 1989.

[22] A.J. Buras and G. Buchalla, Max-Planck Institute Report MPI-PTh-2-93 (1993).

[23] W. Buchmüller and D. Wyler, Phys. Lett. **B 177** (1986) 377;
B.A. Campbell et al., Int. J. Mod. Phys. **A2** (1987) 831.

[24] P. Nason, to appear in "Heavy flavors", Advanced Series on Directions in High Energy Physics (eds. M. Lindner & A.J. Buras - World Scientific, Singapore).

[25] M.L. Mangano, Nucl. Instrum. & Methods **A333** (1993) 57.

[26] A.M. Zaitsev & A.A. Solodkov, Nucl. Instrum. & Methods **A333** (1993) 169.

[27] J. Rosen, J. Marques and L. Spiegel "Heavy Flavor Spectroscopy" contribution to 1993 Snowmass Workshop on B physics.

[28] A.K. Likhoded, S.R. Slabospitsky, M. Mangano and G. Nardulli, Nucl. Instrum. & Methods **A333** (1993) 209.

[29] V.V.Kiselev et al., Yad. Fiz. **49** (1988) 1100 (in Russian).

[30] S.S. Gershtein, A.K. Likhoded and S.R. Slabospitsky, Int. Jour. of Mod. Phys. **6A** (1991) 2309.

[31] L. Claveli, Phys. Rev. D26 (1982) 1610; C.R. Ji and F. Ahiri, Phys.Rev. **D35** (1987) 3318.

[32] E. Eichten, C. Hill, and C. Quigg, "Properties of Excited B Mesons", FERMILAB-Pub-93/255-T, Submitted for Proceedings of Snowmass 1993 B-Physics Workshop.

3 Magnetic Spectrometers

The proposed COBEX apparatus is illustrated in Fig. 1.2. The upper acceptance limit is set to approximately 600 mrad. This is the largest practical aperture for a planar geometry detector. The exact value for this upper limit is not critical since the acceptance for B states increases only slowly above this limit: significant gains in acceptance would require large increases in aperture.

The full aperture is covered by two coaxial spectrometers, with acceptances from 100 mrad to 600 mrad (Spectrometer I) and from 10 mrad to 100 mrad (Spectrometer II). The principle advantage of this two-spectrometer design is that it results in large savings in channel count and detector volume.

The two spectrometers are similar in design. The first element of each spectrometer is a silicon pixel detector, followed by a system of drift chambers before, inside and after their respective analyzing magnets. Both also contain liquid and gas RICH counters, electromagnetic calorimeters and muon identifiers. Each of these ancillary systems is described in separate sections, below.

The most notable difference between the two spectrometers is that Spectrometer I uses a quadrupole for momentum analysis while Spectrometer II uses a dipole. The use of a quadrupole magnet in Spectrometer I has two distinct advantages: (a) particles with angles $\theta < 100$ mrad receive minimal bending inside the beam pipe before emerging from the vacuum window and entering Spectrometer II; (b) the stray field at the positions of the silicon detectors and the RICH detectors is minimized.

The use of a quadrupole for momentum analysis is unconventional, so it is important to understand whether its relatively complex field shape could lead to problems in pattern recognition or areas of poor momentum measurement. A Monte Carlo study (see Sect. 3.7.1) of Spectrometer I convinced us that unambiguous track recognition with high efficiency can be achieved and that the momentum resolution is adequate (see Sect. 3.7.2).

Fig. 1.3 illustrates the tracking properties of the magnetic system for a typical event, which contains B-mesons. Note that the tracks which pass inside the conical vacuum pipe in the quadrupole magnet are scarcely deflected.

3.1 Performance Requirements

The magnetic spectrometer, when coupled with the electromagnetic calorimeters, muon detector and RICH counters must be capable of unambiguous and clean reconstruction and tagging of a wide variety of B, B_s and B-baryon decays.

The spectrometer design is being driven by the following goals:

- efficient track finding in the angular range from 10 mrad to 600 mrad for all charged particles with momenta larger than ≈ 300 MeV,
- efficient matching between silicon tracks and spectrometer tracks,
- B-mass resolution of 15 MeV or better for decay modes containing only charged particles,
- isolation or near isolation of events occurring in adjacent bunches,
- simplicity and cost effectiveness.

The most critical design consideration depends on perpendicular distance ($r_\perp$) from the beam: particle density (charged and neutral) and average momentum are both strong functions of $r_\perp$. At low values of $r_\perp$, ensuring low cell occupancy, obtaining sufficient integrated field and limiting gamma conversions in spectrometer materials are the most vexing problems, while at high $r_\perp$, limitation of multiple scattering becomes the most critical consideration.

3.2 Operating Environment: Particle Density, Flux and Cell Occupancy

Fig. 3.1 shows the (Pythia-generated) charged particle density as a function of perpendicular distance from the beam ($r_\perp$), for three different values of longitudinal distance (z) from the interaction region. In the region of interest, the density is roughly approximated by the z-independent function: $dN/dr_\perp = 0.95/{r_\perp}^2$ particles per cm^2, with $r_\perp$ in cm.

Integrating this over an infinitely long stripe which is tangent to a circle of radius $r_\perp$, results in a prediction for drift-cell occupancy of $\approx \pi/r_\perp$, with $r_\perp$ in cm, for a 1 cm wide drift cell. The density and occupancy distributions will be flattened by the magnetic field, but still give reasonably accurate worst-case occupancy predictions for detectors in front of the Spectrometer I quadrupole and near the beam pipe, in front of the Spectrometer II dipole.

At an LHC luminosity of $5 \cdot 10^{32}$ cm^{-2}s^{-1} the inelastic interaction rate will be 35 MHz, or nearly one interaction per bunch crossing and the resulting charged particle flux will be $\approx 35/{r_\perp}^2 \cdot 10^6$ cm^{-2}s^{-1} at $r_\perp$ cm from the beam.

The dose rate due to charged particles from interactions for thin, low atomic number materials such

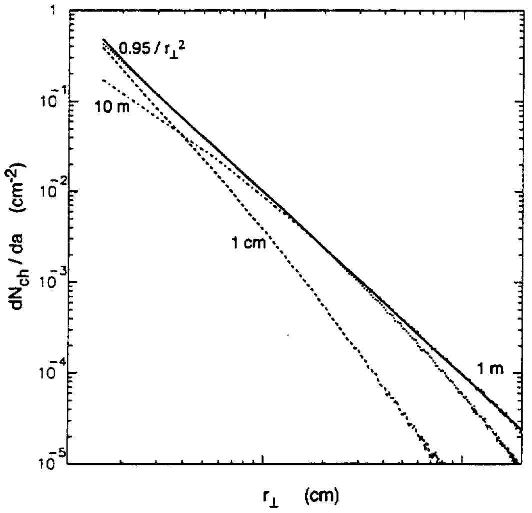

Figure 3.1: The charged particle density as a function of perpendicular distance from the beam line. The solid line is the function 0.95 / $r_\perp{}^2$. The other three curves are from a Pythia simulation at three different distances from the interaction region center (1 cm, 1 m, 10 m).

as carbon, silicon or aluminum is readily calculated from the above flux to be about 100 / $r_\perp{}^2$ kGy/year. This will be the dominant dose to the tracking elements. Since COBEX does not have large solid-angle hadron calorimeter coverage, neutron irradiation will not contribute substantially.

3.3 Analyzing Magnets

3.3.1 Spectrometer I: Quadrupole

Spectrometer I uses a quadrupole magnet with 1.5 m radius and a length of 3 m. The pole tip field is 1.5 Tesla. The average field integral seen by an infinite momentum particle produced at the origin and at polar angle θ is $\int Bdl = B' \cdot L_1 \cdot z_1 \cdot \tan\theta / \cos\theta$, where B' is the field gradient (1 Tesla/m), z_1 is the center of the quadrupole (2.65 m)and L_1 is its length. Thus, a 100 mrad track will see an integrated field of 0.8 Tesla-m and a track at 360 mrad (the largest angle which traverses the length of the magnet) will see an integrated field of 3.0 Tesla-m. The implications for momentum and mass resolution are discussed in Sect 3.7.

The physical implementation of this quadrupole is under study [1]. Various alternative designs are being considered. The most promising is a superferric skew quadrupole with two coils and 4 pole-tips. The return yoke has an 8 m × 8 m cross-section and is 3 m long.

3.3.2 Spectrometer II: Dipole

Spectrometer II contains a superconducting dipole with a uniform magnetic field of 2.5 Tesla, a radius of 1 m and a length of 2 m.

3.4 Vacuum Chamber

The vacuum pipe seen in Fig. 1.2 runs the entire length of the spectrometer. The second window at 4.1 m follows the conical section with half-angle of 100 mrad. The minimum angle acceptance Spectrometer II is determined by the pipe radius at the position of the second window. A pipe radius of 4 cm implies a minimum angle of θ_{min} of 10 mrad.

It appears feasible to have have a pipe radius as small as 2 cm, nonetheless, we assume a radius of 4 cm since this already gives adequate acceptance, approximately matching the acceptance of the microvertex detector, and eases the problems of vacuum pumping. Also, below 6 cm, the high particle density complicates the design of the tracking chambers and other elements.

Construction of the vacuum chamber from aluminum or carbon fibre (or both) will limit multiple scattering of the particles and reduce interactions of particles in material near the beam. Both of these materials have been used successfully at CERN for construction of beam pipes. Recent improvements in aluminum welding used at CERN make aluminum an attractive, cost effective material. Although carbon fibre is more expensive, it could provide additional immunity to secondary interactions in critical areas such as near the window of Spectrometer II, where the beam pipe reaches its minimum diameter (8 cm).

3.5 Silicon Pixel Detectors

A silicon pixel detector is placed at the entrance to both spectrometers. The primary purpose is to aid in matching tracks found in the microvertex detector to those in the spectrometer. Above 150 mrad, tracks emerging from the silicon detector will typically traverse a few of the hybrids associated with each silicon detector, the vacuum chamber window and the RICH counter before emerging into the magnetic spectrometer. Similarly tracks emerging into Spectrometer II traverse 4 m of vacuum, a window and a RICH counter before entering the first momentum-measuring drift chambers. The detailed simulation of microvertex detector/spectrometer matching has not yet been done, however, we believe that the added redundancy of a trajectory measurement after the vacuum window and before the liquid RICH counter will prove useful, though perhaps not indispensable.

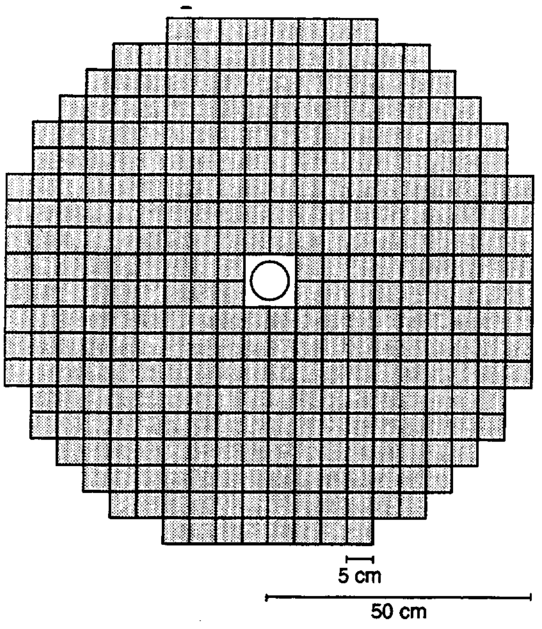

Figure 3.2: Front view of the Spectrometer I silicon pixel detector.

The Spectrometer I pixel detector is composed of 328 5 × 5 cm^2 silicon wafers, each with 100 5 × 5 mm^2 pixels. A front view of the Spectrometer I pixel detector is shown in Fig. 3.2. The total channel count is 32,800. The Spectrometer II pixel detector will contain 218 such tiles and a channel count of 21,800. The total number of tiles in the system is 546, the total channel count is 54,600.

The inner edge of the pixel detectors are 5 cm from the beam, and will receive an annual dose of about 5 kGy for a luminosity of $5 \cdot 10^{32}$ $cm^{-2}s^{-1}$. This is well below the limit for silicon detectors. At the inner edge, the pad occupancy is a manageable 4%.

3.6 Drift Chambers

3.6.1 Chamber geometry

The positions and radial dimensions of the drift chambers are shown in Fig. 1.2 and summarized in Table 3.1. Spectrometer I contains a total of 10 chambers and Spectrometer II contains 9. Chambers are positioned in both analyzing magnets to increase acceptance for wide angle and low momentum tracks.

Chamber	Position (cm)	Radius (cm)		Sense Wires
		Outer	Inner	
Spectrometer I				
1	70	110	7.0	22,000
2	90	130	9.0	26,000
3	110	150	11.0	30,000
4	145	135	14.5	26,000
5	190	135	19.0	25,000
6	265	135	26.5	23,000
7	340	135	34.0	22,000
8	420	140	7.0	28,000
9	440	145	7.0	30,000
10	460	150	7.0	31,000
Spectrometer II				
1	655	65	6.5	12,000
2	685	70	6.9	14,000
3	690	70	6.9	14,000
4	780	100	7.8	20,000
5	830	100	8.3	20,000
6	880	100	8.8	20,000
7	940	100	9.4	20,000
8	975	100	9.8	20,000
9	1010	100	10.1	20,000

Table 3.1: Chamber positions, radial dimensions and wire count.

3.6.2 Cell and module structure

We have chosen a cell structure based on the multi-drift tube design[2] consisting of a hexagonal lattice of cathode wires with anode wires centered in each hexagon. The structure of a small slice of one module is shown in Fig. 3.3. The hexagons are "stacked" (vertically in the illustration), in 5 columns, resulting in a maximum of 5 measurements per module. The distance between adjacent wires is 1.4 mm.

The wires are held only at the outer edges of the cylindrical chamber. Consequently, there will be a dead stripe whose size depends on chamber position to accommodate the beam pipe. The alternative, filling the stripe by attaching wires to a ring with radius that of the beam pipe is unnecessarily complex and adds significant material in a region of high particle density.

The chambers are constructed of 6 modules. The modules are oriented at 0°, 30°, 60°, 90°, 120°, 150° as sketched in Fig. 3.4. Six views were chosen since this leads to adequate coverage for all azimuthal angles while maintaining a manageable channel count. The channel counts for individual chambers are given in Table 3.1. The channel count for the full system is 423,000.

3.6.3 Gas filling

A 1 bar gas mixture of 20% DME, 80% Helium appears most suitable[3]. It has a radiation length of X_o = 951 m and a drift velocity of about 40 μm/nsec in

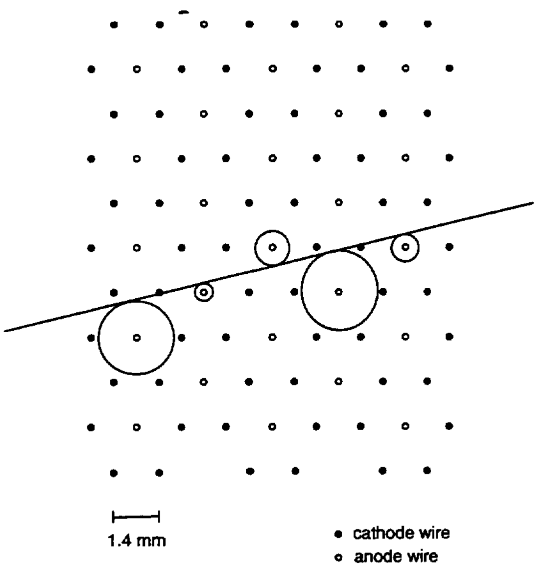

Figure 3.3: Layout of the drift chamber wires. A single cell consists of an anode wire centered on a hexagonal array of cathode wires. The spacing between adjacent wires is 1.4 mm. Each module has five such layers of hexagonal cells as shown. A trajectory is indicated. The radii of circles tangent to this trajectory indicate the measured drift distance.

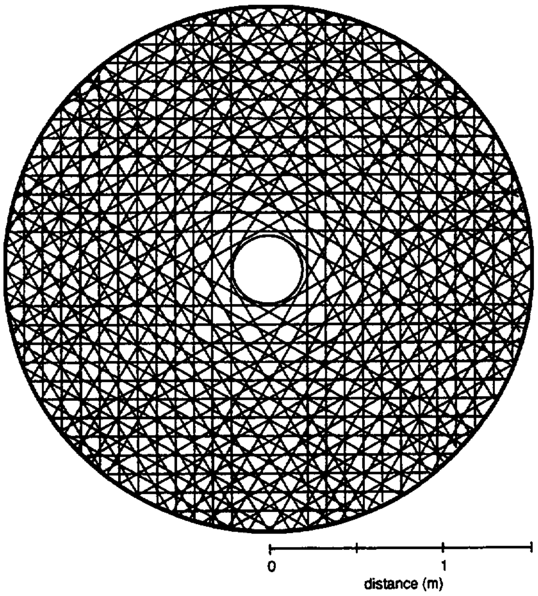

Figure 3.4: Geometry of a drift chamber as seen from the beam direction. Wires are arrayed along 6 directions at 30° intervals, producing a hexagonal symmetry. The inner circle is the beam pipe and is drawn with a radius appropriate for chamber 7 of Spectrometer I.

an electric field of 4 kV/cm[4]. The maximum drift time in our geometry is 35 nsec. A charged particle produces about 16 primary electrons per cm in this gas mixture hence, 5 for a full cell traversal.

3.6.4 Drift resolution

The multidrift tube has been shown[2] to yield a resolution of 70 μm per wire in a pure DME gas filling. With the He/DME mixture proposed here, we expect to achieve a resolution of 100 μm per wire or better. Because of the dead stripe in each view, the number of views per module with hit information and thus the point resolution, is a function of azimuth and $r_\perp$. Assuming a drift resolution of 100 μm per wire and (conservatively) an overall hit efficiency of 90% per wire, we calculate a localization accuracy, per 6-view module of about 30 μm or better in both vertical and horizontal directions, for most chambers. The worst resolution, about 50 μm, is seen near the beam pipe in chamber 5 of Spectrometer I.

3.6.5 Two track separation

For a 2.8 mm drift cell, the average occupancy is $.88/r_\perp$ particles per cell (see Sect 3.2). The occupancy of the cell closest to the beam will be .20. The probability of more than one track traversing this cell is 2%. This, and the high degree of redundancy in the chamber system will ensure a negligible loss of events due to track overlap.

3.6.6 Rate capability and aging

The very small cell size and high electric field (> 4 kV/cm in our configuration) of the multidrift cell endow it with far greater immunity to space-charge gain reduction than conventional proportional chambers. Bouclier et al.[2] have observed gain reductions of less than 10% for a particle flux equivalent to 10^6 minimum ionizing particles per second per cm^2 using a DME gas filling. This flux corresponds to the maximum anticipated flux at a distance of 6 cm from the beam and maximum luminosity of $5 \cdot 10^{32}$ cm^{-2}s^{-1}.

DME gas mixtures show excellent aging characteristics, provided suitable materials and high-purity DME are used. Bouclier et al.[2] report that counters survive without noticeable modification of gain up to integrated currents above 1 C/cm. At a gas gain of 10^5, the maximum yearly charge seen by the COBEX chambers is .05 C, thus the chamber lifetime is at least 20 years.

3.6.7 Electronics

Low noise preamplifiers are mounted directly on the chamber frames. Ten meters away a two stage amplifier is used where a 2 nsec clipping and integration (1/t cancellation) is performed. A discriminator (with threshold set at 2 electrons on the sense wire) drives an 6-bit TDC. No pulse amplitude analysis is performed.

3.7 Resolution and Pattern Recognition

3.7.1 Pattern recognition in the quadrupole spectrometer

Full track reconstruction has been performed in the quadrupole spectrometer. The starting point for this is the set of 3-dimensional hit positions in the 10 measuring stations positioned upstream, inside and downstream of the quadrupole. These hit positions are taken from the Monte Carlo digitizations, and include the effects of multiple scattering and chamber resolution, but not those of chamber inefficiencies or noise. Software is in preparation for the reconstruction of these "space" points in the chambers, but is, at the time of writing, incomplete. The track-finding algorithm proceeds as follows.

As an initial step, straight track segments are reconstructed in the three chambers upstream of the quadrupole, based on the track-roads technique. This is a simple task, as the mean track multiplicity in these chambers is about 20 per event. Pairing hits in chambers 1 and 3, corresponding hits are looked-for in chamber 2 with a road width of 0.12 cm in both projections. Using only tracks which have a physical intersection with all three stations and have an origin with $|z| < 30$ cm, and momentum greater than 0.2 GeV/c, a segment finding efficiency of 99.4% is obtained. Essentially all the inefficiency is for low momentum tracks (<0.5 GeV/c) at large azimuthal angles, which are not reconstructible in the rest of the spectrometer anyway. A contamination of 2.7% "ghost" segments is found, but the majority of these fail to have associated tracks in the rest of the spectrometer.

The second step of the track finding is to look for hits in the remaining chambers (4-10) which correspond to the reconstructed upstream segments. As the momentum of a given segment is unknown, no unique hit positions can *a priori* be predicted in the downstream stations. However, for a given segment, a "candidate" may be found by associating with it a hit in a reference station downstream. The position of this hit in one projection defines a momentum for the candidate, and this momentum constrains the position in the other projection, providing a criterion for acceptance or rejection of the candidate. In this way, all combinations of segments and points in the reference station may be tested, with only a small proportion surviving. These will either be genuine combinations or random coincidences. The size of the road used for testing of the criterion is dictated by the spatial resolution in the reference station, the resolution on the parameters of the segment, the effects of multiple scattering and deviations of the magnetic field from the model used (none in this simulation). The larger it is however, the more ghost combinations will be accepted.

As tracks may propagate out of the quadrupole at any point along its length, the reference station to be used for the above analysis may not be too far downstream, otherwise large acceptance loss will result. On the other hand, if it is too far upstream, the momentum resolution is too poor to allow a narrow road to be defined. Based on the nominal angular acceptance of COBEX of 600 mrad, station 5 is used as the reference plane. The road width for the second projection is defined by the requirement of maximization of the track-finding efficiency, resulting in a value of 0.5 cm. With this conservative approach, a relatively large number of ghost combinations results. These are reduced significantly however by the requirement of a corresponding hit in station 4, this providing two additional constraints, one in each projection. In this way, good efficiency and small ghost contamination are obtained, as described below.

According to the above discussion, a reconstructed track is defined as one which has consistent hits in at least stations 1-5. If it satisfies this condition, it is accepted. With all its parameters defined, hits are searched for in the remaining downstream stations, and are included where found. In fact, where tracks pass through chamber 6, the momentum is recalculated, to allow the road width to be reduced somewhat in later planes.

Finally, in order to reduce further the contribution of ghost tracks, where more than one track uses the same hit in station 3, only the one which uses the maximum number of hits is used, as this is the least likely to be a ghost.

With our definition of a track, only tracks which intersect all of chambers 1-5 are reconstructible. In order to define the track-finding efficiency therefore, as well as the momentum and vertex position requirements listed above for segments, only Monte Carlo tracks which intersect stations 1-5 are used to test the algorithm. Out of these, we find an efficiency of 99% with a ghost contamination of 1%.

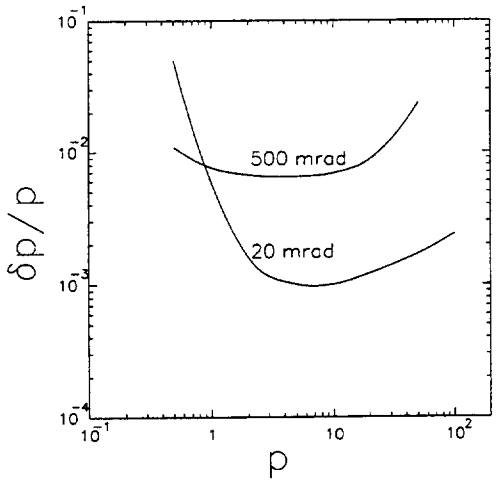

Figure 3.5: Average momentum resolution ($\delta p/p$) versus track momentum for incident polar angles of 20 mrad and 500 mrad. The angles chosen provide the effective upper and lower limits on the resolution of the spectrometer.

3.7.2 Momentum resolution

Figure 3.5 shows the average momentum resolution of the COBEX spectrometer system as a function of momentum for two incident angles. The angles, 20 mrad and 500 mrad, were chosen to indicate the effective limits of the spectrometer resolution. The momentum resolution was measured by transporting particles through the spectrometers using the COBEX Monte Carlo and fitting a charged particle trajectory to the simulated chamber hit information[1]. Vertex information was not included in the track fits, even though doing so could significantly improve the momentum resolution in some cases.

Low momentum, small angle tracks are bent by the quadrupole field and measured by the chambers inside and behind the quadrupole magnet. This results in a poor momentum resolution for such tracks. With increasing momentum, the small angle tracks are measured more often by the dipole spectrometer with an increasingly good resolution. At a momentum of ~ 5 GeV the resolution reaches the multiple scattering limit for the dipole spectrometer of $\delta p/p \approx 10^{-3}$. The resolution of higher momentum particles ($P > 20$ GeV) is limited by the chamber resolution at $\delta p/p \approx 3 \cdot 10^{-5} p$.

At much larger angles (as demonstrated by the 500 mrad curve), low momentum particles pass through the chambers in front of and inside of the quadrupole, but tend to be bent out of the first spectrometer before the end of the magnet. With increasing momentum a larger fraction the tracks will pass through the magnet to be measured by the following chambers, thus ameliorating the resolution. This tendency is not very pronounced in the 500mr tracks since they are so close to the magnet wall, even high momentum particles are lost. This more than compensates the higher fields at large angle to make the 500mr curve an upper limit on the resolution.

3.7.3 Mass resolution

The B–mass resolution depends strongly on the final-state multiplicity of the decay mode under study. The reconstruction of a variety of decay modes has been studied (see Sect. 9), including $B_d \to J/\psi K^o_s$, with a multiplicity of 4 and $B_s \to D_s^- \pi^+\pi^+\pi^-, D_s \to K^+K^-\pi^-$, with a multiplicity of 6. The mass distributions for these modes are shown in Figs. 9.1 and 9.2. The r.m.s. widths are 7.7 MeV and 10.3 MeV, respectively.

References

[1] A.Dael, C.Lesmond, Y.Pabot, J.M.Rifflet, DAPNIA Report 5.93.276A (1993).

[2] R.Bouclier et al., Nucl. Instrum. & Methods **A283** (1989) 509.

[3] A.Sharma and F. Sauli, CERN-PPE/93-51, (1993).

[4] F. Sauli, private communication.

---

[1] The COBEX Monte Carlo and track fitting packages are described in section 9.1.

4 Silicon Microvertex Detector

4.1 Design Requirements

The silicon microvertex detector, shown installed inside the vacuum pipe at the center of the interaction region in Fig. 1.2, has been the subject of extensive R&D efforts[1] by our collaboration for several years. It is a development which allows microvertex detector capability to be added to any forward detector through which a storage ring beam pipe must pass; the interactions could be beam-beam, as in this proposal[2], beam-wire[3] or beam-gas jet[4].

For use with a forward detector, the essential requirements are the following:

- Silicon detector planes are perpendicular to the circulating beams.

- A gap or hole in the detector planes is needed, through which the circulating beams can pass without obstruction.

- The planes are mounted inside the machine vacuum, on Roman pot devices, so that they can be positioned an appropriate distance from the beam to achieve the desired minimum angle coverage, and be retracted during beam manipulation.

- In order to shield the silicon detectors against RF pickup, due to the circulating charge bunches, the silicon detectors are covered by a thin aluminum window. In order to avoid collapse (actually, "blowout") of the window, the silicon detectors must operate in a secondary vacuum.

In a collider experiment, with a beam-beam longitudinal source size of length 5 cm or more, the following requirements must also be met;

- In order to minimize the extrapolation distance to all possible interaction vertices, the silicon system is positioned at the center of the interaction region and the horizontal distance between planes is about 4 cm.

- Silicon planes are also distributed beyond the source size, in order to have complete acceptance and good track definition. In particular, the minimum angle acceptance must match that of Spectrometer II in Fig. 1.2.

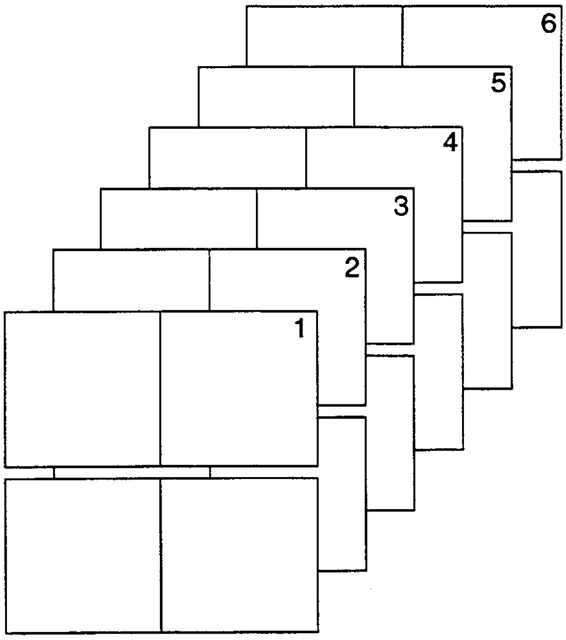

Figure 4.1: Sketch of the P238 silicon detector configuration. 48 4.5 cm square detectors are organized into six planes perpendicular to the beam axis, each with four quadrants. Each quadrant has independent x and y detectors, back to back, separated by 2 mm. The beam enters perpendicular to the page at the center of the gap between the upper and lower sections.

Fig. 4.1 shows a sketch of the 6-plane 43,000 channel silicon-strip system, that was constructed at CERN in 1990 by the P238 collaboration[1], and run in intersection LSS5 at the $Sp\bar{p}S$-Collider from Sept.-Dec. 1990. Each of the 6 planes comprised four quadrants of 4.5 cm square detectors (50 μm pitch) with independent x and y planes back-to-back. The circulating beams pass through the slot between upper and lower sections at the center of the system and are perpendicular to the system.

Since the details of the design and construction of the P238 system are described in Ref. [1], we just summarize the essential features here. We then discuss the differences between the P238 system and what we propose to build for the full COBEX experiment at LHC. One point that we can immediately mention is that the full LHC system will contain 16 planes, with 4 cm separation between planes.

Fig. 4.2 is a sketch of the installation of the P238 silicon detector in the Roman-pot system The 6 silicon planes are the vertical lines just above and below the beam line. The actual pots, with 2 mm wall thickness, are shown by the thin vertical lines close to the bellows. The pot bottoms (sides closest to the beam line) are closed by the undulating 200 μm thick aluminum window, shown by the thin lines in the figure. The reason for using an undulating window of that type, rather than simply a square box bottom, is that this design minimizes the material closest to the beam and also reduces the interactions of small angle tracks.

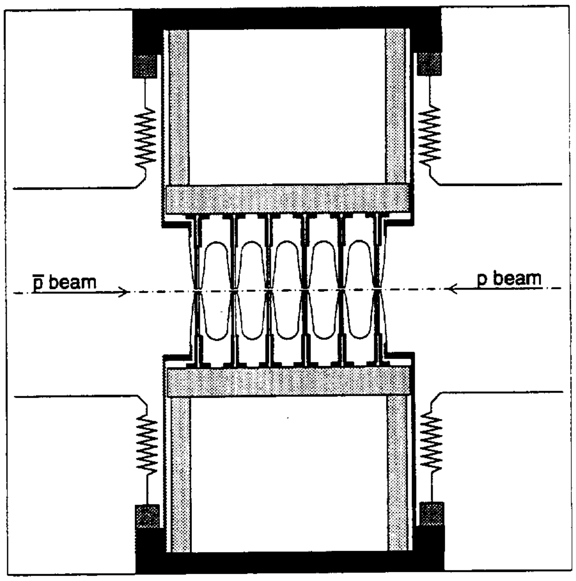

Figure 4.2: Side View of the full detector assembly and Roman pots[1]. The edges of the 200 μm-thick aluminum RF shields closest to the beam (shown as the thin curved lines near the silicon detectors) normally ran at a distance of 1.5 mm from the circulating beams (corresponding to a 3 mm gap). The black horizontal pieces at top and bottom of figure are the vacuum bulkheads bolted to the Roman pots. The grey sections form the support structure for the silicon detectors. The bellows (zig-zag lines) allow pot movements in the vertical direction.

Fig. 4.3 shows an enlargement of two silicon detector half-planes. The outer edge of the aluminum window was positioned 1.5 mm from the center of the circulating beams. There was an additional 1.6 mm "dead space" from that point to the first sensitive silicon strip. This dead space consisted of the 200 μm aluminum thickness, 900 μm gap between inner aluminum wall and edge of silicon plus an additional 500 μm in the silicon. As discussed below, all these distances can be reduced by a factor of two in the future version constructed for COBEX.

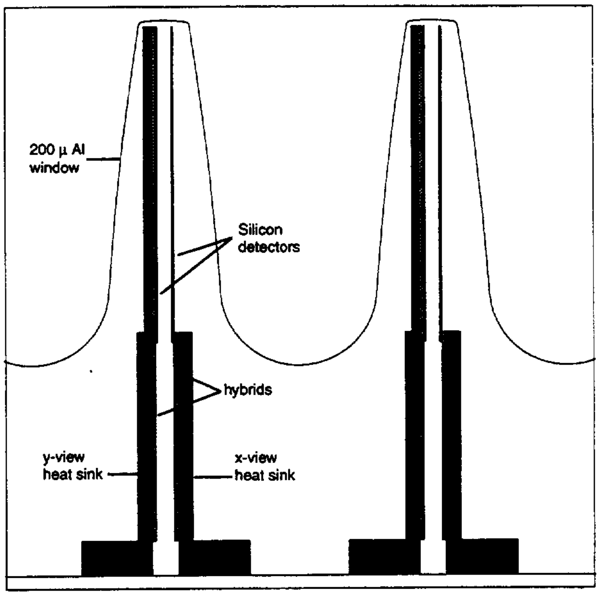

Figure 4.3: Side View showing two planes in a half-detector. The y-view detectors for each plane are on the left of the corresponding x-view detectors. The readout hybrids are glued to aluminum brackets which are bolted to the water-cooled base plate, and also serve as heat sinks.

4.2 Run Experience

The most remarkable thing about the P238 experience was that the system behaved exactly as expected. There were no surprises. Some 7-million minimum bias events were recorded on tape during the P238 run. The cleanliness of the events demonstrated that the silicon detector could be run routinely with the aluminum shield only 1.5 mm from the circulating beams with no detectable RF pickup and no significant beam halo particles. 1.5 mm corresponds to 20 beam widths (20σ) and thus the detectors were not expected to be at risk. In practice, the stability of the pot mechanism and of the beam orbits gave no cause for concern.

The general cleanliness of the events is demonstrated, for example, by the top view of a typical event in Fig. 4.4. Essentially all hits are track related. The relatively small size of the silicon detectors (4.5 cm square in the P238 system, but perhaps 5 cm square in a larger system) led to an impressive signal to noise ratio of about 25 for almost all detectors.

Fig. 4.5 with a side view of a typical P238 event, whose vertex occurs near the center of the detector, illustrates several important features of the proposed

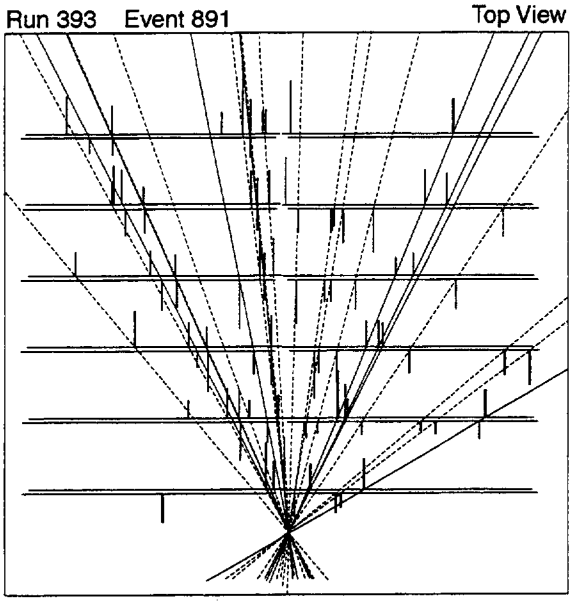

Figure 4.4: Top view of a typical high-multiplicity event in P238[1]. Silicon detectors are represented by horizontal lines. Distances between planes are 3.8 cm; the total detector width is 2 x 4.5 cm. Found clusters are shown as vertical lines, with length and width proportional to the cluster pulse height and width, respectively. Signals are shown if they are larger than 4σ(noise). Solid (dashed) lines are tracks in the upper (lower) half detector.

system:

- tracks are seen in both hemispheres and aid in the primary vertex determination (even though there is a spectrometer system only on one side).
- Because the silicon detectors are in a field-free region, straight line tracks are easily found in real time, and extrapolated to X = Y = 0 to obtain an online estimate of the longitudinal (Z) vertex position.
- Analysis of our P238 real data has shown that X,Y,Z of the primary vertex can be determined online with uncertainties $(\sigma_x, \sigma_y, \sigma_z) = (30, 30, 210)$ μm, respectively. As discussed in Chapt. 8, this allows a very effective trigger algorithm to be implemented in real time. The better determination of the primary vertex position offline, when momentum knowledge of the tracks can be utilized, results in a determination of the B-meson flight path, with an uncertainty, $\sigma = 108$ μm. This leads to an uncertainty in measurement of an event's proper time of $\sigma(\tau)/\tau = 5\%$.

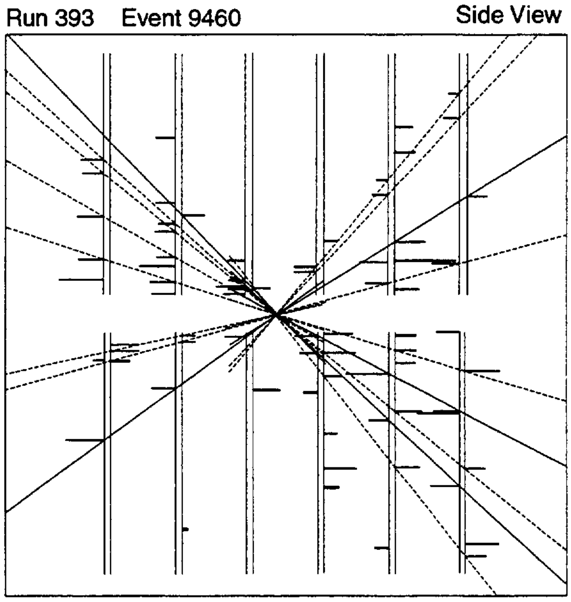

Figure 4.5: Side view of a P238 event whose vertex is near the center of the detector. Tracks in both forward and backward hemispheres are seen. Transverse and longitudinal vertex positions (x, y, z) can be determined online with errors of 30, 36 and 210 μm, respectively.

Fig. 4.6 shows the offline vertex distributions in the transverse directions, which profile the beam rather well. The pots could be repositioned for each run, after stable beams were achieved, with a precision of about 25 μm. During the course of a run, the SPS beams varied by less than ±100 μm in the vertical and horizontal directions with respect to our detectors. It is important to note that this is essentially a "self-calibrating" system, in that it takes only a small number of events to determine online where the beam is with respect to the detector at the beginning of each run. These constants are input to the trigger processor discussed in Chapt. 8.

There are several additional technical advantages of the system sketched in Fig. 4.2. Since the silicon detectors operate in a secondary vacuum, separated from the main machine vacuum (and the circulating beams) by the 200 μm aluminum RF shield, the extraction of signals from the large silicon system proved to be relatively simple. Because of the secondary vacuum, there were rather minimal requirements on the quality of the feed-throughs.

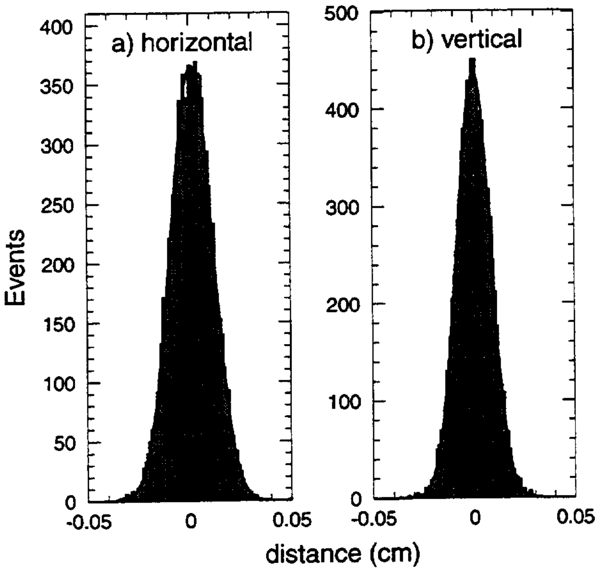

Figure 4.6: (a) x and (b) y vertex distributions for a large sample of events. The curves are Gaussian fits with σ = 100 and 84 μm, respectively. After unfolding a resolution error of 30 μm from the y-distribution, a beam σ of 76 μm is found.

4.3 Beam Halo Measurements

Although the events were visually very clean, we attempted to obtain a quantitative measure of the number of beam halo tracks which traversed the detector per beam-beam interaction. For a sample of minimum bias P238 data, Fig. 4.7 (upper) shows the slope (in 3-dimensions) between the normal to the silicon planes and all tracks which had a projected impact parameter larger than 1 mm from a found vertex. The spike at zero are identified as halo tracks.

The halo candidates are selected by requiring a slope less than 0.005. Fig. 4.7 (lower) shows the integral number of halo tracks versus time for several different runs. The worst case run corresponded to about 1 halo track per 100 interactions. In any case, such halo tracks present no problems at all to the topology trigger discussed in Chapt. 8, because their impact parameter results in their being rejected by the algorithm.

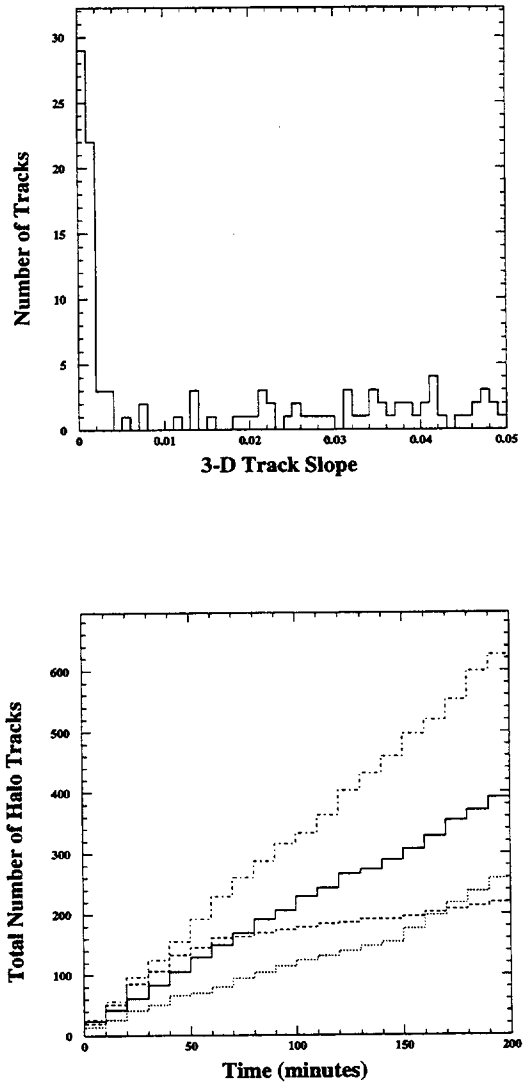

Figure 4.7: Upper plot: Candidates for halo tracks which have more than 1 mm impact parameter with a primary vertex. The quantity plotted is the 3-dimensional angle between the track direction and the normal to the silicon detectors. The peak at zero contains halo tracks. Lower plot: integral number of halo tracks versus time during four different fills. the upper curve corresponds to one halo track per 100 events.

4.4 Simulation of the Silicon Data

We have modeled the P238 minimum bias silicon data using the event generator PYTHIA 5.6[5] and GEANT 3.14[6]. We could then test the reliability of the Monte Carlo calculations by comparing the Monte Carlo events with the real data. For example, Fig. 4.8 shows such a comparison. The quantity plotted is the fraction of events with a χ^2 value larger than the abscissa value. As discussed in some detail in Chapt. 8, the χ^2 is formed from the projected impact parameters of the tracks with respect to the primary vertex and tests the hypothesis that the tracks come from a single vertex. The essential point is that it demonstrates the reliability of our Monte Carlo calculations. Were this detector not a truncated 6-plane system, Fig. 4.8 would be the the minimum bias suppression obtained offline. See chapter 8 for detailed Monte Carlo calculations of the trigger efficiency using the silicon system.

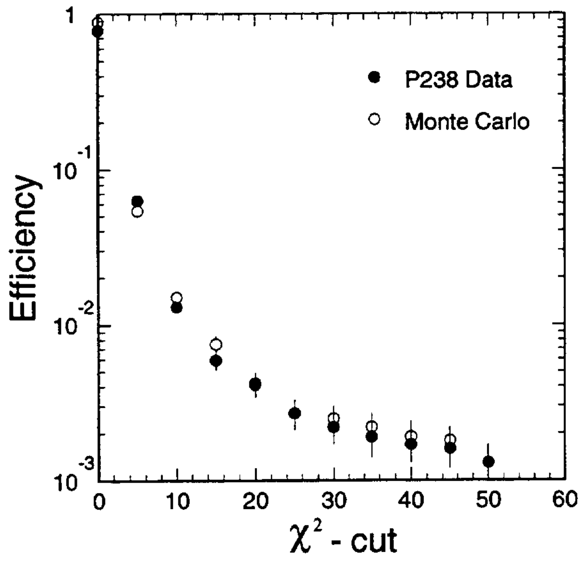

Figure 4.8: Trigger efficiency vs. χ^2 for the 6-plane P238 silicon system. Real data are compared with Monte Carlo predictions.

4.5 The COBEX Silicon System for LHC

For LHC, the silicon support structure has to be redesigned to allow track clearance up to 600mrad. The aluminum window thickness will be reduced to 100 μm, contributing to decreasing the "dead space" between the inner edge of the aluminum window and the first silicon strip. The gap between silicon and aluminum will be reduced to 400 μm and it should be possible [7] to reduce the dead space in the silicon from 500 μm to 250 μm. Thus, the total dead space in the new system would be 0.8 mm in place of the 1.6 mm in P238.

Double sided silicon detectors will be used with the addition of the best available pixel detectors at the time. Faster readout chip electronics that can cope with the 25 nsec bunch spacing will also be utilized.

References

[1] J. Ellett et al. [P238 Collaboration], Nucl. Instrum. & Methods **A317** (1992) 28.

[2] S. Erhan et al. [COBEX Collaboration], Nucl. Instrum. & Methods **A333** (1993) 101.

[3] W. Hofmann [HERA-B Collaboration], Nucl. Instrum. & Methods **A333** (1993) 153.

[4] Y. Lemoigne [GAJET Collaboration], Nucl. Instrum. & Methods **A333** (1993) 113.

[5] T. Sjöstrand, Computer Physics Comm. **46** (1986) 43.

[6] R. Brun et al., GEANT3, CERN Program Library: W5013, (Nov. 1990).

[7] P. Weilhammer, private communication.

5 Ring Imaging Cherenkov Counters

Particle identification will be accomplished with a system of focused liquid and gas Ring Imaging Cherenkov (RICH) counters, supplemented by electromagnetic calorimeters and muon filters. The RICH counters are designed to identify almost all hadrons from B decays as well as leptons below 10 GeV/c.

The geometries of the RICH counters are indicated in Fig 1.2. In Spectrometer I, a focused liquid RICH counter is positioned immediately following the pixel chamber, between $z \approx 0.35$ m and 0.65 m from the intersection. A gas RICH counter is positioned behind the quadrupole, at $z = 4.65$ m. In Spectrometer II, the gas RICH counter occupies the region from $z =$ 4.65 m to 6.30 m, and is followed by a focused liquid RICH counter.

5.1 Description of the Proposed Technology

We propose to use a variant of the recently developed RICH detectors with fast-cathode pad photon detectors[1, 2, 3]. In summer 1993 such a RICH prototype was successfully tested at CERN in a π testbeam [4]. The module tested was a proximity focused counter with a solid LiF radiator. The Cherenkov angle resolution obtained was 14 mrad, near to the expected resolution of 12 mrad from an analytic calculation. In all other respects, its response was as predicted, with little noise and no photon feedback.

The detector plane, a photon-sensitive asymmetric MWPC with cathode-pad readout, is sketched in Fig. 5.1. It consists of a 3 mm thick fused quartz window whose inner surface is coated with 100 μm metallic strips with 1.5 mm pitch (7% opacity) which define an equipotential surface. This is followed by a plane of 50 μm anode wires with a 1.24 mm spacing. A plane of 5 mm × 6.6 mm cathode pads is positioned 0.5 mm below. The cathode pad plane is coated with a CsI/TMAE photon converter. The readout electronics are mounted on the back side of the detector plane and are 34 mm deep.

5.2 Liquid RICH Counters

A preliminary design for the Spectrometer I focused liquid RICH calls for an 8-fold azimuthal segmentation of both focusing mirror and detector plane. A cross-section through one such segment is shown in Fig. 5.2. The Spectrometer II liquid RICH is similar, differing only in radial dimensions.

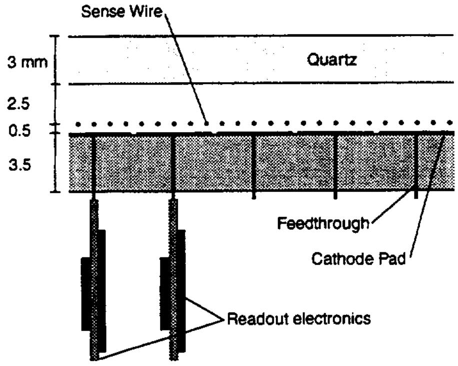

Figure 5.1: Side view of a photon detector. The underside of the quartz window is an equipotential surface. Anode wires are arrayed 2.5 mm below and CsI/TMAE-coated cathode pads are a further 0.5 mm. Two readout modules are shown.

The focusing mirror has a radius of 1.5 m and is positioned about 20 cm behind the detector plane. The 1 cm thick C_6F_{14} liquid radiator follows the contour of the mirror and is held in place by a 3 mm thick fused quartz window. The detector angle and mirror position are optimized for a track of 250 mrad. The detector plane is of the type described in Section 5.1. The material in the liquid RICH counter is 15% of a radiation length. This can probably be reduced to 12%.

The expected performance of the liquid RICH counters is shown in Table 5.1. The number of photoelectrons obtained and the 3σ momentum limits on π/K separation shown assume a detector plane of infinite area. The images of tracks will however be truncated by the finite radial extent of the real detector (see Fig. 5.2), resulting in a loss of up to half the produced light. Since the 3σ limits vary as the inverse fourth root of the number of photoelectrons, the upper limits for some angles will be up to 18% less than the values indicated.

5.3 Gas RICH Counters

Both gas RICH counters have photon detectors of the type described in Sect. 5.1 at their upstream ends, followed by gas radiators, then focusing mirrors. The gas radiators are 75 cm of C_5F_{12} ($\gamma_T = 16.3$) in Spectrometer I, and 165 cm of a mixture of C_5F_{12} and CF_4 with $\gamma_T = 28.8$ in Spectrometer II. The gas counter optics do not require mirror segmentation but practical considerations will force segmentation into a manageable number of pieces (probably eight).

The performance of the gas counters is summarized

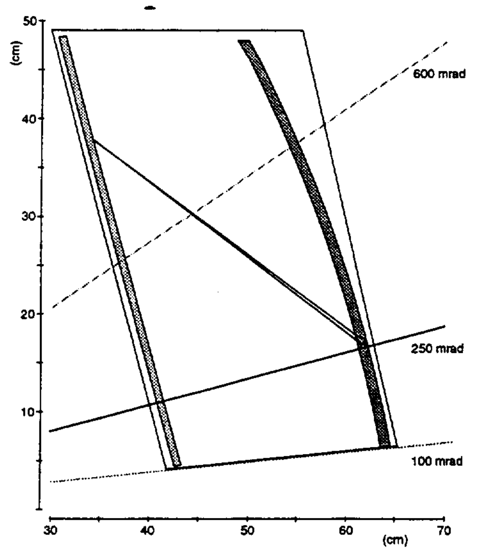

Figure 5.2: A cross-section through a segment of the Spectrometer I liquid RICH counter. The focusing mirror is positioned about 20 cm behind a detector plane. A 1 cm thick C_6F_{14} liquid radiator follows the mirror's contour. The detector plane is inclined at 260 mrad from the vertical. The trajectories of a 250 mrad track and two Cherenkov photons are indicated.

in Table 5.2. The table demonstrates that the performance is uniform, with little dependence on track angle: the 3σ upper limits for π/K discrimination vary by 10% over the aperture of the Spectrometer I counter and negligibly over the Spectrometer II aperture.

The Cherenkov angle resolutions are dominated by the contribution due to photon measurement error, i.e. pad size, particularly in Spectrometer II. It is possible to reduce this error by reading out the anode wires as well as the cathode strips. Photons which give a single cathode hit would then be measured with higher precision using the hit wire position. We estimate that this would, for example, push the 3σ momentum limit for π/K separation up to 90 GeV in Spectrometer II. Reducing the pad size to 5 mm × 5 mm and reading out the anodes would push this 3σ limit to 100 GeV.

5.4 Summary

Fig 5.3 shows the momentum ranges for unique identification amongst particle pairs in the liquid and gas radiators. Between the Cherenkov thresholds for any particle pair, discrimination is based on the presence or absence of light. Above both thresholds, an estimate of the Cherenkov angle must be made. The indicated upper limits are the highest momenta for which a 3σ difference between predicted Cherenkov angles for two particle types can be measured. For the liquid radiator, the upper limit for π/K separation is shown as 8.5 GeV. The corresponding numbers in Table 5.1 are for the most part above this, but do not include light loss due to finite photon detector size. For the gas radiators, the limits shown correspond to those in Table 5.2 since light loss is limited to a small region near the counter walls.

The number of channels for all RICH counters is summarized in Table 5.3. The total channel count of 800,000 is largely dominated by the Spectrometer I gas RICH counter.

θ	σ_θ (mrad)				n_{pe}	$P_{\pi/K}$ GeV
	pad	z_e	tot.	ave.		
0°	1.04	.0003	2.81	2.81	33	9.8
5°	0.48– 1.89	0.02– 1.35	2.77– 3.50	2.97	33	9.5
10°	0.21– 3.39	0.09– 3.77	2.79– 5.72	3.42	32	8.8
15°	0.41– 7.71	0.78– 11.0	2.84– 13.8	4.77	23	6.8

Table 5.1: Performance of the liquid RICH counter as a function of incident track angle relative to the normal to the detector. The full ranges of pixel width, photon-emission-point, and total resolutions as a function of azimuthal Cherenkov angle are given, followed by the total error, averaged over azimuth, the number of photoelectrons, assuming an infinite detector plane and the maximum momenta for π/K separation to (3σ).

References

[1] J. Seguinot, T. Ypsilantis, CERN-LAA/PI/91-004, 3/3/91, Nucl. Instrum. & Methods, in press.

[2] R. Arnold et. al., Nucl. Instrum. & Methods **A314** (1992) 465.

[3] M. French et. al., Nucl. Instrum. & Methods **A324** (1993) 511.

[4] The Fast RICH collaboration, College de France, Strasbourg, PSI, RAL, KEK, to be published.

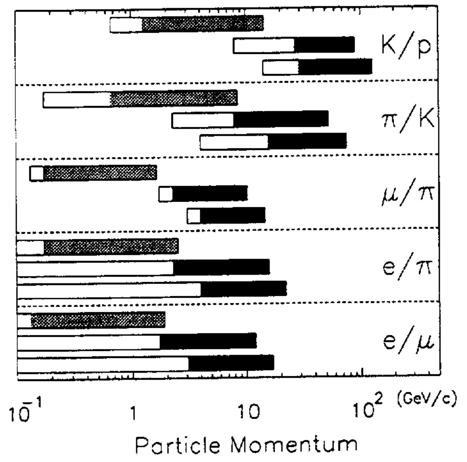

Figure 5.3: Momentum Ranges of RICH Counter Identification. For each indicated pair of particles, the upper bar in each set indicates the range of the liquid RICH counters and the lower bars are the ranges of the gas RICH counters in Spectrometers I and II. In all cases, the open bars show the momentum range between the thresholds for the lighter and heavier particles. The 3σ separation upper limits are indicated by the end of the solid bars.

θ	σ_θ (mrad)			n_{pe}	$P_{\pi/K}$ GeV
	pad	(E)	average		
Spectrometer I					
0°	0.77	0.35	0.85	16	54.3
5°	0.77	0.35	0.85	16	54.1
10°	0.77	0.35	0.90	16	52.7
15°	0.77	0.35	1.03	16	48.9
Spectrometer II					
0°	0.59	0.21	0.62	9	75.5
2°	0.59	0.21	0.62	9	75.4
4°	0.59	0.21	0.62	9	75.4
6°	0.59	0.21	0.61	9	75.3

Table 5.2: Expected performance of the gas RICH counters as a function of incident track angle. For each track angle, two contributions to the angular resolution on the Cherenkov angle are given (photon position measurement and chromatic aberration) followed by the total resolution per photon, averaged over azimuth, the number of photoelectrons and the 3σ momentum limits for π/K separation.

Spect.	Type	Radius (m)	Pixel Size mm × mm	Channel Count
I	Liquid	0.5	$5 \cdot 5$	$3.1 \cdot 10^4$
II	Liquid	0.6	$5 \cdot 5$	$4.5 \cdot 10^4$
I	Gas	1.7	$3 \cdot 4$	$6.6 \cdot 10^5$
II	Gas	0.5	$3 \cdot 4$	$6.5 \cdot 10^4$

Table 5.3: Number of channels in each RICH counter.

6 Electromagnetic Calorimeter

The design goals of the electromagnetic calorimeter system are:

- to provide electron identification for particle momenta above the effective range of the RICH system over the full spectrometer aperture,
- to provide precise γ four-vectors for high resolution mass reconstruction of B decays containing a single γ or a single π^o over part of the spectrometer aperture.

6.1 Geometry

As shown in Fig. 1.2, the calorimeter coverage is divided into 3 angular regions:

- **350 mrad to 600 mrad:** The angular region subtended by the quadrupole magnet is covered by a relatively low-resolution cylindrical calorimeter which lines the inside of the magnet.
- **100 mrad to 350 mrad:** This angular region is covered by a high-resolution calorimeter located at $z = 5.4$ m.
- **below 100 mrad:** This angular region is covered by a high-resolution calorimeter located at $z = 10.1$ m.

6.2 The Quadrupole Calorimeter

The region between 600 mrad and 350 mrad ($1.2 < \eta < 1.7$) will be covered by calorimetry used only for electron/hadron separation. The calorimeter will line the inside of the quadrupole and will consist of an array of 1 mm tungsten / 4 mm scintillator sandwiches running the length of the quadrupole and viewed at each end by a phototube. The longitudinal position is inferred from the ratio of pulse heights.

The azimuthal segmentation will be about 10 cm, for a module count of 94. The use of tungsten allows for a compact device: 9 radiation lengths in a thickness of 15 cm. The average number of charged particles and photons per event in this rapidity range is 6 (combined), thus the average occupancy is 6%.

The need for this calorimeter has not been firmly established. It is meant as a supplement to the Spectrometer I liquid RICH counter which ceases to provide effective electron/hadron separation above 2 to 3 GeV. If, after further simulation, it is found that this calorimeter does not add substantially to the yield of tagged, reconstructed B mesons, it will not be built.

6.3 Calorimetry Below 350 mrad

The aperture below 350 mrad will be covered by high-resolution radiation-hard electromagnetic calorimetry. The principle design problem for the forward calorimetery is the high radiation dose.

6.3.1 Lead Tungstenate

The calorimeter medium which comes closest to satisfying our requirements is $PbWO_4$ crystals. The task of understanding the properties of these crystals has only recently begun[1] and considerable progress is still being made [2]. To date, these crystals have been shown [3] to have energy resolution of $\sigma(E)/E = .03/\sqrt{E} \oplus .064/E$, with E in GeV.

The light produced is a combination of Cherenkov light and three components of scintillation light with time constants $\tau = 2$ ns(30%), 7 ns(35%) and 35 ns(35%). The emission spectrum is centered at 480 nm and has a full width of 130 nm. The radiation length is 0.9 cm.

$PbWO_4$ crystals have been shown to be extremely radiation resistant. Up to doses of 10^4 Gy, the optical properties remain nearly unchanged and for a dose of 10^6 Gy, the transmission decreases by no more than 30%. Furthermore, the crystals recover quickly from radiation damage: after a period of 15 days, much of the transmission loss occurring after irradiation to 10^6 Gy is recovered. The subject of radiation damage to these crystals is being actively pursued. It is of particular interest to understand their behavior when gradually accumulating a large radiation dose over a period of a year or more. The observed self-annealing effects imply that the radiation limits in the LHC operating environment are likely be 10^5 Gy or more.

6.3.2 Cell structure

The cells will have square cross-section and a length of 22 cm ($\approx$ 25 radiation lengths). The choice of granularity must be based on considerations of π^o opening angle, cell population, γ position, resolution and cost. This matter is currently under study. For the purposes of estimating channel count, we assume cell size of 4×4 cm^2 for all cells, leading to channel counts of 6,500 for Spectrometer I and 1,900 for Spectrometer II.

6.3.3 Radiation considerations

Starting from Ref. [4], we derive the following formula for the maximum yearly (i.e. an integrated luminosity of $5 \cdot 10^3$ pb^{-1}) radiation dose in Gy, to a $PbWO_4$

calorimeter:

$$dose = \frac{14.0 \cdot e^{2.9 \cdot \eta}}{z^2}$$

where η is the pseudorapidity, and z is the distance in meters from the intersection region to the front face of the calorimeter along the beam.

For the Spectrometer I calorimeter, the maximum dose rate will be 3 kGy per year at 100 mrad. This dose rate poses no particular problem for $PbWO_4$.

At the Spectrometer II minimum-angle acceptance cutoff of 10 mrad, the maximum dose will be 650 kGy per year. At 20 mrad, the maximum yearly dose will be 90 kGy and at 40 mrad, the maximum dose rate falls below 10 kGy. Thus, above 40 mrad, the calorimeter lifetime is probably at least 10 years. Between 20 mrad and 40 mrad, periodic (of order yearly) replacement of crystals may be necessary. It may prove impractical to instrument the region below 20 mrad.

6.3.4 Performance

To evaluate the contribution of calorimeter resolution to the B-mass resolution, we have simulated the final state B $\rightarrow \chi_{c2} K^o_s$, $\chi_{c2} \rightarrow J/\psi\gamma$, $J/\psi \rightarrow \mu^+\mu^-$, $K^o_s \rightarrow \pi^+\pi^-$. This final state is similar to the much-studied B $\rightarrow J/\psi K^o_s$, except that it contains a γ and an additional mass constraint which should prove useful for background discrimination.

We generate events using Pythia and restrict ourselves to those containing B-mesons whose charged decay products are within the 600 mrad aperture and whose γ is within the 10 mrad to 350 mrad calorimeter aperture. (We note in passing that if the calorimeter aperture extends to only 20 mrad, the loss in acceptance will be 15%.) We smear the γ four-vector using the energy resolution given in Sect 6.3.1 and assume a 1 cm position resolution. Using the generated four-vectors for the charged decay products and the smeared γ four-vector, we calculate the $J/\psi\gamma K^o_s$ invariant mass. Since generated four-vectors are used for the charged particles, the width of the resulting mass distribution is just the contribution of the calorimeter resolution and must be added in quadrature with the resolution due to charged particle momentum resolution. We find an r.m.s. calorimeter contribution to the B-mass resolution of 24 MeV which, when added to charged particle contribution of 7.7 MeV (see Sect. 9.2.1) results in an overall B-mass resolution of 25 MeV.

References

[1] V.G. Baryshevsky et al., Nucl. Instrum. & Methods **A322** (1992) 231.

[2] L. Nagornaya et al., Proceedings of the Int. Workshop Crystal 2000, Chamonix, France, Sept. 22-26, 1992, 367.
M. Kobayashi et al., Proceedings of the Int. Workshop Crystal 2000, Chamonix, France, Sept. 22-26, 1992, 375.
V.A. Kachanov et al., Proceedings of the Int. Workshop Crystal 2000, Chamonix, France, Sept. 22-26, 1992, 381.
L.V. Miassoedov et al., Proceedings of the Int. Workshop Crystal 2000, Chamonix, France, Sept. 22-26, 1992, 437.

[3] V.A. Kachanov, M.V. Korzhik, J.P. Peigneux, private communication.

[4] D.E. Groom et al., Nucl. Instrum. & Methods **A279** (1989) 1.

7 Muon System

A muon detection system covers the angular aperture of the second (100 mrad) spectrometer. This system serves the dual purposes of providing a fast signal for single or multiple high p_T muons (see discussion in section 8.2) and of identifying muons that are too fast to be uniquely identified by the RICH counters. A second absorber behind Spectrometer I is under consideration. This would probably not be used for triggering, but could provide needed muon identification for tagging.

The Spectrometer II muon detector consists of a 2.5 m long iron filter with gaps for measuring stations after 1.5 m, after 2 m, and at the end of the filter. The muon filter can be constructed of iron blocks leaving a square hole $\sim$ 25 cm on a side for the passage of the beam pipe. The 2.5 meters of iron correspond to 15 interaction lengths. This should be sufficient to reduce triggers from hadron punch-through to less than the background rate due to $\pi^\pm$ and $K^\pm$ decays. Also, muons typically lose 4 GeV in traversing the iron. Thus, muons of less than 4 GeV are absorbed in the iron, reducing the number of background muons detected.

Since the main purpose of the muon detector is for use as a fast trigger in a high luminosity environment, the chambers used in the system must have a time resolution of less than the bunch crossing time (25 nsec). The position resolution need only be good enough to provide adequate online resolution, and to enable the matching of the muon track to its trajectory in the spectrometer, where precision momentum and p_T determinations are made. Cathode strip readout chambers are under investigation as a detector which is intrinsically fast enough to provide a signal every beam crossing. Coarse cells of 1 cm width give an adequate online momentum resolution, as discussed below.

A fast trigger signal is provided when muon chamber hits are seen to be consistent with a $>$ 15 GeV muon. This fast trigger is generated by coincidence logic located on or near the muon chambers. Since a 15 GeV track bends by 100 mrad in the spectrometer dipole magnet, the road width is small. For example, using 1 cm readout strips on chambers separated by 50 cm, a given strip in chamber 2 needs to be combined with only 10-12 strips in each the first and third muon chambers. The coincidence logic necessary to implement this trigger is therefore quite simple.

The muon momentum resolution attainable online from the chambers in the muon detector is limited by two main effects. First, multiple scattering in the absorber smears the muon direction by $0.23\ GeV/p$. This results in a momentum resolution limit of $\delta p/p = 15\%$. With 1 cm strips, the contribution to the online momentum resolution due to the chamber resolution is $\delta p/p = 4.1 \cdot 10^{-3} p$. Additional effects which could contribute to the online resolution are the bending in the quadrupole, and an uncertainty in the interaction position. These effects should be small relative to the multiple scattering and chamber resolution contributions. Thus, the online resolution $\delta p = 2.6$ GeV at $p = 15$ GeV, the Level 0 trigger threshold.

8 Triggering & Data Acquisition

Three Level-1 triggering schemes are contemplated:

- Topology trigger (silicon) for luminosities up to $5 \cdot 10^{31}$ cm^{-2}s^{-1},
- Single muon trigger for luminosities up to $5 \cdot 10^{32}$ cm^{-2}s^{-1},
- Dimuon trigger for luminosities as high as $5 \cdot 10^{33}$ cm^{-2}s^{-1}.

Table 8.1 shows the mean number of interactions per bunch crossing for these three luminosities.

$\mathcal{L}$uminosity cm^{-2}s^{-1}	$\bar{n}$
$5 \cdot 10^{31}$	0.09
$5 \cdot 10^{32}$	0.9
$5 \cdot 10^{33}$	9

Table 8.1: Average number of inelastic interactions per bunch crossing for low and high luminosity pp running, assuming 25 nsec bunch spacing and 70 mbarn inelastic cross section.

For the "low luminosity" running, we propose to use a topology trigger which uses hit information from the silicon microvertex detector. The good efficiencies that can be obtained, coupled with the relative lack of final state bias, make this the trigger of choice for general purpose B-physics at lower luminosities. However, it becomes overwhelmed by spurious triggers from pileup effects (multiple interactions in a bunch crossing) at high luminosities.

The second is a single high-p_t muon trigger, which will work at luminosities larger than 10^{32} cm^{-2}s^{-1}, and is limited only by the rate capabilities of the data-handling hardware. Despite its lower efficiency (except for muonic B decays and especially $B \rightarrow J/\psi$ - see below), the muon trigger is perhaps the only effective general purpose B trigger at high luminosity proton-proton colliders.

The dimuon trigger will be used for maximum "reach" for the rare final state $B_s \rightarrow \mu^+\mu^-$. In this high luminosity running mode, the silicon system will be retracted to 1 cm from the beam, and the RICH counters and EM calorimetry will be removed.

In all cases, high rates of minimum bias, beauty and charm events emerge from the Level-1 trigger. It will be necessary to pass these events into a powerful online computational system, where momentum-analyzed tracks from the spectrometers will be matched with tracks in the microvertex detector. Full multi-vertex reconstruction will be done in order to select interesting events for writing to tape.

8.1 Topology Trigger

The strategy of the Level-1 topology trigger, which uses digitized silicon hit information, is to search for events which are inconsistent with having a single vertex.

Complete GEANT simulations have been made of the silicon detector response to PYTHIA-generated minimum bias, inclusive beauty and charm events and a Level-1 topology trigger algorithm was developed using these events. This algorithm provides a minimum bias suppression of 1/100 with a B-Meson efficiency of 20-50% (depending on final state multiplicity), corresponding to a beauty enhancement factor of 20 to 50. The algorithm is sufficiently concise to allow implementation in a pipelined data-driven trigger processor[1]. The suppression of minimum bias background is sufficient to allow efficient transfer of accepted events to a Level-2 trigger processor farm for further filtering.

The COBEX topology algorithm consists of the following steps:

- **Point Finding:** The raw silicon hit information is transformed into points independently in the x-z and y-z planes. A point is defined as the geometrical center of a cluster (contiguous hit strips). The average cluster width is 1.6 strips. A comparison of the points found in this way with the original track coordinates shows that they have a resolution of 16 μm (FWHM). Although the total event charged track multiplicity is high, one quadrant sees on average, less than 1/8 of the total, resulting in the rather modest mean multiplicity of 2.5 points per quadrant.
- **Track Finding:** Next, straight lines which traverse at least three planes of silicon, are found independently in both hemispheres in their x-z and y-z projections, using a road width of one silicon strip or (25 μm). This rather stringent collinearity cut corresponds to the multiple scattering of a 2 GeV/c track and thus tends to reject tracks with lower momentum which degrade the vertex algorithm. It also tends to reduce the number of ghost tracks. On average, the algorithm finds about 80 % of the tracks present, mainly losing low momentum tracks which fail the collinearity test. No attempt is made to match the views online.

- **Duplicate Rejection:** The track-finding algorithm tends to find several segments of the same track with different hit combinations. Moreover, due to the narrow road width, tracks which suffer from large multiple scattering can be found in more than one non-overlapping segment. The duplicate rejection process attempts to remove all segments but the one with a hit closest to the beam.
- **Primary Vertex Approximation:** In order to define the subset of found tracks whose origins are near the primary vertex, we need to have a first estimate of this vertex position in the longitudinal coordinate, z. This estimate is made by histogramming in 5 mm bins, the z-intercepts of all the found x-z and y-z track projections (only the two hits closest to the beam on each track are used to define the track parameters). The two adjacent bins which contain the most hits are then found and their average position, weighted by the number of hits in each bin, is taken as the preliminary primary vertex Z coordinate. This procedure yields a Z-position with an accuracy better than 1 mm. The vertex transverse positions, X and Y, are initially assumed to be zero.
- **Exclude Tracks with Projected Impact Parameters > 1mm:** Most tracks from strange particle decays as well as remaining badly-scattered and ghost tracks are removed by eliminating all tracks with projected impact parameter larger than 1 mm at the estimated primary vertex position (almost all tracks from beauty or charm decays have much smaller impact parameters).
- **χ^2 Calculation:** An improved primary vertex position is calculated from the remaining tracks by minimizing the following χ^2 for a single vertex hypothesis, using the projected track impact parameters and slope dependent weights. A large χ^2 results if the event topology is inconsistent with a single vertex hypothesis, and is therefore evidence of heavy flavor production.

$$\chi^2 = \left[\sum_{i=1}^{N_x} \frac{b_{xi}^2}{\sigma_{xi}^2}\right] + \left[\sum_{j=1}^{N_y} \frac{b_{yj}^2}{\sigma_{yj}^2}\right] \tag{23}$$

This equation contains independent sums over x and y view tracks. b_{xi} (b_{yj}) is the projected impact parameter of the i'th (j'th) track in the x (y) view. Here, the primary vertex point, which is used to evaluate the projected impact parameter, is no longer constrained to be at X = Y = 0. A weight, σ_{xi} (or σ_{yj}) is assigned to each impact parameter based on the track's slope (which gives a very rough indication of the track's momentum) and the extrapolation distance between the vertex and the closest measured point on the track.

- **Iteration:** Despite the care taken to eliminate bad tracks and tracks from strange particle decays, minimum bias events often retain one or two such tracks with large impact parameters. Since usually many more large impact parameter tracks are contained in a $B\bar{B}$ event, discarding the track with the largest contribution to the χ^2 and repeating the vertex fit, yields a larger minimum bias suppression with acceptable B efficiency. Simulation shows that the trigger selectivity is maximized after two such iterations.

8.1.1 Simulation of topology trigger

In chapter 4, we demonstrated that it is possible to make reliable Monte Carlo predictions of triggering efficiencies. Here we calculate the trigger efficiency of minimum bias events and some B-meson decays for a full 16-plane system.

Fig. 8.1 shows the the trigger efficiencies vs. χ^2 cut for minimum bias events and for three different B-meson decay modes. Demanding χ^2 larger than about 6 yields a minimum bias efficiency (suppression) of about 1/100, while the average B efficiency for the three states shown is about 30%. This is typical of this trigger algorithm. Decay modes with larger multiplicity have somewhat larger efficiencies, while decay modes such as $B_d \to \pi^+\pi^-$ have somewhat smaller efficiencies. Section 9.2 describes the trigger and reconstruction efficiencies of several B decay modes in more detail.

8.2 Single Muon Trigger

A single muon trigger will be used for acquisition during medium luminosity (up to $5 \cdot 10^{32}$ cm^{-2}s^{-1}) running. Although the muon trigger efficiency for decay modes without a final state muon is much less than that of the topology trigger, access to high luminosities and efficient tagging make muon triggering desireable.

The single muon trigger is divided into three hierarchical levels as follows:

- **Level 0, Fast Muon Detection:** Fast muons are found by looking for a track consistent with a p > 15 GeV muon in the three muon chambers. The 15 GeV minimum momentum allows

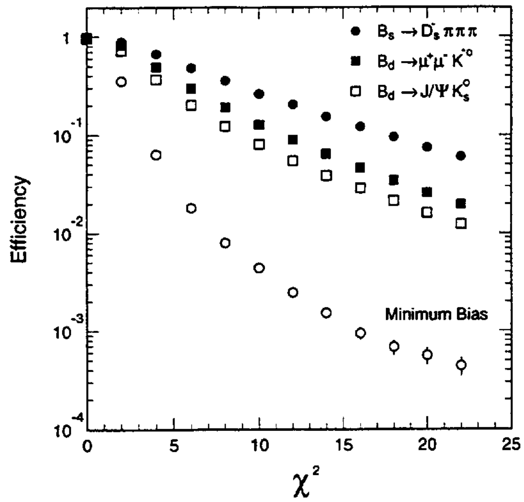

Figure 8.1: Trigger efficiency vs. χ^2-cut of topology trigger for minimum bias events and for three different B-meson final states.

all muons in the 100 mrad aperture with $p_T > 1.5$ GeV to pass the cut, and reduces the background from hadron decays by a factor of ~ 3. The Level 0 trigger rate is dominated by muons from $\pi^\pm$ and $K^\pm$ decays and hadronic punch-through, and is expected to be 3% of the minimum bias rate. This trigger level can be implemented with coincidence logic which can make a decision in the 25 nsec bunch crossing time scale, as discussed in chapter 7.

- **Level 1, $\mu\, p_T$ Requirement:** An initial calculation of the muon p_T and impact parameter in the non-bending view is made from the position and slope of the muon track in the chambers. Events are selected if a muon is found to have large p_T (typically > 1.5 GeV) and direction consistent with having come from the interaction region. Most muons from $\pi^\pm$ and $K^\pm$ decays are eliminated by these requirements. These calculations may be made using a specialized trigger processor, or within the same DDP architecture used for the topology trigger.

- **Level 2, Reconstruction in front of filter:** The muon is reconstructed through the spectrometer to verify that the Level-1 trigger particle is not a ghost track or hadronic punch-through and to refine the muon p_T estimate for a more precise cut. A DDP or a RISC processor farm can be used to make these calculations.

8.3 Dimuon Trigger

A dimuon trigger will be used at a luminosity of $5 \cdot 10^{33}$ to search for B $\rightarrow \mu^+\mu^-$ and other FCNC decays. This trigger follows the same logic as the single muon trigger, but since the level 0 trigger runs at the bunch crossing rate, will not require any additional hardware. Additional requirements will be included in Level 2 to insure that the trigger muons are of opposite charge, have a large vector sum p_T and large invariant mass.

8.4 Trigger Processors & Detector Readout

The lack of a fast highly-selective trigger requires that all detectors are read out for each bunch crossing and pipelined or stored while complex trigger calculations are made. The readout system is divided into three stages. In the first stage, each readout channel has a fast FIFO buffer that samples the detector state every bunch crossing and stores these data for at least 200nsec (8 bunch crossings) while a fast (Level-0) trigger is being calculated and distributed to all detectors. In low luminosity running, the fast trigger will be an interaction signal. At higher luminosities, the Level-0 muon trigger will be used. In either case, the fast trigger rate will be less than 4 MHz.

Detector data from events selected by Level-0 undergo digitization and zero suppression and are transferred to many FIFO buffers (one or more for each detector) for storage while the Level-1 trigger is being calculated from the silicon or muon data. The Level-1 algorithm discussed in section 8.1 will be implemented using a processor with a pipelined data-flow architecture as described in 8.4.2. With such an architecture, the processing elements are imbedded in the data readout channel. Because of its pipelined structure, the data driven processor works on different parts of several events simultaneously. This simplifies data distribution and alleviates many of the I/O bottlenecks which would occur with a more traditional processor architecture. We note that the total required computing power of the Level-1 trigger processor for the topology trigger is given by the 10^5 instructions per event, times the interaction rate of 3.5 MHz, or $3.5 \cdot 10^5$ MIPS (million instructions per second). A processor which executes a subset of this algorithm suitable for triggering a fixed target charm experiment has already been built and tested in RD21. The level 1 trigger reduces the rate to less than 50kHz.

Finally, data from events passing the Level-1 trigger are transferred from the FIFO to a processor in the level-2 farm. The level 2 processor uses all available data to fully reconstruct the event, and select those with recognizeable B decays, as described in 8.4.3. The final event sample will be written to tape.

Table 8.2 shows the numbers of detector elements, the average number of elements with hits, and the expected data lengths for each of the subdetectors in a single arm apparatus. This yields a total average data length of 44 Kbytes/event.

Detector	Elements	Hits	Noise	Length
Silicon	114700	650	600	2500
Si Pixel	32800	20	180	400
Liq Rich 1	31000	600	31	1200
Chambers 1	263000	4700	520	10500
Gas Rich 1	660000	200	660	1700
EM Cal 1	200	200	-	400
EM Cal 2	6500	6500	-	13000
Si Pixel 2	21800	20	120	300
Chambers 2	160000	4050	320	8800
Liq Rich 2	45000	500	45	1100
Gas Rich 2	65000	200	65	500
EM Cal 3	1900	1900	-	3800
μ Chambers	6000	5	10	30
Total	1407900	19545	2551	44230

Table 8.2: Number of detector elements, average number of hits, estimated noise hits, and total sparsified data length for each detector. Calorimeter channels are assumed to be read out without sparsification.

8.4.1 Detector readout system

Emphasis is being placed on concentrating as much intelligence as possible near the detector. This will result in better compaction of the detector data and hence lower data volume and higher live times. As discussed in the following paragraphs, the development of VLSI readout electronics for the RICH and Silicon is already well underway.

- **Silicon:** The silicon detectors will be read out using a high density (128 channels per IC) VLSI chip which employs sparse data scanning to minimize the number of cycles needed to read the data. The Berkeley SVX chip[3], which was developed for the CDF silicon-strip vertex detector, has many of the needed features. A COBEX readout chip, however, would have to be faster, and have several layers of buffering before the sparse readout section. The success of the present SVX and other chips gives us confidence that such an IC can be built within the required time scale.

- **Chambers:** The chamber-hit times will be encoded and recorded using a 6-bit, 1 nsec bin TDC system. Each sense wire signal is tested every 1 nsec starting from the bunch crossing (gate) signal. Hit data from each chamber pack are transferred to the FIFOs over 20-32 parallel data streams arranged to receive approximately equal amounts of data.

- **RICH:** Cherenkov photons are detected on pad detectors. The pad signals are amplified and shaped by a 16-channel VLSI chip, and latched into a 66 position shift register to store the hit data until after the Level-1 trigger decision has been made. Quantities of both VLSI chips used in the RICH readout have been manufactured, and tested with a prototype RICH counter (see Sect. 5.1).

- **Pixel Detectors:** The silicon pixel detectors will be read out with the same type of readout as the silicon strip detectors.

8.4.2 Level-1 trigger processor

A data driven processor will be used for the Level-1 calculations of the topology and muon triggers. Data driven processors have intelligence distributed in the readout channels which makes them ideal for complex computations requiring large quantities of data. They have the following properties:

- **No centralized control:** There is no central sequencer in the system. The processor consists of an array of function modules, in which the arrival of data at a module initiates its operation. Many processing units can therefore be working simultaneously on a given problem.

- **Parallel:** Several data streams are processed in parallel. In COBEX, track finding in the silicon detectors is done in parallel in 8 identical processors (4 quadrants × 2 views). Other parallelism can be intrinsic to a processor structure.

- **Pipelined:** Several events are processed simultaneously, but at different stages of the algorithm. For example, one event may be in the track finding subroutines at the same time that other events are undergoing duplicate rejection, vertex fitting, etc.

- **Expandable**- The processor may be increased to solve an arbitrarily complex problem by the addition of more modules. Since there are no resources like central memory or common I/O paths, bottlenecks do not appear. Also, because there is very little overhead, an increase in the number of processor modules yields a proportional increase in processor speed.

Some of the COBEX collaborators built and tested a data driven processor operating online with a silicon strip detector as a heavy flavor topology trigger as a part of the RD21 research project. The Data-Driven processor is based on the architecture developed by the Nevis-Univ. Mass. group [2] for Fermilab experiment E690. The processor was combined with the P238 silicon vertex detector (described in Sect. 4) and installed in the H8 beam line at the CERN SPS.

The RD21 fixed target algorithm uses many of the same techniques needed for a collider experiment, but takes advantage of the fixed target geometry, specifically the thin foil taget, to simplify the processor. We are confident that the full collider algorithm can be implemented within this architecture.

RD21 had a test run in August-September 1993, during which data were read in to the data driven processor through a specially developed silicon readout system. The processor results were exactly those expected from the processor emulation. Futher results from this run will be available soon.

For COBEX, we plan to update the RD21 technology while maintaining the principles of the data flow architecture. By employing such techniques as optical fiber data transmission, application specific integrated circuits (ASIC's), Digital signal processors (DSP), etc., we hope to improve the speed, flexibility, reliability, and ease of development and maintenence of the processor system.

8.4.3 Level-2 trigger processor

A second level of filtering for all events which pass Level-1 will be implemented as a farm of high-speed (100 MHz or greater) RISC processors which would have access to all the event data. These processors may perform some or all of the following functions:

- Reduce the data volume and simplify offline analysis by suppressing zeros, clustering hits, and finding features in the data.
- Perform complete track reconstruction.
- Eliminate common sources of background. As an example, pileup may be removed by eliminating events with multiple primary vertices, or energy flow that is inconsistent with a single event.
- Repeat the Level-1 test with matched views, and correct weighting based on the track momenta.
- Determine the event topology.
- Look for specific B decay modes.

To determine the size of the RISC farm necessary to perform these functions we assume that the average event will require 10^6 RISC instructions. To handle the 50 kHz maximum Level-1 trigger rate, we estimate that we will need a "farm" with about 500 100-MIPS RISC processors. Clearly, should faster processors become available, this number can be reduced.

Note that the 10^6 instructions is an average figure, some events will take considerably more or less than this mean. Note also that some of the reconstruction tasks will have already been performed by the Level-1 processor (e.g. line finding in the silicon) and readout system.

References

[1] J.G. Zweizig, Nucl. Instrum. & Methods **A333** (1993) 223.

[2] W. Sippach et al., IEEE Trans. Nucl. Sci. **27** (1980) 578; E.P. Hartouni et al., IEEE Trans. Nucl. Sci. **36** (1989) 1480;

[3] S.A. Kleinfelder et al., IEEE Trans. Nucl. Sci. **35** (1989) 171.

9 Event Reconstruction & Tagging

In order to understand all efficiencies for event reconstruction and the backgrounds under B signals in mass spectra, we have written full event reconstruction software and run it on simulated spectrometer data. In this chapter we describe how we:

- **Simulate the Monte Carlo data samples,**
- **Write event reconstruction software,**
- **Simulate background in invariant mass spectra,**
- **Simulate flavor tagging,**
- **Estimate all efficiencies.**

9.1 Event Simulation

Pythia 6.3[1] is used as the event generator for all data samples. The primary interaction vertices are distributed with the expected LHC interaction region length ($\sigma_z = 5.3$ cm).

In the generation of events which contain the decay of a B-meson into an exclusive final state, JETSET 7.3[2] is used to decay all particles except the B-meson, which is "forced" to decay into a desired channel. B-meson oscillations are also included in the event generation with $x_d = 0.7$ and $x_s = 10$.

In the generation of events for the inclusive channels used in Sect. 9.3 for background studies, JETSET is used for all particle decays.

Tracks from the generated events are passed through COBEX detector simulation software and digitized events are written out as raw data tapes. The detector simulation includes all elements discussed in Chapts. 3, 4 and 5, with multiple scattering, gamma conversions and energy loss. Hadronic interactions are accounted for by stopping the track at its interaction point. Decays in flight of $\pi^{\pm}$'s and $K^{\pm}$'s are also included.

In tracking through the quadrupole and dipole fields, chamber points are generated smeared with the expected chamber resolutions. Realistic track parameters are then obtained by using the CERN minimization routine MINSQ to fit a charged particle trajectory through the quadrupole or dipole fields to the measured points. In each case, all available chamber points on a track are used in the fit. If a track is lost before a sufficient number of chamber points exist for a reliable fit, the track is thrown out and the geometric acceptance calculated accordingly. Only tracks with momentum greater than 200 MeV are used in the offline physics analysis. In general, a track's initial direction cosines are determined by requiring hits in at least two silicon detectors.

The studies of track finding efficiency in both the quadrupole spectrometer, discussed in Chapt. 3 and in the silicon system, discussed in Chapt. 4 show that both are very efficient. Therefore, in the Monte Carlo studies carried out thus far, perfect track pattern recognition has been assumed.

Mass identification of charged particles in the RICH counters has thus far been assumed to be perfect if a track's momentum is within the 3 σ limit discussed in Chapt. 5. In case of ambiguities, multiple mass identification assignments are made to reflect this fact. Electron and muon identification is supplemented by the electromagnetic calorimeter and muon systems, respectively, which are assumed to each be 90% efficient for tracks with momenta larger than 5 GeV. Misidentification of hadrons as leptons by these systems has not been implemented.

9.2 Event Reconstruction

The primary vertex of the event is found by minimizing a χ^2 using only x-y matched silicon tracks. The vertex χ^2 is formed from the impact parameters of all the tracks. If the χ^2 exceeds some cut value, the track making the largest χ^2 contribution is removed and the process is repeated. The iteration continues until either the χ^2 becomes acceptable or fewer than four tracks remain in the track list. If a primary vertex is found, the discarded tracks are subsequently used to search for additional vertices using the same procedure. If another primary vertex candidate is found inside the beam envelope which is either separated from the first by more than 5 cm, or has a high multiplicity, or a large invariant mass, the event is assumed to contain more than one interaction and is discarded. For large multiplicity decay modes, the primary vertex is recalculated after the tracks used in the reconstruction of the B-meson are removed from the track sample. This improves the decay-time resolution considerably.

We are studying the possibility of reconstructing exclusive B mesons decays in bunches which contain more than one interaction. Properly identifying the B mesons under such conditions could be possible for some decay modes (e.g. $B \rightarrow J/\psi K_s^\circ$) which have prominent signatures but is problematic for others such as the $B \rightarrow \pi^+\pi^-$ decays. Tagging with K mesons would also be of inferior quality.

Although the angular resolution of tracks which miss the silicon is not good enough to uniquely associate the tracks with either a primary or heavy flavor decay vertex, such tracks are nevertheless useful in the reconstruction of well-constrained high-multiplicity B decay modes and long-lived K^o_s's and Λ^o's.

Special reconstruction routines are written for each of the exclusive decay modes studied. Details of the reconstruction software and efficiencies are given for selected decay modes below.

The geometric acceptance is calculated with the following requirements:

- the momenta of the B_d decay tracks are successfully reconstructed by the momentum fitting routines and the momentum of each track is greater than 200 MeV,
- the primary vertex of the event is found when the B_d decay tracks have been removed from the vertex fit,
- for each decay mode, a subset of the decay tracks are measured in the silicon detector. The number of such tracks, and which ones should satisfy the requirement, is decay-mode-dependent and is described separately for each channel below.

The reconstruction efficiencies are calculated for events which are geometrically accepted in the apparatus and have passed the silicon topology trigger. The χ^2 cut used in the silicon topology trigger which is described in 8.1 is chosen to give 1/100 suppression for the Minimum Bias event sample.

9.2.1 $B_d \rightarrow J/\psi K^o_s$

In this section we describe the $B \rightarrow J/\psi K^o_s$ reconstruction software as an example of a CP-violation channel. Another example, the $B \rightarrow \pi^+\pi^-$ reconstruction procedure, is described by Erhan[3].

For events with a single primary vertex, J/ψ candidates are selected from uniquely identified opposite-sign lepton pairs which have a good vertex χ^2. To ensure good vertex resolution, the lepton tracks are required to have at least two hits in the silicon.

The K^o_s candidates are selected from $\pi^+\pi^-$ pairs which form a good vertex. All spectrometer tracks are used in order to maximize the K^o_s decay volume. The Cherenkov information for each track is required to be consistent with a pion identification.

The definition of geometric acceptance in this decay mode also requires that the lepton pairs are measured in the silicon detector and the K^o_s decay occurred within the decay volume. The downstream end of the K^o_s decay volume is bounded by the entrance to the quadrupole if one of its tracks is detected in Spectrometer I. Otherwise, the K^o_s decay volume is limited by the set of chambers in front of the dipole magnet in Spectrometer II. The geometric acceptance for the $B_d \rightarrow J/\psi K^o_s$ is 12% .

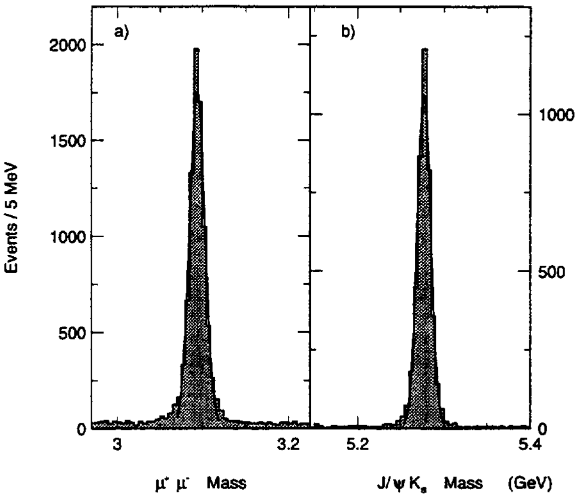

Figure 9.1: Reconstructed invariant mass spectrum (5-MeV bins) for J/ψ and $B \rightarrow J/\psi K^o_s$. The mass resolutions are σ_M = 9.2 and 7.7 MeV.

The topology trigger efficiency for this decay mode is 20% for events which are in the geometric acceptance of the apparatus.

The missing transverse momentum of the J/ψ and K^o_s is calculated with respect to the B-meson flight path and pairs with a small missing p_t normalized to its error are kept as a B candidates. The J/ψ and primary vertices are required to be separated by more than 0.5 mm. Finally, the invariant mass of surviving $J/\psi K^o_s$ pairs is formed and B mesons are selected with a mass cut of 50 MeV.

Figs. 9.1(a,b) show the resulting invariant mass distributions for the J/ψ and the $J/\psi K^o_s$ after reconstruction cuts. The measurement uncertainties are σ_M = 9.2 and 7.7 MeV for J/ψ and $J/\psi K^o_s$ respectively.

The reconstruction efficiency of $B_d \rightarrow J/\psi K^o_s$ for events which are within the acceptance of the apparatus and are triggered by the silicon topology trigger is 33% .

9.2.2 $B_s \rightarrow D_s^- \pi^+\pi^+\pi^-$

Here we describe the reconstruction of the $B_s \rightarrow D_s^- \pi^+\pi^+\pi^-$ final state as an example of a reconstruction of a large multiplicity decay mode. All $K^+K^-\pi$ combinations with a common vertex are formed and the combinations satisfying the D_s^- mass cut of 12 MeV are kept as D_s^- candidates. All three-pion combinations are formed using the tracks detected in the silicon detector. These are combined with the D_s^- candidates in order to search for B_s-mesons. When a B_s is found, its vertex is calculated using the three pions. Only two of the three D_s^- decay tracks are required to be in the silicon detector.

The event primary vertex is recalculated using only tracks measured in the silicon detector after removing the B_s decay tracks.

Kaon's used in the D_s^- search are required to be uniquely identified, pions to be π-compatible. A minimum decay length of 0.05 cm is required, along with a small transverse momentum measured relative to the B_s decay path.

The geometric acceptance calculation for this channel also requires that two of the D_s^- decay tracks and all of the π's from the B_s vertex are measured in the silicon detector. The geometric acceptance for the $B_s \rightarrow D_s^-\pi^+\pi^+\pi^-$ decay mode is 9%.

The topology trigger efficiency for this decay mode is 41% for events which are in the geometric acceptance of the apparatus.

Fig. 9.2(a) shows the $K^+K^-\pi^-$ invariant mass for all combinations (solid) and after D_s^--meson reconstruction cuts for events in which the B_s momentum points into a 600 mrad cone. The invariant mass of the $D_s^-\pi^+\pi^+\pi^-$ after all reconstruction cuts is shown in Fig. 9.2(b). The combinatoric background shown in the figure includes the contributions from the partially accepted B_s-mesons. The measurement error on $D_s^-\pi^+\pi^+\pi^-$ mass is $\sigma_M = 10.3$ MeV.

Fig. 9.3 shows the difference between the generated and reconstructed decay lengths of B_s-mesons for the $D_s^-\pi^+\pi^+\pi^-$ decay mode. The measurement error on the reconstructed decay length is $\sigma = 108$ μm. Fig. 9.4 shows the resulting error on the proper time measurement of the B_s-mesons as a function of B_s momentum (p). The solid line is a fit to the function $= \sqrt{(a/p)^2 + b^2}$ where p is the reconstructed B_s momentum. The proper time resolution decreases as 1/p and becomes constant for B_s momentum greater than 40 GeV. The error in proper time measurement is $\sigma(t)/\tau < 3\%$ for B_s momenta above 50 GeV. The reconstruction efficiency of the $B_s \rightarrow D_s^-\pi^+\pi^+\pi^-$ decay mode for events accepted in the apparatus and triggered by the silicon topology trigger is found to be 62% for a mass cut of 30 MeV.

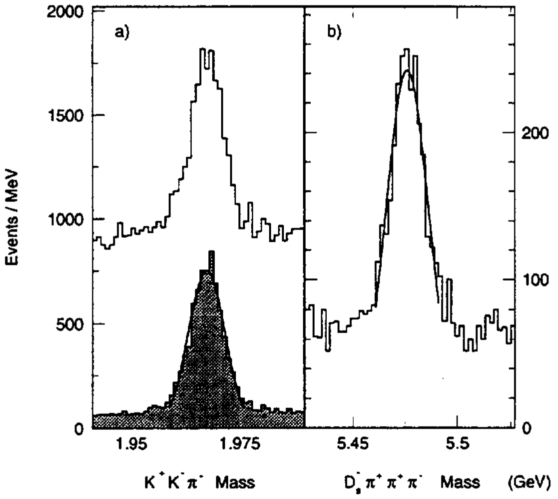

Figure 9.2: (a) The invariant mass spectrum for all $K^+K^-\pi^-$ combinations (solid) and after the D_s^--meson reconstruction cuts (shaded) for events in which the B_s momentum points into a 600 mrad cone. (b) Reconstructed invariant mass spectrum for $B_s \rightarrow D_s^-\pi^+\pi^+\pi^-$ for the same events. The combinatoric background shown includes contributions from partially accepted events.

9.2.3 $B_d \rightarrow \mu^+\mu^-K^*$

The event reconstruction for the $B_d \rightarrow J/\psi K_s^\circ$ decay mode is carried out with a four-fold loop over all reconstructed tracks using all combinations of μ^+, μ^-, K^+ and π^- tracks with a common vertex. The muon pair is required to be uniquely identified while only π-incompatibility is required for the kaon. The pion is allowed to be ambiguous. In addition, at least three of the four tracks are required to be measured in the silicon detector.

The primary vertex of the event is refitted using all the silicon tracks which are not used in the B_d reconstruction. If the primary vertex cannot be found after removal of the B_d tracks then the candidate is discarded.

The geometric acceptance for this decay mode includes the requirement that the number of B_d decay tracks detected in the silicon detector is greater than two. With this requirement, in addition to the general acceptance criteria given above, the geometric acceptance for this decay mode is 17% and the silicon topology trigger efficiency for the accepted B_d-

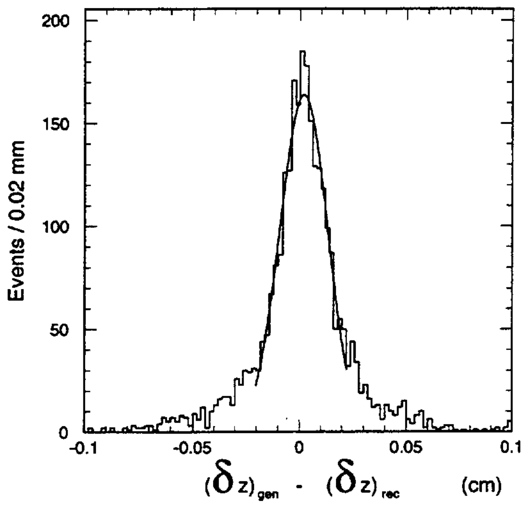

Figure 9.3: Difference between generated and reconstructed decay lengths for $B_s \rightarrow D_s^- \pi^+ \pi^+ \pi^-$ mesons. The error on the reconstructed decay length is $\sigma = 108\ \mu$m.

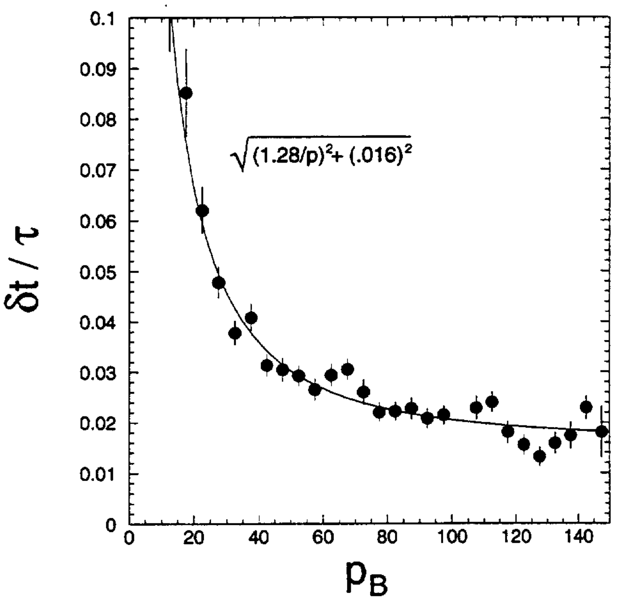

Figure 9.4: The measurement error in proper time, $\sigma(t)/\tau$, as a function of momentum (p) for reconstructed B_s-mesons. The solid curve is a fit to the function $\sqrt{(a/p)^2 + b^2}$, where p is the reconstructed B_s momentum.

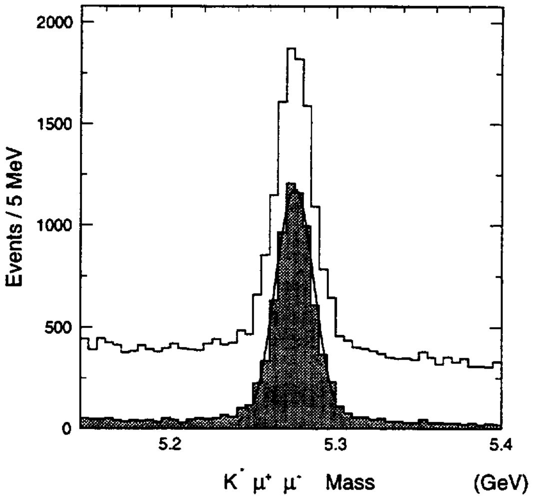

Figure 9.5: The invariant mass spectrum (5-MeV bins) of $\mu\mu K\pi$ for all combinations (histogram) and after reconstruction cuts (shaded histogram). The mass resolution is $\sigma = 11.7$ MeV.

mesons is 24% .

The B_d reconstruction requires that the four track vertex is separated from the refit primary vertex by more than 0.05 cm and that the total transverse momentum of the four tracks with respect to the B_d decay path is small compared to its error. A $K\pi$ submass and a $\mu\mu K\pi$ mass are calculated for candidates which pass the reconstruction cuts and the calculated masses are required to be within mass cuts of 100 MeV and 50 MeV, centered on the $K^*(890)$ and B_d masses, respectively.

Fig. 9.5 shows the resulting invariant mass distributions of all $\mu\mu K\pi$ combinations from events where the momentum vector of the B_d points into a 600 mrad cone. The shaded histogram shows the same distribution after reconstruction cuts. The combinatoric background seen in the figure is mostly from partially accepted events. The measurement uncertainty for the $\mu\mu K\pi$ mass is $\sigma = 11.7$ MeV.

The reconstruction efficiency calculated using events which are accepted in the apparatus as described above and passing the silicon topology trigger is 35% .

9.3 Background Simulation

In order to study the background contributions from various sources, we have prepared four event samples: minimum bias, inclusive $b\bar{b}$ inclusive $c\bar{c}$ and two-event superposition.

The minimum bias and inclusive event samples are subjected to the same reconstruction and tagging analysis as the signal channels in order to obtain the background produced by these sources.

Inclusive $b\bar{b}$ and $c\bar{c}$ events could contribute a major part of the background since these events already contain a secondary vertex and for some decay modes such as $B_d \rightarrow J/\psi K_s^o$ some of the submasses are produced with larger branching ratios. Pile-up events could be a source of background for decay modes which do not contain submasses i.e. $B_d \rightarrow \pi^+\pi^-$ if two event vertices are sufficiently close.

For the $J/\psi K_s^o$ mode, the background from all sources has been estimated to be less than 10%. This is determined by passing small samples of events from all classes: minimum bias, inclusive charm and inclusive beauty, through the reconstruction software for the $J/\psi K_s^o$ mode, and weighting them by their cross sections and estimated trigger efficiencies. Considerably more background may be present in the $B \rightarrow \pi^+\pi^-$ final state, as discussed in Ref. [3], but the analysis is not yet complete.

Presently, we are re-doing the background analysis with much larger event samples and extending the study to other decay modes.

9.4 Tagging

To avoid the large event loss which would arise from requiring full reconstruction of both B and $\bar{B}$ in the spectrometer, a single particle from the second B can be used as a tag, providing certain conditions are met. As discussed in the following paragraphs, either leptons or charged kaons can provide useful tags. In order to understand the tagging possibilities, an analysis was made of PYTHIA-generated $B\bar{B}$ events.

The type of trigger used (lepton or silicon topology - see Sect. 8) influences every step that follows: the reconstruction efficiency, the tagging efficiency and the dilution effect. All these factors are combined in the estimates of CP-Reach in Sect. 10.2. In this section, we only give lepton and kaon tagging efficiences for events which pass a silicon topology trigger. An advantage of this trigger is that it does not bias the tag particle. Dilution effects are discussed in Sect. 10.1.

9.4.1 Lepton tagging

For reconstructed B-decays in a 600 mrad spectrometer, most muons from the pair-produced $B\bar{B}$ are in the same spectrometer hemisphere and are correlated within one unit of rapidity. At the LHC, about 6% of reconstructed events have a tagging muon with $p_t > 1.2$ GeV (necessary to suppress muons from the c → s transition) in the spectrometer. The tag quality (good tags/all tags) is found to be about 74%. The momenta of most muons outside the 600 mrad aperture is low, so little is to be gained from extending the muon identification beyond 600 mrad.

A similar fraction of reconstructed events will be tagged by an electron with $p_t > 1.2$ GeV.

9.4.2 $K^\pm$ tagging

The strategy is to examine identified $K^\pm$ mesons that are not associated with the reconstructed B and are inconsistent with coming from the primary vertex.

A $K^\pm$ which contains the s-quark at the end of the b → c → s chain uniquely identifies the flavor of its $\bar{B}$-Meson at decay. However, there are many sources of mis-tagging, such as kaons which are produced from the $s\bar{s}$ sea or from a $W^\pm$ in either the b → c or c → s transitions (which can have either sign). These are all approximately accounted for in the PYTHIA event generation and can be investigated by tabulating the supplementary kaons found in the spectrometer. About 27% of the B-mesons in the spectrometer are found to have a tagging $K^\pm$ with impact parameter greater than 3σ from the primary vertex. The correct charge is found in about 80% of these tags. Thus, for the silicon topology trigger, kaons and leptons can together tag as much as 36% of all reconstructed B-Mesons.

The geometric acceptances, silicon topology trigger efficiencies and reconstruction efficiencies for three decay modes are summarized in Table 9.1. The geometric acceptance given in the table includes all the fiducial cuts explained in the reconstruction section earlier. Silicon trigger efficiencies are for fully accepted events. The reconstruction efficencies are calculated for accepted and triggered events. The total efficiencies for these decay modes, defined as the product of geometric acceptance, trigger and reconstruction efficiencies, are given in the bottom row.

References

[1] H.U. Bengtsson and T. Sjöstrand, Computer Physics Comm., 46 (1986) 43.

	$B_d \to J/\psi K_s^o$	$B_s \to D_s^- \pi^+\pi^+\pi^-$	$B_d \to \mu^+\mu^- K^*$
Geometric Acceptance	0.12	0.09	0.17
Trigger Efficiency	0.20	0.41	0.24
Reconstruction	0.33	0.62	0.35
Total Efficiency	0.008	0.023	0.014

Table 9.1: Geometric acceptance is calculated for $B_d \to J/\psi K_s^o$, $B_s \to D_s^- \pi^+\pi^+\pi^-$ and $B_d \to \mu^+\mu^- K^*$ decay modes as explained in the text. Trigger efficiencies given are for silicon topology trigger and are for accepted events. Reconstruction efficiencies are for accepted and triggered events. Total efficiencies for these decay modes are the products of geometric acceptance, trigger and reconstruction efficiencies.

[2] T. Sjöstrand, Computer Physics Commun. **39** (1986) 347. T. Sjöstrand and M. Bengtsson, Computer Physics Commun. **43** (1987) 367.

[3] S. Erhan, Nucl. Instrum. & Methods **A333** (1993) 213.

10 Physics Analyses and Performance

In this chapter, we discuss the details of the physics analyses, and summarise the expected performance of the experiment in the following highest priority measurements:

- B_s-$\overline{B_s}$ Mixing
- CP Violation
- Rare B-Meson Decays

10.1 Mixing Analysis and Measurement of Dilution Factors

We consider a prototype mixing measurement in which relatively large branching ratio exclusive final states of the B_d or B_s are reconstructed and the proper decay time of each event is measured. The flavor of each B-meson at production is tagged by observing a supplementary $K^{\pm}$ or $\ell^{\pm}$ in the spectrometer, as discussed in Sect. 9.4.

For a given mixing channel, there are two CP-conjugate initial states and two CP-conjugate final states, resulting in four independently observable samples. Their time-dependent decay rates, were given in Eqs. 3 and 4. The functions given are idealised, and would be measured only in the case of perfect tagging. In practice, imperfect tagging causes a dilution of the effect, as events which belong in one sample are placed in another. What is observed in each sample is therefore a linear combination of the correct distribution with that of the CP-conjugate initial state.

The net effect of mis-tagging is therefore to modify the decay-time distributions to the following forms, where the tagging particles (leptons and charged kaons) are denoted $T^{\pm}$, depending on their charge. Note that in general, $B \rightarrow T^{+}$ and $\bar{B} \rightarrow T^{-}$, so that eg. T^{+} means that the mixing particle was a $\overline{B}$.

$$T^{+}B: \quad A(t)e^{-t}[1 - D^{+}\cos(xt)] \qquad (24)$$

$$T^{-}B: \quad A(t)e^{-t}[1 + D^{-}\cos(xt)] \qquad (25)$$

$$T^{+}\bar{B}: \quad A(t)e^{-t}[1 + \bar{D}^{+}\cos(xt)] \qquad (26)$$

$$T^{-}\bar{B}: \quad A(t)e^{-t}[1 - \bar{D}^{-}\cos(xt)] \qquad (27)$$

where the $\overset{(-)}{D}{}^{\pm}$ are the dilution factors. Time, t, has been expressed in units of proper time. The factor A(t), is the COBEX experimental "acceptance function", which reflects various biases in the B lifetime measurements. Such biases result, for example, from cuts on B flight path during offline event reconstruction or even at the trigger level if the silicon topology trigger is used. COBEX Monte Carlo studies yield the approximate form, $A(t) = 4t^2/(1+4t^2)$, for reconstructed B events. The most significant distortion of the measured proper time distribution occurs for times less than about one mean life.

The dilution factors contain, among other things, the time-integrated probabilities for non-oscillation and oscillation of the tag-providing B. Although the four dilution factors should be quite similar, tag background, B_s background and a B-$\bar{B}$ production asymmetry (or other valence quark effects) can make these factors differ from one another. A careful study of tagging efficiencies and production asymmetries using both the oscillation measurements described here and the tagging of non-oscillating $B^{\pm}$ decays is necessary in order to obtain reliable measurements of the dilution factors.

The determination of x_s is an important step in the physics program outlined in Chapter 2. For now, we assume that there is no pathological behavior of the dilution factors in Eqs. 24-27 and we proceed to understand how large a value of x_s can be measured with the B_s data sample that will be obtained in the first year of running COBEX at LHC. We take as an example, the channel

$$B_s \rightarrow D_s^{\pm}\pi^{\mp}\pi^{+}\pi^{-}. \qquad (28)$$

The parameters relevant to the estimation of the yield of such events are shown in Table 10.1. The sample of more than 10^5 reconstructed tagged B_s events that will be obtained in the first year of LHC running is an enormous one for a determination of x_s. As shown in Chapter 9, the proper time resolution in B_s decay, for B_s's with momentum in the range 50-100 GeV, is $\sigma(t)/\tau = 3\%$. Figs. 10.1 show a Monte Carlo data sample plotted versus proper time for the two types of

Luminosity	$5 \cdot 10^{31}$ cm^{-2}s^{-1}
Running time	10^7 s
$b\bar{b}$ cross section	$5 \cdot 10^{-28}$ cm^2
Hadronisation to B_s or $\overline{B}_s$	0.24
BR($B_s \rightarrow D_s^{\pm}\pi^{\mp}\pi^{+}\pi^{-}$)[1]	$6.6 \cdot 10^{-3}$
BR($D_s^{\pm} \rightarrow$ all charged)	$6.0 \cdot 10^{-2}$
Total Efficiency	$8.3 \cdot 10^{-3}$
No. tagged and reconstructed	$2.0 \cdot 10^5$

Table 10.1: Event yield of tagged and reconstructed events at COBEX in the first year of LHC for $B_s \rightarrow D_s^{\pm}\pi^{\mp}\pi^{+}\pi^{-}$. The total efficiency includes geometrical, trigger, reconstruction and tagging efficiencies.

distribution in Eqs. 24-27. 50,000 tagged events were generated according to the functions with the dilution factor assumed to have a value $D = 0.40$ and $x_s = 25$. The curves in the figures are the result of maximum likelihood fits of the equations to the data. Figs. 10.2 show the log of the likelihood function plotted versus x_s, for four widely different values of x_s. There is a clear single minimum seen for the largest theoretically allowed value of x_s.

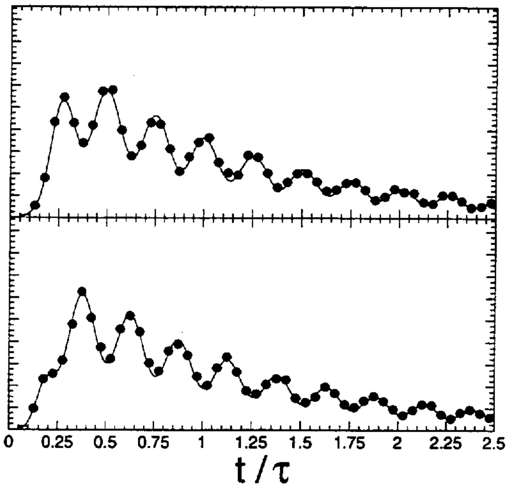

Figure 10.1: Proper time distributions for the two types of tagged events, generated according to Eqs. 24-27 using a uniform $D = 0.40$. The two plots correspond to $x_s = 25$, with the upper plot using $1 + D\cos(xt)$, and the lower plot using $1 - D\cos(xt)$. There is a generated sample of 50,000 tagged events. The curves result from simultaneous Maximum-Likelihood fits to the data shown and to the proper time distribution of the corresponding untagged sample. The generated events include the effects of the 3% uncertainty in proper time measurements as discussed in the text.

Finally, we summarize the statistical significance for the range of x_s values used in the fits just described. Fig. 10.3 shows the statistical significance of the oscillation (the fitted value of D divided by its uncertainty) versus x_s and also, on the same plot, the fitted uncertainty in x_s versus the value of x_s.

There is great value in demonstrating good sensitivity to large values of x_s. For the CP violation analysis discussed in the next section, asymmetries will have to be measured in rapidly varying time distributions and the better the overall capability, the more reliable will be the results.

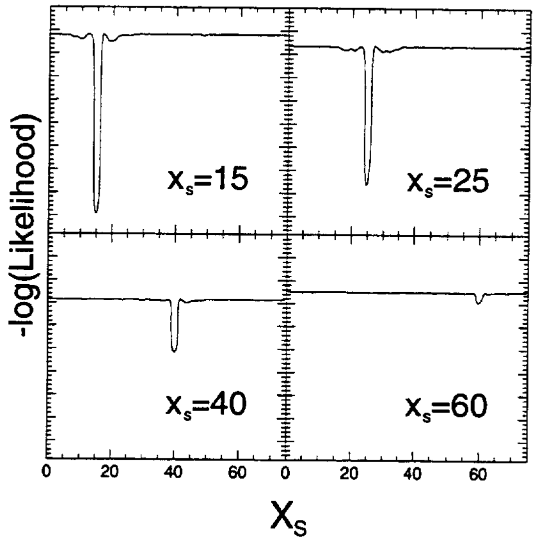

Figure 10.2: Log of the likelihood function versus x_s, for the four indicated values of x_s, for a data sample of 50,000 tagged events and for a 3% uncertainty in proper time measurements.

10.2 Analysis of CP-Violation

The various observables discussed in section 2.2 will be addressed in turn.

Decays of Neutral B-mesons to CP-eigenstates.

The time-dependence of such decays was given in Eq. 11. Decays of B_d and $\bar{B}_d$ to $J/\psi K^o_s$ involve a unique CKM phase, so that the time-dependent rates reduce to

$$\Gamma(t)(\overset{(-)}{B}{}^0 \to J/\psi K^0_S) = Ae^{-t}[1 \mp \sin(2\beta)\sin(xt)]. \quad (29)$$

In practice, as in the case of B_s-$\overline{B_s}$ mixing, imperfect tagging results in a dilution of the samples with events from the other sample, and the observed time dependences are linear superpositions of the two, as follows:

$$\bar{\mathrm{N}}(t)(\bar{B}_d \to J/\psi K^o_s) \propto A(t)e^{-t}[1 + D^+\sin(2\beta)\sin(xt)] \quad (30)$$

$$\mathrm{N}(t)(B_d \to J/\psi K^o_s) \propto A(t)e^{-t}[1 - D^-\sin(2\beta)\sin(xt)] \quad (31)$$

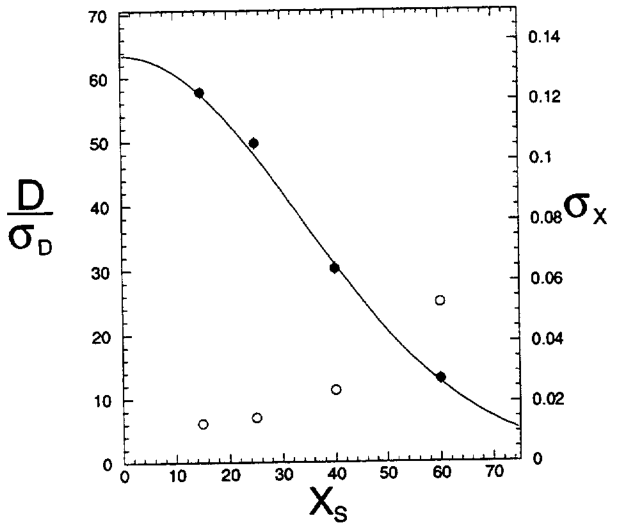

Figure 10.3: Black dots: The statistical significance of the fitted value of the dilution factor, D (D, divided by its uncertainty) versus x_s used in the event geneneration. Open dots: The fitted uncertainty of x_s (use the right hand scale) versus x_s.

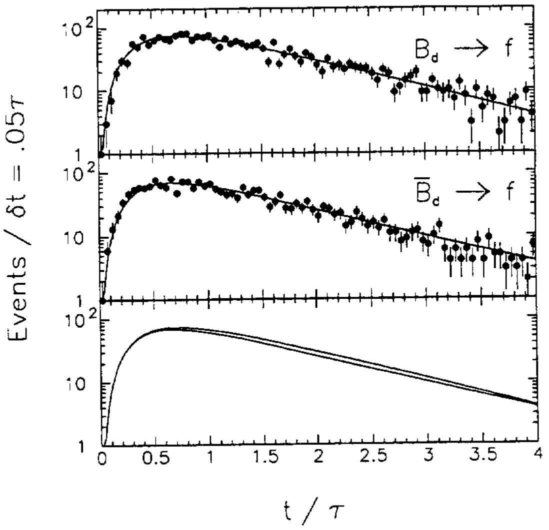

Figure 10.4: Monte-Carlo study of CP-Violation effects in B_d decay. (a) Proper time distribution of 2100 events generated according to Eq. 31 assuming $\sin(2\beta) = 0.20$, $x = 0.7$ and $D\pm = 0.40$. The curve is the fitted function used in the generation; (b) same for Eq. 30; (c) the two curves from (a,b) are superimposed. All curves contain the acceptance function, A(t), discussed in the text.

where again, the experimental acceptance function has been included and the dilution factors, D^+ and D^-. The latter may be obtained experimentally by measuring the amplitudes of B_d oscillations to large branching ratio non-CP-eigenstates, in analogy to the measurement of B_s oscillations discussed in the last section.

A CP-measurement consists of simultaneously (or independently) fitting Eqs. 30 and 31 to the observed proper time distributions of mesons flavor-tagged as $\bar{B}_d$ and B_d, respectively, to obtain the product of a dilution factor and the CP-violation parameter $\sin(2\beta)$. It is evident that the independent determination of the dilution factors is critical.

To determine the measurement uncertainty of $\sin(2\beta)$ and how the uncertainty depends on the sample size and $D^{\pm}$, Monte Carlo event samples were generated according to Eqs. 30 and 31, assuming various values of $\sin(2\beta)$ and $D^{\pm}$. Except for the (small) background under the mass peak, all sources of wrong tags are modeled, including those resulting from oscillation. Simultaneous Maximum Likelihood fits of Eqs. 30 and 31 were then made to the observed time distributions. Fig. 10.4 shows one example of such a fit. 4200 $\bar{B}_d$ plus B_d events were generated assuming $\sin(2\beta) = 0.20$, $x = 0.7$ and $D = 0.40$. The resulting fit yielded $\sin(2\beta) = 0.176 \pm 0.044$ (4σ). It is interesting to note in Fig. 10.4, that the loss of events with t less than about one mean life has no great influence on the measurement of $\sin(2\beta)$, since Eqs. 30 and 31 have their maximum difference when $\sin(xt) = 1$, corresponding to $t = 2.2$ mean lives for $x = 0.7$.

The resulting uncertainty in $\sin(2\beta)$ is found to depend on sample size, N (B plus $\bar{B}$ events) in the following way:

$$\delta[\sin(2\beta)] = \frac{1}{\sqrt{0.56 D^2 \mathrm{N}}} \tag{32}$$

where the constant 0.56 is a statistical factor which is characteristic of the time-dependent fit and our particular acceptance function. For COBEX, $0.56D^2$ is in the range 0.09 to 0.11.

In order to calculate the number of events produced per year, and the CP-reach, we note that the number of $\overset{(-)}{B}_d$ produced per year ($= \mathcal{L} \times t \times \sigma_{b\bar{b}} \times$ BR($b \rightarrow B_d$) $\times$ 2) is $\simeq 2 \cdot 10^{11}$ at the low luminosity of $5 \cdot 10^{31}\mathrm{cm}^{-2}\mathrm{s}^{-1}$. The other relevant quantities for the calculation are shown in Table 10.2. As shown above, it is estimated that in the channel $B \rightarrow J/\psi K^\circ_s$ alone,

No. of $\overset{(-)}{B}_d$ yr^{-1}	$2 \cdot 10^{11}$
BR($B^0 \rightarrow J/\psi K_S^0$)[2]	$5.6 \cdot 10^{-4}$
BR($J/\psi \rightarrow \mu^+\mu^-$)	$6.0 \cdot 10^{-2}$
BR($K_S^0 \rightarrow \pi^+\pi^-$)	$6.86 \cdot 10^{-1}$
Overall Efficiency (ϵ_{total})	$8 \cdot 10^{-3}$
Tagging Efficiency (ϵ_{tag})	$3.6 \cdot 10^{-1}$
No. of events per year	$\simeq 13000$
(Dilution Factor)^2	$1.8 \cdot 10^{-1}$
Fitting Factor	$5.6 \cdot 10^{-1}$
$\Delta[\sin 2\beta]$	0.027

Table 10.2: Event yield and CP-reach of tagged and reconstructed events at COBEX in the first year of LHC running for the channel $B \rightarrow J/\psi K_s^o$. The total efficiency ϵ_{total} includes geometrical, trigger and reconstruction efficiencies.

the statistical error on the determination of $\sin 2\beta$ will be of the order of 0.03 in one year of running. Close inspection of Fig. 2.1 reveals that $|\sin 2\beta| > 0.2$, so that even at the lower limit, it will be well measured within the first year.

The CP-reach of COBEX for $\sin 2\alpha$ was reviewed by Erhan[3]. This channel is very difficult to simulate, owing to the large combinatorial background, and furthermore, the effects of "penguin pollution" cause considerable uncertainty in the interpretation of the results. An updated analysis is in preparation, results of which will be presented to the LHCC.

Decays of Neutral B-mesons to non-CP-eigenstates.

This method is one of the particularly strong advantages of the LHC environment for B physics: B_s mesons are required, which are not accessible at an e^+e^- B-factory. The method can be applied to measure γ at COBEX, using any of the channels:

- $B_s^0 \rightarrow D_s^\pm K^\mp$,
- $B_s^0 \rightarrow D_s^{*\pm} K^\mp$
- $B_s^0 \rightarrow D_s^\pm K^{*\mp}$

which are expected to have the time dependences given in equations 15 and 16. It can also be applied to other final states with the same flavour quantum numbers, but in these cases, the angular distributions need to be analysed for the helicity amplitudes.

In the above channels, the analysis will proceed along similar lines to that of B_s-$\overline{B_s}$ mixing, except for the additional complication that the B_s decay vertex must be measured from the line of flight of the reconstructed D_s and the track of the charged kaon. Two possible methods are foreseen. In the first, a straight line is projected from the primary to the fully reconstructed D_s decay point. Then the intersection of this line with the charged kaon track is found and is taken as the B_s decay point. The second method consists of reconstructing the flight path of the D_s from its vertex position and its momentum, vector, and finding the intersection of this with the charged kaon track. These two methods have different errors. In the second case, a preliminary study has shown that the error on the z-coordinate of the B_s vertex is not significantly degraded compared with that where the tracks actually come from the vertex, so that the vertex resolution found in the B_s mixing study may be used here.

In order to calculate the number of events produced per year, we note that the number of B_s produced per year ($= \mathcal{L} \times t \times \sigma_{b\bar{b}} \times$ BR(b $\rightarrow B_s$) $\times$ 2) is $\simeq 6 \cdot 10^{10}$ at the low luminosity. In order to estimate the acceptance and efficiencies in these channels, we rely on the results of the B_s mixing study (Sect. 10.1). Here, the only difference is in the particles accompanying the D_s in the final state: a kaon, a $K - \pi$ pair, or possibly a $\pi - K^0$ pair as compared with three pions. There are competing factors, namely the geometric acceptance, which should be larger for low multiplicity final states, the trigger efficiency which, at least for the topology trigger, will be less for lower multiplicity, and the reconstruction efficiency which should also be somewhat better with less combinatoric background to remove. We conservatively estimate the product of these and the tagging efficiency (independent of final state) as $5 \cdot 10^{-3}$ for the D_s case and $3 \cdot 10^{-3}$ for the D_s^*.

The relevant branching ratios [4] to the final states and the number of events per year in each channel are shown in Table 10.3. Each channel includes a 6% branching ratio for the D_s to go to all charged particles. It should be noted that the branching ratios and event yields for the latter three states are only order-of-magnitude estimates. In order to extract the angle γ from the data, the following asymmetry may be formed (from equations 15 and 16):

$$\begin{aligned} A_{\overset{(-)}{f}}(t) &= \frac{\Gamma(t)(B^0 \rightarrow \overset{(-)}{f}\ ) - \Gamma(t)(\bar{B}^0 \rightarrow \overset{(-)}{f}\ )}{\Gamma(t)(B^0 \rightarrow \overset{(-)}{f}\ ) + \Gamma(t)(\bar{B}^0 \rightarrow \overset{(-)}{f}\ )} \\ &= \pm B \cos(xt) \\ &- C \sin(\phi_f \pm \delta_s) \sin(xt)] \end{aligned} \qquad (33)$$

where $B = (1-|\lambda|^2)/(1+|\lambda|^2)$, $C = 2|\lambda|/(1+|\lambda|^2) = 1 - B^2$ and λ is defined in eq. 10. As in the case of B_s-$\overline{B_s}$ mixing, dilution factors are also present, which, for clarity, have been suppressed in the above equations. They should take the same values in this analysis however. Fitting the two asymmetries above,

B_s Decay Mode	- B. R. $\cdot 10^{-4}$	ϵ_{total} $\cdot 10^{-3}$	No. yr^{-1} $\cdot 10^{3}$
$D_s^- K^+$	(2.4 ± 0.5)	5	4.3
$D_s^{*-} K^+$	(2.4 ± 0.5)	3	2.6
$D_s^- K^{*+}$	(4.4 ± 1.6)	3	5.2
$D_s^+ K^-$	~ 1.4	5	2.5
$D_s^{*+} K^-$	~ 1.4	3	1.5
$D_s^+ K^{*-}$	~ 0.9	3	1.1

Table 10.3: Event yield of tagged and reconstructed events at COBEX in the first year of LHC running for the Non-CP final eigenstates shown. ϵ_{total} is the product of geometrical, trigger, reconstruction and tagging efficiencies. In the K^* case, ϵ_{total} contains an extra factor of 0.67 for the BR($K^* \rightarrow$*charged*).

$|\lambda|$, $\sin(\phi_f + \delta_s)$ and $\sin(\phi_f - \delta_s)$ may be extracted. It can be shown [5] that the errors on the coefficients ($c_i = B, C\sin(\phi_f \pm \delta_s)$) of the trigonometric functions in the above asymmetries are given by

$$\Delta c_i = \frac{1}{\sqrt{F_i(t_0) N_{tot}}} \tag{34}$$

where t_0 is the minimum proper time at which events are observed and N_{tot} is the total number of events used to calculate the asymmetry. The "fitting factors" $F_i(t_0)$ are a measure of the average statistical weight per event used to calculate the asymmetry: as the asymmetry varies between ± 1, some events (those where the asymmetry is small) make a comparitively small contribution to our knowledge of the amplitude. In the case of B_s mixing, these factors are approximately 0.5 for both coefficients. This is simply because for $x > 5$, the asymmetry oscillates many times before the amplitude of the decay distributions falls off significantly, so that the mean value of $|\sin(xt)|$ is 0.5, thereby diluting the weight of each event accordingly.

We are now in a position to calculate the statistical error on $\sin(\phi_f \pm \delta_s)$. In ref. [4], it is argued that in the channels discussed here, $\delta_s \simeq 0$, so that we measure $\sin(\phi_f)$ directly. In this case,

$$\Delta \sin(\phi_f) = \frac{1}{DC\sqrt{F_i(t_0) N_{tot}}} \tag{35}$$

where D is the dilution factor. We assume the same value for the dilution factor as in the B_s mixing analysis, ie. $D \simeq 0.4$. C is unknown, but an estimate to better than an order of magnitude may be obtained from Table 10.3, using the fact that

$$\lambda = \frac{\sqrt{BR(B_s \rightarrow f)}}{\sqrt{BR(\overline{B}_s \rightarrow f)}} = \frac{\sqrt{BR(B_s \rightarrow f)}}{\sqrt{BR(B_s \rightarrow \overline{f})}}. \tag{36}$$

For example, for the first decay in Table 10.3, $|\lambda| = 0.76$, giving $C \simeq 0.96$, close to its upper limit of 1. A safe lower bound for C in this case is around 0.15. We therefore quote the CP-reach in a given channel using the constant k, where and the range of C, where $\Delta \sin(\phi_f) = k/C$. The CP-reach for the various channels is listed in table 10.4 from which it can be seen that using several channels, the error on $\sin(\gamma)$ will be less than 0.07 in one year's running at LHC.

B_s Decay Mode	Range of C	k	Max. error on $\sin(\gamma)$
$D_s^- K^+$	0.45 - 1	0.043	0.10
$D_s^{*-} K^+$	0.45 - 1	0.055	0.12
$D_s^- K^{*+}$	0.28 - 1	0.040	0.14

Table 10.4: CP-reach for $\sin\gamma$ for the first year of LHC running. The error on $\sin\gamma$ is given by k/C.

10.3 Analysis of Rare Decay Modes

Following the discussion in Chapt. 2, we would like to consider some of the decay modes discussed there.

We believe that the inclusive decays

$$B_s^0 \rightarrow X_s e^+ e^- B_s^0 \rightarrow X_s \mu^+ \mu^- \tag{37}$$

will be observble at COBEX. In the absence of new physics beyond the Standard Model, their branching ratios are expected to be [6] $(0.6 - 2.5) \cdot 10^{-5}$ and $(3.5 - 14.0) \cdot 10^{-6}$ respectively. The signature will be the existence of two leptons originating from a single secondary vertex, with, in addition, at least two other charged hadronic tracks from the same vertex, one of which is a kaon. These are currently the subject of a study, results of which will be presented to the LHCC in due course.

Several exclusive rare decay modes are also of interest at COBEX. These are shown in Table 10.5 along with their predicted Standard Model branching ratios [6]. We have simulated as an example, the channel $B_d^0 \rightarrow \mu^+ \mu^- K^*$ as described in Chapter 9. The total efficiency, as defined there is found to be 1.4%, which, after allowing for the Clebsch-Gordan coefficient for K^{*0} to decay to charged particles gives an expected number of about 5000 reconstructed events for the first year of running with the average peak luminosity of $5 \cdot 10^{31}$ $\mathrm{cm}^{-2}\mathrm{s}^{-1}$. This will allow detailed kinematic distributions to be formed, providing a rigorous test of the Standard Model in this very rare process. The efficiencies for the other channels are expected to be of the same order of magnitude.

In the case of the purely leptonic rare decay

$$B_s^0 \rightarrow \mu^+ \mu^-, \tag{38}$$

B_d Decay Mode	B. R.	No. produced in 10^7 s
$B_d^0 \to e^+e^-K^*$	$\simeq 5.6 \cdot 10^{-6}$	$\simeq 1.1 \cdot 10^6$
$B_d^0 \to \mu^+\mu^-K^*$	$\simeq 2.9 \cdot 10^{-6}$	$\simeq 5.8 \cdot 10^5$
$B_d^0 \to e^+e^-K$	$\simeq 6.0 \cdot 10^{-7}$	$\simeq 1.2 \cdot 10^5$
$B_d^0 \to \mu^+\mu^-K$	$\simeq 6.0 \cdot 10^{-7}$	$\simeq 1.2 \cdot 10^5$
$B_d^0 \to e^+e^-\omega^\circ$	$\simeq 3.7 \cdot 10^{-7}$	$\simeq 7.4 \cdot 10^4$
$B_d^0 \to \mu^+\mu^-\omega^\circ$	$\simeq 1.9 \cdot 10^{-7}$	$\simeq 3.8 \cdot 10^4$

Table 10.5: Branching ratios and event yield during first year of LHC running for rare decays observable at COBEX using the topology trigger.

its branching ratio is expected to be $1.8 \cdot 10^{-9}$ in the absence of new physics beyond the Standard Model. In order to detect this channel, it will be necessary to run in the high luminosity mode at $5 \cdot 10^{33}$ cm^{-2}s^{-1}. At this luminosity, there will be an average of 9 intereactions per beam crossing. Preliminary studies show that using kinematic cuts alone, only a branching ratio of about 10^{-6} is reachable, before being swamped by the main background - that due to semi-leptonic decays of more than one B-meson in the same beam crossing. In order to achieve something approaching the Standard Model branching ratio, it is necesary to use vertex information to ensure that both muons come from a single vertex. In order that the silicon should survive such a high luminosity however, the silicon is retracted from 3 mm from the beam to 1 cm from the beam. As the particle density varies as $1/r_\perp^2$(see Sect. 3.2), this maintains the flux in the silicon at essentially the same levels as at medium luminosity, $5 \cdot 10^{32}$ cm^{-2}s^{-1}. This reduces the geometrical acceptance somewhat, but with a two-body decay, it is still significant.

References

[1] S. Stone, private communication.

[2] S. Stone, HEPSY 93-4, to appear in proceedings of 5th International Symposium on Heavy Flavour Physics, Montreal, 1993.

[3] S. Erhan, Nucl. Instrum. & Methods **A333** (1993) 213.

[4] R. Aleksan, I. Dunietz & B. Kayser, Zeit. Fur Phys. C 54, 653 (1992).

[5] P.F. Harrison, Nucl. Inst. and Meth. A333 (1993), 230.

[6] A. Ali, private communication (1993).

11 Experimental Area & Installation

11.1 Insertion Requirements

Since COBEX plans to use colliding beam interactions it can make use of a normal insertion layout. Compensation of the effects of the magnetic fields of the spectrometer on the circulating LHC beams will have to be studied but are not expected to cause any special problems.

The experiment also requires vertex detectors placed within a few mm of the beams at the center of the collision region, above and below the beams. These detectors will therefore be placed in moving vacuum enclosures of the type often referred to as "Roman Pots". The present suggestion is to use vacuum vessels and detectors similar to those already used at the SPS collider in P238 and studied in RD21.

There will be three different modes of operation, depending on the available luminosity. COBEX plans to start with a luminosity of $5 \cdot 10^{31}$ cm^{-2}s^{-1} for the first year or two. Since this can be obtained with an LHC luminosity as high as $1.5 \cdot 10^{33}$, it can be foreseen that there will be no difficulty for the desired period. After this initial running period, COBEX will switch to its single muon trigger and run with a luminosity of $5 \cdot 10^{32}$ cm^{-2}s^{-1}, which can be obtained with LHC luminosity as high as 1.5×10^{34}.

When LHC reaches its peak luminosity of $2.5 \cdot 10^{34}$, a third running mode with $5 \cdot 10^{33}$ cm^{-2}s^{-1} will be used and the silicon system will be retracted to about 1 cm from the beam.

Thus, we foresee being able to operate at all times with the standard beta of 0.5 to 15 m. The standard quadrupole separations will be sufficient and in principle no protection of these quadrupoles will be needed for at least the first two years of LHC operation.

11.2 Underground Cavern

An experiment of the COBEX type using a more or less conventional collision region will conveniently fit into one of the existing transverse caverns at Point 4, 6 or 8. However, the length of the spectrometer and the dimensions of the final detectors mean that a relatively minor enlargement of the machine tunnel will be needed on one side. This is the position of the so called mobile shielding of LEP which in any case must be removed to allow the LHC beam to pass. An enlargement of the tunnel to a diameter of about 7 m over a length of 5 m does not appear to pose any significant problems. The excavation can only be carried out after LEP has stopped running and the LEP experiment has been removed, but will not take more than a few months and has been estimated to cost around 600 KCHF.

Having permanently accessible counting rooms on the surface will mean that cable lengths have to be at least 150m. If access to the electronics is needed during collider operation, it might be necessary to provide a shielded region underground. We do not however believe this will be necessary.

If access during collider operation is needed to the electronics, it might be necessary to provide an underground shielded region, although we do not believe this will be necessary.

Figs. 11.1, 11.2 and 11.3 show the layout of COBEX and possible modifications to an existing cavern at Point 4, 6 or 8.

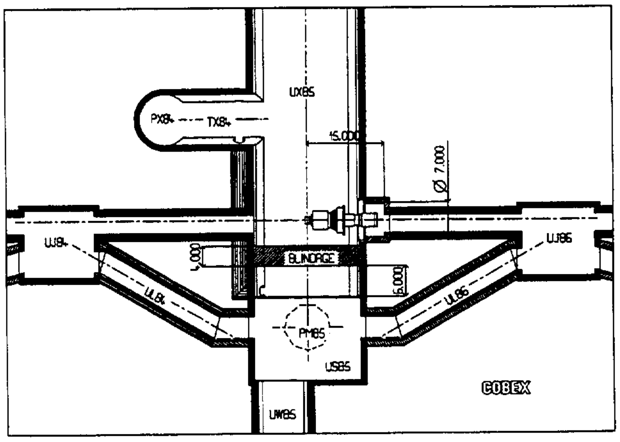

Figure 11.1: Layout of COBEX at even intereaction point: plan view.

11.3 Surface Zones and Services

For possible installation in any of the existing caverns at Point 4, 6 or 8, the surface zones could be used without modification. Since the COBEX detectors are smaller than the typical LEP detector, all facilities such as counting rooms, electrical power distribution, cooling and ventilation and gas installations are expected to be adequate. Similarly, the SX assembly hall and crane will be sufficient for preassembly and testing and the PX access shaft will be large enough for installation underground.

11.4 Installation Costs

It seems likely that COBEX will not need an underground counting room. Thus the total experimental

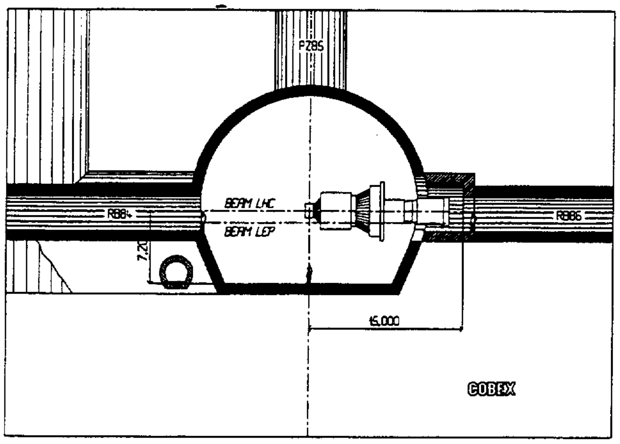

Figure 11.2: Layout of COBEX at even intereaction point: side elevation.

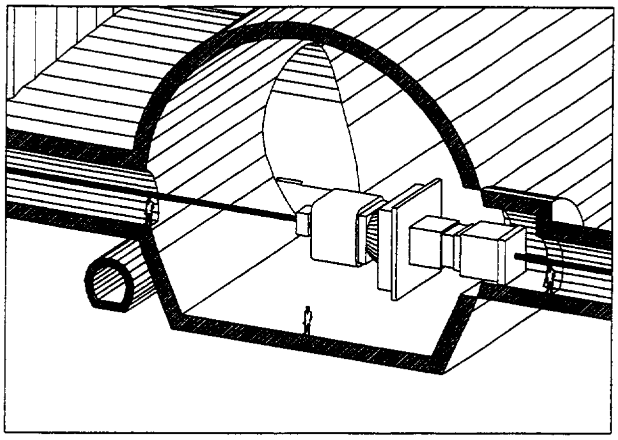

Figure 11.3: Layout of COBEX at even intereaction point: perspective.

area costs for COBEX will be around 12 MCHF - dominated by the cost of an LHC low-beta insertion (10MCHF). Installation costs will be additional, but should be much smaller amounts, because all services, power, gas pipes, etc. already exist.

13 Costs

The COBEX detector concept presented here, has been guided primarily by physics objectives and attention to cost has so far been a secondary concern. We have endeavored to design a detector with a high degree of redundancy to ensure that the physics objectives can be met and that the Monte Carlo predictions of efficiencies will be fulfilled. As the detector concept is refined, cost will receive far greater emphasis and reductions in channel count are likely. Thus, the costs presented here must be considered preliminary and, in some respects, overestimated. A summary of cost estimates is given in Table 13.1.

The collaboration is in a formative stage and it is not possible at this time to make clear divisions of responsibilities for the detailed design and construction of detector components. By the time the Technical Proposal is presented, a well-defined organizational structure must be in place.

Detector Subsystem	Quantity	Unit Cost	Total
Silicon Vertex Detector			
Si Detectors	64	6,500	416
Electronics	$1.1\cdot10^5$	0.7	77
Support			250
Subtotal			743
Silicon Pixel Detector			
Si Detectors	546	2,500	1,365
Electronics	54600	0.7	38
Support			250
Subtotal			1,653
Analyzing Magnets			
Quadrupole			8,000
Dipole			3,500
Subtotal			11,400
Drift Chambers			
Mechanical	19 modules	50,000	950
Electronics	$4.2\cdot10^5$	20	8,400
Subtotal			9,350
RICH Counters			
Mechanics			620
Electronics	$8.7\cdot10^5$	8	7,000
Subtotal			7,620
Tungsten Calorimeters			
Mechanics			100
Electronics	94	200	19
Subtotal			119
$PbWO_4$ Calorimeters			
Crystals	$3\cdot10^6$cm^3	2	6,000
Electronics	8500	200	1,700
Subtotal			7,700
Muon System			
Iron	160 tons	1	160
Chamber mechanics	12 modules	8,000	96
Electronics	6000	25	150
Subtotal			406
Triggering & DAQ			
Topology Trigger Processor			1,500
Muon Trigger Processor			100
Level III Processor Farm	500	9,000	4,500
Data Acquisition			2000
Subtotal			7,100
Total			47,100

Table 13.1: Detector costs. Unit costs are in CHF, total costs are in KCHF.